
Electronic Theses and Dissertations, 2004-2019

2015

Reactive Sputter Deposition of Lithium Phosphorus Oxynitride Thin Films, A Li Battery Solid State Electrolyte

Prabhu Doss Mani
University of Central Florida

 Part of the [Engineering Commons](#)

Find similar works at: <https://stars.library.ucf.edu/etd>

University of Central Florida Libraries <http://library.ucf.edu>

This Doctoral Dissertation (Open Access) is brought to you for free and open access by STARS. It has been accepted for inclusion in Electronic Theses and Dissertations, 2004-2019 by an authorized administrator of STARS. For more information, please contact STARS@ucf.edu.

STARS Citation

Mani, Prabhu Doss, "Reactive Sputter Deposition of Lithium Phosphorus Oxynitride Thin Films, A Li Battery Solid State Electrolyte" (2015). *Electronic Theses and Dissertations, 2004-2019*. 693.
<https://stars.library.ucf.edu/etd/693>

REACTIVE SPUTTER DEPOSITION OF LITHIUM PHOSPHORUS OXY-NITRIDE THIN
FILMS, A Li BATTERY SOLID STATE ELECTROLYTE

by

PRABHU DOSS MANI

B.E. National Institute of Technology, 2003

M.S. University of Central Florida, 2014

A dissertation submitted in partial fulfillment of the requirements
for the degree of Doctor of Philosophy
in the Department of Materials Science and Engineering
in the College of Engineering and Computer Science
at the University of Central Florida
Orlando, Florida

Summer Term
2015

Major Professor: Kevin R. Coffey

© 2015 PRABHU DOSS MANI

ABSTRACT

Lithium phosphorus oxy-nitride (LiPON) thin films are widely studied and used as a thin film electrolyte for lithium ion battery applications. LiPON thin films may be prepared by many techniques, but RF sputter deposition is most frequently used and was investigated in this dissertation, in spite of its low deposition rate, because of it offers more reliable and controllable processing. This dissertation includes the methodologies of sputter deposition and materials characterization of the LiPON thin film electrolytes.

The LiPON thin films were deposited under varying conditions of process gas, substrate bias, and deposition temperature. To understand the variations in ionic conductivity observed, the films were extensively characterized to examine structural and compositional differences, including examination by x-ray photoelectron spectroscopy (XPS), inductively coupled plasma optical emission spectroscopy (ICP/OES), and spectroscopic ellipsometry. In addition, film density, and the intrinsic stress of the deposited films were also studied.

The highest ionic conductivity of 9.8×10^{-6} S/cm was obtained at elevated deposition temperature and is correlated to a reduced density of defects, as indicated from the optical characterization.

Dedicated to my mom, Smt. Kasthuri Mani, dad, Mr. Mani Narayanasamy, my siblings Raghanna, Raji, Vimala, Kamala, their partner in crimes, Jayanthi anni (Raghanna's wife), Priya anni (Raji's wife), Shiva (Vimala's hubby), Gajendra Babu (Kamala's friend) and the little ones Shruthiksha, Diksha, Ganika, Vaibhaav and the new born chinna Raji. Also, to my paatis Paanjalai, periya paatti, pattan's Shri Narayanasamy, Shri Govindsamy and Shri Kuppusamy and muppattan Shri. Kottapuli.

I also dedicate this dissertation with utmost respect to all my wonderful teachers who have supported, guided and planted confidence all along my life, Ms. Thangam (3rd grade Gayatri Vidyala teacher), Ms. Karpagam (SSBV, Maths teacher) Ms Kamala (SSBV, History teacher), Telugu teacher SSBV, Tamil teacher SSBV, Chemistry teacher, Boston matriculation HSS, and Ms. Geetha, (Physics teacher SSBV), Physics teacher private tuition. PhD faculties Dr. Kevin Coffey, and committee members Dr. Sundaram, Dr. Heinrich, Dr. James J. Hickman. My previous committee members Dr. Linan An, Dr. Diego Diaz. Yoga teachers – Krista Shirley.

ACKNOWLEDGMENTS

These eight years had been a longest part of my life that I have spent away from my family and my country, mother India. It is a milestone that would have not been possible without the continuous support and guidance of my advisor, Professor Kevin R. Coffey. He is not only my advisor but has been my mentor all these years and have wholeheartedly shared his views on any questions that I may ask him not just with research but also career counseling and advice. I am deeply moved and fortunate to have an association with him as he evaluated me critically when needed and appreciated my efforts throughout my graduate school. English is my second language and I methodically learnt and acquired scientific writing skills during my study here. Dr. Coffey was patient, helpful and have always supported for learning and doing internships to acquiring technical skills.

My wholehearted thanks to my committee members Dr. Sundaram, Dr. Hickman, Dr. Heinrich, for guiding and serving in my dissertation committee.

Edward Dein is the another important person who have played me in my research learning everything in clean room right from sputtering tools to lithography process. He is more a friend and very respectable and admirable colleague. I am very fortunate to have collaborated with him at UCF.

My friends and colleagues of Dr. Coffey's group: Dr. Vinit Todi, Dr. Arun Vijayakumar, Dr. Andrew Warren, Daniel Yates, Dr. Bo Yao, Dr. Dave Shelton, Seth Hill and Sameer Izzat.

My sincere thanks to Karen Glidewell, Mikhail Klimov, Kirk Scammon, Maria Stancescu for assistance with characterization facilities. My special mention to Candace Martin for assisting me XPS analysis and it would not have been possible without her support.

My sincere thanks to Dr. Steven Duranceau, Maria Pea Real-Robert for assistance with ICP/OES analysis and their significant contributions in terms of corrections for LiPON manuscript.

It would have not been possible without Dr. Seal's assistance and for Electrochemical Impedance Spectroscopy measurements.

Dr. Vinit is also my roommate and have also been my mentor who guided me throughout these years. Dr. Arun, was more a great friend than a colleague. He was part of Planar Energy Devices, which sponsored the research from Fall 2007 to Spring 2012. Through him I was also able to do impedance measurements and gained technical exposure at Planar. Arun, his wife, Aswathi (Bhabhi) and son Madhav have made me feel like part of their family. I owe a big time them.

Dr. Balasubramaniam Lingam, Dr. Gautam Medhi, and Dr. Pankaj Kadwani were my roommates. Dr. Simranjeet Singh, though lived for a few months as a roommate, we became closer in days. They hold a significant part of my life. Dr. Pankaj got married to Pooja and had a baby boy Parin less than a year ago. Its inspiring when you see your friends grow and mature with their lives. Dr. Jyoti has been a great friend and significant other of Dr. Simran, they always hold a special place in my heart.

My close associates, Bojanna Palangappa, Karan Tamhane, Neha Bandewadekar, Afsaan Kermani, Nisha Mehta, Jerin Madhavapallil, Dr. Chetak Patel, Dr. Himanshu Saxena, Dr. Pansy Patel, Saral Shah and Neha Patel. The bond we share with each and every one of them is special and I am deeply indebted to them.

I am very very grateful to Cori Cunningham, who showed me Krista Shirley. I am deeply indebted to them. Cori is my beloved friend and Krista is my whole and sole motivating soul. I am really fortunate to have known them. Dash is the most humblest person I have ever seen. He is the gentleman and is my role model. Tatiana, Jason, Alethia, Heather, Stacey, and Natalia Serna have all shown humility is the cornerstone for being human. I have had the opportunity to learn from established teacher Tim Feldmann and Karen Breneman.

My thickest pals, well wishers, family friends, ones who actually know my family members and one's family members who know me: Geethapriya Balasubramanium, Priya Saikumar. These two have fair share of my life and heart and kind of soul mates.

Ms. Priyadarshini Ravindran. Needless to say about this loyal friend, one will make you feel worthy of yourself. She is innocent and her entire family knows me. Such a good person to lean on.

Saisitaram Ramesh, Jaishree Gnans, the best couple that I have known. They inspire me.

My beloved sisters: Ms. Pavi, Ms. Vidusha, Ms. Ramya and my beloved brothers: Dr. Mahadeven, Supreeth Rajan. These are people I hangout and go for trips and played volleyball, and many other games. They made feel lighter. They made me dance, which is a big thing. Southern Spice lovers.

My fellow UCF friends who guided me and supported me unconditionally during my initial years at UCF: Dr. Kumaran, Dr. Prakash Palanisamy, Dr. Prabhakar Mohan, Dr. Abhilash Vincent, Dr. Manjeri, Dr. Virendra, Dr. Ajay Karakoti, Dr. Vinoth, Dr. Himansu Pattanaik. Dr. Pattanaik and his wife Dr. Smrithi are good friends and shared quite a good time.

My cute friends - Swetha Barkam, Shashank Saraf and Sruthi Reddy. Swetha has been my closest friend with whom apparently I spent the longest time at UCF. She has been part of the senate and her creativity and easy demeanor always inspire me. I have such a deep association that words cannot describe. She opened the doorways for having new friends at UCF towards the end of PhD student life. Shashank, is an associate you can rely on not only for sharing facilities at his lab, but also on a personal level. Impedance spectroscopy would not have been possible without Shashank and Dr. Virendra. Sruthi is a great loyal and trustable friend one can have, and also my wake up text messenger. Swetha and Sruthi painted Joker's face during Halloween which I consider the best moment at UCF. These people inspire me and are my family.

My special UCF friends Vaahini Ganesan, Janardan Nath, and Ashwin Kumar with whom I learnt photography, played volley ball and attend many events in the recent past. A very very great couple (Vaahini and Janardan) to hangout with.

Shout out to Tushar, Shraddha, Siddesh, Raveena, Rishi, Vinoth, Manoj Reddy, Hari Kishan, Nishant. There are lots to learn from younger generation and they really inspire you.

Sangeetha, Sarmila, Rev, Sangeetha's mom, Vijayalakshmi and dad, Sathya Seelan. They took care of me and Jagi when we were in Malaysia. I owe big time to this amazing family.

My longest and deepest friends Chakku, Thiruna, Shylu, Vijayan and Shylu. They are support system. Lots of love always.

Many thanks to Scott Faris and the team at Planar Energy who have funded my PhD project between Fall 2007 and Spring 2012 and also giving me an opportunity to intern with them.

My friends at Quantumscape Corporation - Cheng-Chie-Chao, Ken Hammerel, John Lehan, Bradley Stimson, Jason, Niall Donnelly, Tim Holmes, Jagdeep Singh. I learnt a lot while interning there and its been a pleasure to work with them and fortunate to get the opportunity.

My extended part of my family, the ones who have seen almost most part of my life and have spent considerable amount of my time since childhood: Murali and Jagadeesh. I owe my life to them. Murali's mom, brother, wife Vidya and daughter Harshu. Jagadeesh's family.

My uncle Shankar mama, his wife mami Jayanthi, and their daughters. Chithi, periyamma, periya mama KK Kannan and mami Godavari and their daughters Amlu, Kutti, Shankar Chitthappa, chitthi and kids, Aththai and kids.

I would also like to thank Toni, Kim, Dr. Andrew, Dr. Sohn for providing me the opportunity to work in alpha-alumina project.

To all others who I forgot to mention here, I am deeply indebted to you all.

TABLE OF CONTENTS

| | |
|--|-------|
| LIST OF FIGURES ----- | xiii |
| LIST OF TABLES ----- | xviii |
| CHAPTER 1 INTRODUCTION:----- | 1 |
| 1.1 Thin film lithium ion batteries: ----- | 1 |
| 1.2 Presentation of the problem: ----- | 2 |
| 1.2.1 Requirements of solid state electrolyte ----- | 2 |
| 1.2.2 Lithium phosphorus oxynitride----- | 5 |
| 1.2.3 Objective of the current research----- | 7 |
| CHAPTER 2 BACKGROUND----- | 9 |
| 2.1 Lithium Phosphorus Oxynitride ----- | 9 |
| 2.1.1 Lithium phosphate ----- | 10 |
| 2.1.2 Nitridation of lithium metaphosphates and lithium orthophosphate ----- | 15 |
| 2.2 Ionic conduction----- | 22 |
| 2.2.1 Motion of Ions in solid electrolytes ----- | 22 |
| CHAPTER 3 EXPERIMENTAL TECHNIQUES----- | 26 |
| 3.1 Reactive sputter deposition----- | 26 |
| 3.1.1 RF substrate biasing ----- | 27 |
| 3.1.2 Process gas pressure ----- | 29 |

| | |
|---|--------|
| 3.1.3 Deposition temperature----- | 29 |
| 3.1.4 Sample preparation ----- | 29 |
| 3.1.5 Sample Processing----- | 30 |
| 3.2 Characterization ----- | 31 |
| 3.2.1 Spectroscopic ellipsometry ----- | 32 |
| 3.2.2 Electrochemical impedance spectroscopy----- | 36 |
| 3.2.3 X-ray photoelectron spectroscopy----- | 40 |
| 3.2.4 Secondary ion mass spectroscopy----- | 43 |
| 3.2.5 Inductively coupled plasma – optical emission spectroscopy----- | 45 |
| 3.2.6 Stress measurement ----- | 48 |
| CHAPTER 4 PRELIMINARY RESULTS AND DISCUSSION----- | 50 |
| 4.1 Thickness measurements ----- | 50 |
| 4.2 Stress measurements----- | 51 |
| 4.3 Surface characterization ----- | 55 |
| 4.3.1 Surface roughness----- | 55 |
| 4.3.2 Scanning electron microscopy----- | 55 |
| 4.4 Secondary ion mass spectroscopy----- | 55 |
| 4.5 Summary ----- | 57 |
| CHAPTER 5 RESULTS----- | 58 |
| CHAPTER 6 DISCUSSIONS----- | 74 |

| | |
|---|----|
| 6.1 Substrate bias power ----- | 74 |
| 6.2 Pressure effects at 10W substrate bias condition ----- | 77 |
| 6.3 Deposition temperature effects at 10W bias condition: ----- | 77 |
| CHAPTER 7 CONCLUSIONS ----- | 86 |
| CHAPTER 8. FUTURE WORK ----- | 88 |
| 8.1 Solid state nuclear magnetic resonance study on the effects of substrate bias power, substrate heating ----- | 88 |
| 8.2 Effect of hydrogen doping ----- | 88 |
| 8.3 Effect of cation doping ----- | 88 |
| 8.4 Effect of anion doping ----- | 89 |
| 8.5 3D microfabrication----- | 89 |
| REFERENCES ----- | 90 |

LIST OF FIGURES

| | |
|--|----|
| Figure 1-1 Comparison of volumetric and gravimetric energy densities of Lithium ion batteries .1 | .1 |
| Figure 1-2 Battery Voltage losses Vs Operating Current [1] (a) IR loss (b) Activation polarization and (c) Concentration polarization.....2 | 2 |
| Figure 2-1 Li_3PO_4 Chemical bond structure: (a) Lewis structure (b) simplified bond structure. The sp^3 hybrid orbitals of phosphorus forms four covalent σ bonds and one covalent π bond with oxygen. Note that the Li^+ ion conduction happens by hop to the double bonded oxygen in exchange for π bonds. This representation is presented from the reference cited.[29].....10 | 10 |
| Figure 2-2 Various tetrahedral sites of phosphate glasses[47]11 | 11 |
| Figure 2-3 Tetrahedra structures as a function of a ratio, $R = \text{M}_2\text{O}/\text{P}_2\text{O}_5$, $M = \text{Li}$ or Na [48].....12 | 12 |
| Figure 2-4 shows two unit cells of $\gamma\text{-Li}_3\text{PO}_4$. The Li atoms are shown as isolated atoms (black) and the PO_4 groups are shown as shown tetrahedra. The PO_4 tetrahedra have no shared oxygen atoms and are therefore isolated from each other14 | 14 |
| Figure 2-5 is showing $\gamma\text{-Li}_3\text{PO}_4$ structure with 3 LiO_4 tetrahedra (two $\text{Li}_\text{I}\text{O}_4$ and one $\text{Li}_\text{II}\text{O}_4$) (right). This Figure is reproduced from a reference.[10].....15 | 15 |
| Figure 2-6 Nitridation of a part of metaphosphate chain. The nitrogen atoms that replace oxygen atoms increase the cross-linking between PO_4 tetrahedra [7,51,52].16 | 16 |
| Figure 2-7 Polyhedral crystal structure of $\beta\text{-Li}_3\text{PO}_4$ in (a) (001) shown above and (b) (100) shown below with PO_4 (dark) LiO_4 (light [6]17 | 17 |

| | |
|---|----|
| Figure 2-8 Polyhedral crystal structure of $\gamma\text{-Li}_3\text{PO}_4$ in (a) (001) left and (b) (100) right. PO_4 (dark), LiO_4 -(light), $\text{Li}_\text{I}\text{O}_4$ -(gray), $\text{Li}_\text{II}\text{O}_4$ -(dots). O_I , O_II , O_III represents black, gray and white circles respectively[6] | 18 |
| Figure 2-9 Representation of structural difference in $\gamma\text{-Li}_3\text{PO}_4$ and polycrystalline LiPON with $\gamma\text{-Li}_3\text{PO}_4$ structure [6,16] | 19 |
| Figure 2-10 Vacancy, interstitial and interstitialcy type diffusion processes in crystalline solids | 22 |
| Figure 3-1 The sputtering deposition geometry used axial rotation of the substrate to provide circumferential uniformity of the deposited film thickness from an off-axis magnetron sputter deposition source (one of three is shown). The tilt angle of the deposition source was adjusted to optimize radial thickness uniformity..... | 26 |
| Figure 3-2 A metal/electrolyte/metal layered structure was used for ionic conductivity measurements. (a) is the layer structure, (b) a side view, and (c) is a top view showing the cross electrode geometry. | 29 |
| Figure 3-3 Ellipsometry set-up. | 33 |
| Figure 3-4 Overlapping top electrodes of adjacent devices in ionic conductivity measurement.[33,78] | 35 |
| Figure 3-5 Impedance-Frequency response, Nyquist plot, of a typical MEM device. Dotted line show imperfect blocking electrodes..... | 36 |
| Figure 3-6 Circuit model of an MEM device | 38 |
| Figure 3-7 The equivalent circuit model used to extract ion transport resistance, R_ion , to determine the ionic conductivity of LiPON films. The other circuit elements are identified in the text. | 39 |

| | |
|---|----|
| Figure 3-8 The photoelectric effect in X-ray photoelectron spectroscopy..... | 42 |
| Figure 3-9 A basic ESCALAB 220XI configuration and schematics | 43 |
| Figure 3-10 Perkin Elmer – Optima 2100 DV ICP/OES spectrometer | 44 |
| Figure 3-11 Radial view and axial view schematics in Optima 2100 DV ICP/OES spectrometer | 47 |
| Figure 3-12 shows the sample placement on the substrate holder during LiPON film deposition for stress measurements..... | 49 |
| Figure 4-1 Thickness profile Vs Gun tilt..... | 50 |
| Figure 4-2 Deposition rate Vs Substrate bias | 51 |
| Figure 4-3 Cartoon of the delaminated film on Silicon | 52 |
| Figure 4-4 Cartoon of the non-delaminated film on Silicon | 52 |
| Figure 4-5 Stress measurements | 53 |
| Figure 4-6 Surface Roughness Measurements | 53 |
| Figure 4-7 Delaminated film-SEM surface, cross section and FIB cross section | 54 |
| Figure 4-8 Non-delaminated film with crack initiating site-SEM surface, cross section and FIB cross section | 54 |
| Figure 4-9 Delaminated region SIMS profile..... | 56 |
| Figure 4-10 Non-delaminated region SIMS data..... | 56 |
| Figure 5-1 Result of the XPS depth profiling of sample G. Inset (a) shows the variation of composition as atomic percent as a function of ion milling time in an area with Pt electrodes. Inset (b) shows the equivalent depth profile of an adjacent area without Pt electrodes. Inset (c) shows %LiPON, %Pt, %C, %Si and the (>N-)/(=N-) bond ratio as a | |

function of ion milling time for an area with Pt electrodes. Inset (d) shows the %LiPON, %C, %Si and the (>N-)/(=N-) bond ratio for an adjacent area without Pt electrodes. Inset (e) shows the high resolution N1s scans from the area with Pt electrodes overlaid at a sequence of ion milling times to illustrate the relative consistency of the N bonding with depth. Inset (f) shows the high resolution N1s scans from an adjacent area without Pt electrodes to illustrate the variation of N bonding in the upper portion of the LiPON layer.

.....62

Figure 5-2 Results of XPS depth profiling of samples B and F. Insets (a) and (b) show the variation in composition and bonding for sample B in an area with and without Pt electrodes, respectively, in a manner equivalent to that of Figure 5-1 (a) and (b) for sample G. Insets (c) and (d) show the same comparative data for sample F.....64

Figure 5-3 Examples of the deconvolution of the high resolution XPS spectra from sample G of Li1s, O1s, N1s and P2p scans are given by insets (a), (b), (c) and (d), respectively. The attribution of the peaks to different bonds is given in the text.....66

Figure 6-1 Inset (a) shows the ionic conductivity and inset (b) the activation energy of ionic conduction for LiPON films as a function of substrate bias power. Please note that the curved lines are shown to guide the eye.76

Figure 6-2 Inset (a) shows the ionic conductivity and inset (b) the activation energy of ionic conduction for LiPON films as a function of deposition temperatures. Please note that the lines are shown to guide the eye.79

Figure 6-3 Inset (a) shows the optical extinction coefficient, k, and inset (b) the refractive index, n, for LiPON films deposited at various deposition temperatures as a function of

wavelength. Inset (b) also shows a subset graph that shows the increase in refractive index at 999nm as a function of deposition temperature. Please note that the curve line is shown to guide the eye.81

Figure 6-4(a) The energy variation of an amorphous glass with the displacement of a diffusing interstitial atom (Li^+ in LiPON) as it jumps between successive interstitial sites of varying energy levels. The type k site shown in the picture is at a typical lowest energy or a deep trap site. (b) A plot similar to (a) for interstitial jumping in an idealized or ordered material containing only the sites of equal energy states state and having activation energies corresponding to E^o .(Reproduced, by permission, from John and Wiley Sons Inc., "Kinetics of Materials", by Robert W. Balluffi, Samuel M. Allen, W. Craig Carter, *Chapter 10 Diffusion in Non-crystalline Materials, Figure 6-4.4, p235. Copyright © 2005 by John Wiley & Sons, Inc.*)[99]83

Figure 6-5 shows the characteristics of LiPON films deposited under different temperature conditions. Figure 6-4 (a) shows the increasing trend of the ionic conductivity, the decreasing trends of Li/P atomic ratio measured by XPS and molar volume calculated from film density and atomic concentration. Figure 6-4 (b) shows a decreasing trend of lithium oxide, Li_2O , and an increasing trend of reduced metallic phosphorus with the increase of deposition temperatures. In Figure 6-4 (c) the correlation between penetration depth, δ , (nm) and the ionic conductivity is strong and almost linear. Please note that the curved lines are shown to guide the eye.85

LIST OF TABLES

| | |
|--|----|
| Table 5-1 enlists various sample series, identified with A to O. The processing conditions of each sample including substrate bias power, deposition temperature, process gas type, gas pressure and flow. The deposition rate is also included for each sample..... | 58 |
| Table 5-2 compares the properties of LiPON samples A through O. The film properties included here are the ionic conductivity, the activation energy for the ionic conduction, thin film intrinsic stress, (developed during deposition and cooling), film density and the optical properties. The optical constants, refractive index (n) at 999 nm, extinction coefficient (k) at 246 nm, penetration depth in nm and the optical band gap energy in eV.. | 59 |
| Table 5-3 shows the XPS measured elemental compositions in atomic percentages of Li, P, O, N, and the derived stoichiometry of LiPON films. The Li/P atomic ratios calculated from XPS and the ICP/OES are also compared. | 68 |
| Table 5-4 shows the comparison of lithium bonds (Li bonding in LiPON and lithium bonded to just oxygen (Li ₂ O) as in non-LiPON) and the nitrogen bonds (N1, N2, N3, N3/N2 ratio) associated with LiPON and unidentified nitrogen bond (N4) associated with non-LiPON.. | 70 |
| Table 5-5 shows the comparison of deconvoluted phosphorus and oxygen bonds The phosphorus bonds include the phosphate PO ₄ ³⁻ and the reduced metallic phosphorus while the oxygen bonds include oxygen bonded in phosphate PO ₄ ³⁻ (bridging oxygen, (-O-), and non-bridging oxygen, (P=O)) and oxygen bonded with lithium (Li ₂ O, non-LiPON). | 72 |
| Table 5-6 shows the molar volume calculations from the atomic weights of Li, P, O, and N in LiPON, the measured film density, and the molar volume. | 73 |

CHAPTER 1 INTRODUCTION:

1.1 Thin film lithium ion batteries:

Thin film lithium-ion batteries are of interest due to their use as an integrated source of power to operate a variety of miniaturized devices, such as micro-machines, sensors, transmitters and electronic circuitry. Such devices require the storage of energy in a small and light source and a low rate of internal energy dissipation. Figure 1-1 shows a comparison of volumetric and gravimetric energy densities of lithium ion and other battery technologies.

Lithium-ion batteries are comprised of cells in which Li^+ ions are transported between the positive and negative electrodes during intercalation and de-intercalation. Hence they are also called “rocking chair batteries”.

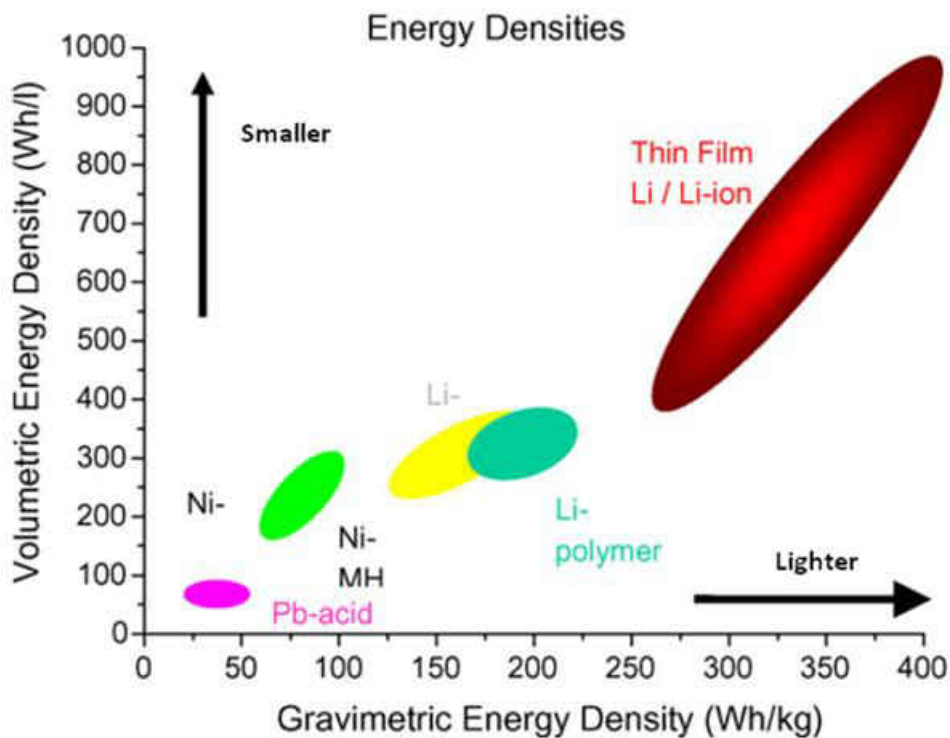


Figure 1-1 Comparison of volumetric and gravimetric energy densities of Lithium ion batteries

Lithium is the most attractive anode material as it has a favorable thermodynamic electrode potential with high specific capacity. Lithium metal is highly reactive with many solid-state electrolytes.

Thin film battery components include current collectors, cathode, anode, an electrolyte, and protective coating material. Thin film battery cells have typical energy densities near 3.6 J cm^{-2} (1 mWh cm^{-2}).

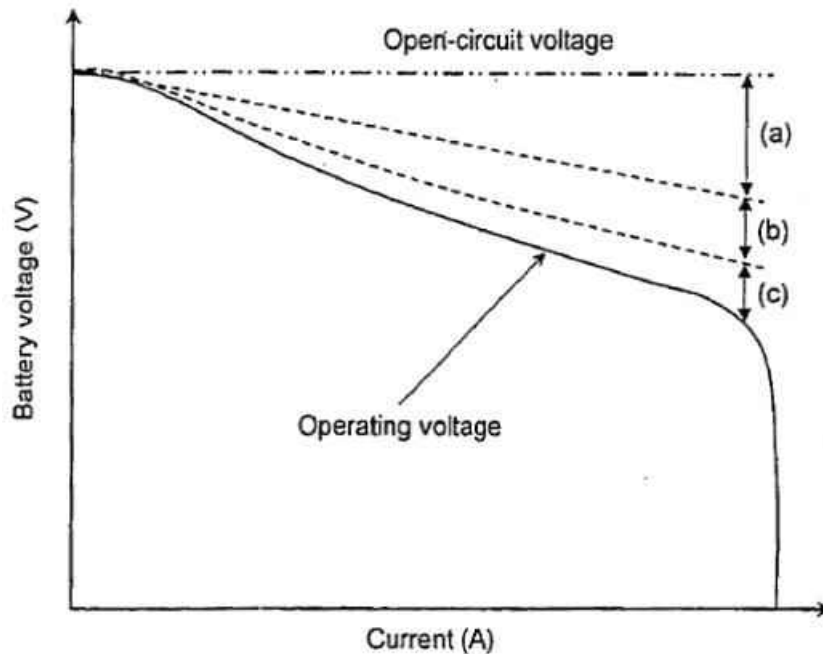


Figure 1-2 Battery Voltage losses Vs Operating Current [1] (a) IR loss (b) Activation polarization and (c) Concentration polarization

1.2 Presentation of the problem:

1.2.1 Requirements of solid state electrolyte:

The voltage across a battery that is not connected to an external load resistor is known as the open circuit voltage, and ideal batteries have a flat current-voltage profile equal to the open-circuit voltage. This profile is illustrated in Figure 1-2. But the voltage profiles in real batteries are seldom flat. Possible mechanisms for the drop in battery voltage with increasing current are:

- (a) IR loss: When there is a high internal resistance in the battery, a significant voltage drop occurs across the battery itself.
- (b) Activation polarization: During the discharge process of battery operation positive ions move from anode to cathode through an electrolyte. The electrolyte-electrode interface is heterogeneous and acts as an energy barrier to the charge transfer reaction. This is known as activation polarization. A voltage drop occurs due to the slow charge transfer reaction when there is a high energy barrier [1].
- (c) Concentration polarization: When the ions move slowly in the electrolyte during the discharge, then a concentration difference, called a concentration polarization, occurs at the electrolyte-electrode interface [1]. This concentration polarization acts as a resistance and causes an additional voltage drop across the battery.

Hence, the total voltage drop is the additive contributions from the above three mechanisms. When the battery terminals are connected to an external load resistor (R) the additive voltage drop can be given in the equation [1] as follows:

$$V = V_{oc} - [(\eta_{ct})_a + (\eta_c)_a] - [(\eta_{ct})_c + (\eta_c)_c] - I * R_i = I * R \quad (1-1)$$

- where,
- V_{oc} = Open-circuit voltage of a battery
 - η_{ct} = Activation polarization or charge-transfer overvoltage at either an anode or a cathode
 - η_c = Concentration polarization at either an anode or a cathode
 - R_i = Internal resistance of the battery
 - I = Operating current through an external resistor

Given the above mechanisms, it is clear that many aspects of the solid-state electrolyte are important to optimize the battery performance.

(i) Having a high ionic conductivity in the solid-state electrolyte means having a minimum internal IR loss. The internal resistance, R_i , is inversely proportional to, σ_i , the ionic conductivity:

$$R_i = \frac{h}{\sigma_i * A} \quad (1-2)$$

where h is the thickness and A is the area of the electrolyte. As the ionic conductivity is directly proportional to the mobile ion concentration, the ionic conductivity is increased by the number of mobile ions present. Equation (1-2) also makes it clear that the electrolyte thickness must be minimized and its area and ionic conductivity maximized to reduce the internal resistance loss.

(ii) The solid electrolyte must also insure that the current present in the electrolyte is mostly due to that from the transport of the desired ion, i.e., Li^+ . This is commonly quantified as the transport number, which compares the desired ion conductivity to the total conductivity of the electrolyte.. The transport number t_i is given by :

$$t_i = \frac{\sigma_i}{\sigma_t} \quad (1-3)$$

where σ_t is the total conductivity and σ_i is the conductivity of working ions [2]. The total conductivity is given by $\sigma_t = \sigma_i + \sigma_e + \sum_j \sigma_j$, where σ_e is the electronic conductivity and $\sum_j \sigma_j$ is the conductivity of all other mobile ionic species. Any counter mobile ions that may be present will accumulate near the electrode-electrolyte interface, which induces a counter-internal electric field and generates a concentration polarization. Solid electrolytes should be electrically insulating ($\sigma_e = 0$), otherwise an internal leakage current will be present that will provide a power loss [2].

(iii) The reaction rate of charge transfer at the electrolyte-electrode interface should be sufficiently fast such that the charge transfer resistance is minimal.

(iv) The solid-state electrolyte has to retain its mechanical and chemical integrity and, specifically, remain impervious to any reactants during repeated charge/discharge cycles. Reduction or oxidation of this electrolyte could damage the cell beyond its working limits [2].

(v) The maximum voltage that a battery may be exposed to is known as the voltage window (V_g). The voltage window is necessarily greater than the open circuit voltage and is typically limited by the stability of the electrolyte. A high voltage window is desirable to ensure stability of the battery during charging.

(vi) Electronic conductivity can occur homogeneously throughout an electrolyte (e.g. as in LiNbO_3 [3]) where it is readily quantified by the transport number, described in point (ii) above. However, electronic conductivity can also occur heterogeneously by the formation of electrolytic paths of electronically conducting foreign materials. Such electrolytic paths may include cracks or pinholes where the cathode and anode materials deposit during the formation or operation of the cell. This may result in the creation of lithium dendrites on one of the electrode-electrolyte interfaces.

As described in points (i) to (vi) above, the properties of the solid-state electrolyte are crucial to battery performance. Hence a solid state electrolyte should have high ionic and low electronic conductivity, fast charge transfer at electrolyte-electrode interface, and good mechanical, chemical, and electrochemical stability.

1.2.2 Lithium phosphorus oxynitride

Lithium phosphorus oxynitride (LiPON) is one of the most studied solid state electrolytes in thin film form [4–31]. Xiaohua Yu [9] showed that amorphous LiPON exhibits only Li^+ ion conductivity between -26°C to 140°C , with an ionic conductivity of $2.3 (\pm 0.7) * 10^{-6}$ S/cm at 25°C and activation energy of $0.55 (\pm 0.02)$ eV. He reported negligible electronic conductivity

(10^{-14} S/cm) and inferred the transport number of unity.[32]. This is expected for alkali-metal oxide glasses since the nitrogen, oxygen and phosphorus atoms are rigidly bounded in the LiPON framework structure and exhibit zero mobility at ordinary temperatures. A voltage window of 5.5 ± 0.2 V at room temperature was also reported. Yu also described LiPON as mechanically stable and a rigid barrier to the possible growth of lithium dendrites that did not crack as the cathode volume changed during battery cycling.

Other workers have reported that LiPON suffers from a high level of internal stress that degrades its reliability. RF sputter deposited LiPON thin films can exhibit crack formation and have a tendency for increased delamination with time. These phenomena are understood as due to a high level of internal stress that is induced during the deposition process. LiPON films prepared by ion beam assisted deposition have been reported to suffer electronic shorting due to the internal stress raised by the difference in thermal expansion coefficients between that of the substrate and the film [13].

Lithium phosphorous oxy-nitride (LiPON) is one of the widely studied and commercially used solid state electrolytes in lithium battery technology. LiPON films have a stable network, wide electrochemical window, negligible electronic conductivity, and a relatively high ionic conductivity.[9] For LiPON films prepared by magnetron sputter deposition, the role of processing parameters in determining film properties is complex. Thin films of LiPON were first characterized and investigated for thin film batteries by Bates et al. where a maximum ionic conductivity of 3.3×10^{-6} S/cm[4,5] was reported. Bates et al. used radio-frequency (RF) sputter deposition to prepare thin film samples[4,5], a primary processing technique for LiPON thin films.[4–7,9,12,22,24,31,33] Other methods, such as, ion-beam assisted deposition (with ionic conductivity of 1.1×10^{-6} S/cm)[16], plasma assisted directed vapor deposition (between 10^{-7} and

10^{-8} S/cm)[29], and evaporation (6×10^{-7} S/cm)[34] have also been used.

The RF sputtering technique commonly uses a lithium ortho-phosphate (Li_3PO_4) target and a nitrogen sputtering process gas. Almost all prior reports of the ionic conductivity for RF sputtered LiPON thin films are in the range of 6×10^{-7} S/cm to 3×10^{-6} S/cm. [4–7,9,12,16,22,24,29,31,33,34] The exception was the work of Chiu et al.[35] who reported a higher ionic conductivity of 9.1×10^{-6} S/cm, which is still considerably lower than that of sulphide solid state electrolyte materials which are in the range of 10^{-3} S/cm.[36,37] Accordingly, the primary aim of this study was to explore the further potential of deposition process parameters (i.e., substrate biasing, substrate heating, process gas pressure) to improve the ionic conductivity of LiPON films and to replicate or improve on the ionic conductivity results of Chiu et al.[35]

1.2.3 Objective of the current research

The main objective of the proposed research is to use and extend our understanding of LiPON to increase its ionic conductivity. Additionally, the proposed research intends to develop this high ionic conductivity in reactively sputter deposited LiPON films having controlled internal stress that are mechanically robust and suitable for battery applications.

The lithium sulphur electrolytes are super-ionic conductors with the ionic conductivity in the range of 10^{-3} S/cm, but they are hygroscopic and required stringent environmental controls to process and develop. The LiPON films are mechanically stable and non-hygroscopic and hence this dissertation study is aimed to:

- maximize the ionic conductivity in RF sputter deposited LiPON thin films, replicating and exceeding the ionic conductivity achieved by Chiu et al.
- characterize and understand the LiPON film structure, process and properties correlation.

- validate the characterization methods employed by various authors in ionic conductivity measurements, XPS sample preparation and analysis and sample digestion procedure for ICP/OES measurements.

- and develop/improve methods for sample preparation in ionic conductivity measurements, chemical bonding and composition analysis using XPS depth profiling, sample digestion procedure in ICP/OES and penetration depth/band gap energy calculations using spectroscopic ellipsometry measurements

To achieve these objectives, LiPON processing will be investigated, to include compositional modifications. In addition to the properties of LiPON as a battery electrolyte (ionic conductivity, stress), the structure of the amorphous LiPON films will be investigated by a variety of techniques including spectroscopic ellipsometry and X-ray photoelectron spectroscopy (XPS). The composition of LiPON will be studied by XPS and inductively coupled plasma-optical emission spectroscopy, (ICP/OES).

CHAPTER 2 BACKGROUND

2.1 Lithium Phosphorus Oxynitride

The charging and discharging rates of lithium-ion batteries are controlled by the electrochemical diffusion of lithium ions, which is characterized by the lithium-ion conductivity. These batteries require high ionic conductivity, which poses a significant challenge for an inorganic electrolyte because of their dense atomic structures.

Amorphous lithium phosphorus oxynitride (LiPON) is a widely used thin film solid state electrolyte for rechargeable thin-film lithium-ion batteries because of its exceptional electrochemical stability and good Li^+ ion conductivity [9]. This electrolyte has demonstrated a voltage window of 5.5V [4,8], an acceptable value for lithium-ion batteries that operate at ~4.0 V.

The historical development of LiPON as a solid state electrolyte is very interesting. Many inorganic compounds are better ionic conductors in an amorphous state than in a crystalline form and LiPON is an example of this. The ionic conductivity of the amorphous lithium orthophosphate with composition $0.6\text{Li}_2\text{O} : 0.4\text{P}_2\text{O}_5$ is 10^2 times greater than that of its crystalline form Li_3PO_4 [38]. It was known that the durability in contact with air and water of sodium metaphosphate was improved by nitriding [39], and this also proved true for LiPON[40]. In addition to stability, nitriding lithium orthophosphate also increased the ionic conductivity of the electrolyte by a factor of 30 [38]. However, the reaction of LiPON[41–44] with moisture, oxygen and carbon have been observed have resulted in surface deterioration and thus reduction in ionic conductivity and reduced capacity was observed. This can be mitigated by using an over layer of LiPON[11] deposited on top of the electrode. To place these observations in context, an understanding of the bonding of lithium phosphates and nitrated lithium phosphates is necessary.

2.1.1 Lithium phosphate

Lithium phosphate glasses are formed by addition of a network modifier, Li_2O to the network former, P_2O_5 . [45]. The Lewis structure of Li_3PO_4 , the electronic configuration and the combination of Li_2O and P_2O_5 to form various lithium phosphates are pivotal to understanding the ionic conduction phenomenon in LiPON films. Hence, some inferences from the work of Kim[29] and Vereda-Moratilla[16] are discussed here. The phosphate glass framework is comprised of PO_4 tetrahedra, each of which is bonded to three other tetrahedral in the absence of Li. In this compound, the phosphorus outer electrons ($3s^23p^3$) form sp^3 hybrid orbitals and its bonding can be represented by the Lewis structure shown in Figure 2-1(a).

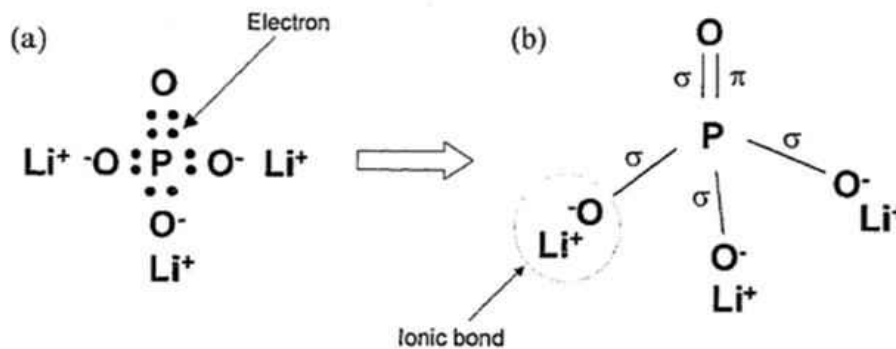


Figure 2-1 Li_3PO_4 Chemical bond structure: (a) Lewis structure (b) simplified bond structure. The sp^3 hybrid orbitals of phosphorus forms four covalent σ bonds and one covalent π bond with oxygen. Note that the Li^+ ion conduction happens by hop to the double bonded oxygen in exchange for π bonds. This representation is presented from the reference cited.[29].

In Figure 2-1(b) a simplified structure of Li_3PO_4 is shown and from this we can understand the basic issues of electronic and ionic conductivity in these materials. Four of the outer phosphorus electrons form four covalent σ bonds with the 2p electrons of the four oxygen atoms and the fifth phosphorus outer electron forms a strong covalent π bond [45]. This chemical bond structure has no mobile electrons available, thus crystalline Li_3PO_4 is an insulator and has a large band gap energy of 5.75 eV [46].


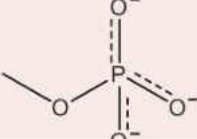

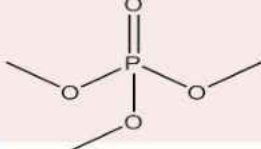
| No. of bridging oxygen (i) | Tetrahedra | Illustration |
|----------------------------|------------|--|
| 0 | Q^0 |  |
| 1 | Q^1 |  |
| 2 | Q^2 |  |
| 3 | Q^3 |  |

Figure 2-2 Various tetrahedral sites of phosphate glasses[47]

The Li_3PO_4 molecule has a PO_4 tetrahedron with a phosphorus atom in the center and four oxygen atoms on its vertices. Three of the four outer oxygen atoms have an ionic bond to a Li atom while the fourth has the π bond to the central phosphorous atom. The Li atoms have the freedom to migrate to the empty π bonded oxygen atom site (and the π bond moves to the vacated Li site), which constitutes the most basic form of ion transport. Li-deficient glasses will have additional sites for Li ions to move to and, hence, can provide a higher lithium-ion conductivity than stoichiometric Li_3PO_4 glasses. The phosphate glass framework is comprised of PO_4 tetrahedra, each of which is bonded to three other tetrahedral in the absence of Li. Thus the combination of PO_4 tetrahedra defines the phosphate glass types.

The PO_4 tetrahedra that form the three-dimensional glass network can be classified by Q^i , where i is the number of bridging oxygen atoms of the tetrahedron [47]. The various Q^i

tetrahedral configurations in phosphate glasses are shown in Figure 2-2. Networks of these glasses are characterized by the [O]/[P] ratio, or equivalently by the value of x in the general formula $x\text{Li}_2\text{O} \cdot (1-x)\text{P}_2\text{O}_5$. Glasses with low [O]/[P] ratio or small x have more shared oxygen atoms between tetrahedra, such that they have predominantly Q^3 and Q^2 configurations, while glasses with high [O]/[P] ratio or larger x have more Q^1 and Q^0 tetrahedra.

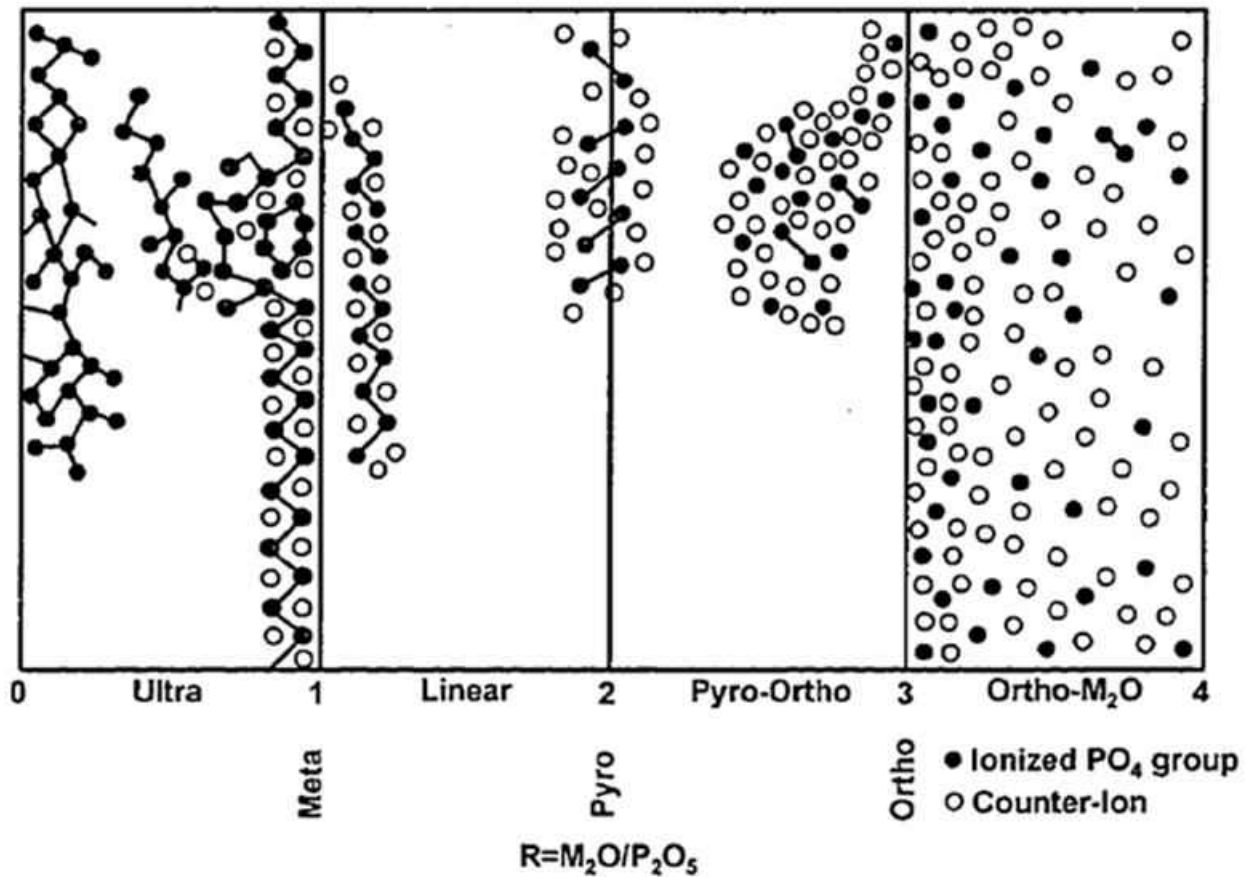


Figure 2-3 Tetrahedra structures as a function of a ratio, $R = \text{M}_2\text{O}/\text{P}_2\text{O}_5$, $\text{M} = \text{Li}$ or Na [48]

Another equivalent metric of phosphate glass composition is the ratio, R , of Li_2O to P_2O_5 [45]. The R value can be used to classify phosphate glasses as ultraphosphate ($R < 1$), metaphosphate ($R = 1$), polyphosphate ($1 < R < 3$), and orthophosphate ($R = 3$). Figure 2-3 illustrates the impact of the R value on the ability of the phosphate to form a network. A brief overview of

the different binary phosphate glass structures that are possible as a function of R and the role of nitrogen incorporation into metaphosphate and orthophosphate glasses will be examined below.

2.1.1.1 Vitreous P_2O_5

Vitreous P_2O_5 is an ultraphosphate glass ($R = 0$) with a base structure of Q^3 tetrahedra having three bridging oxygen atoms (P-O-P) and one non-bridging oxygen (P=O). The non-bridging oxygen bond length is shorter and the bond strength is stronger than that of the bridging oxygen atoms and the 3D network of this glass has some features of crystalline hexagonal P_2O_5 .

2.1.1.2 Ultraphosphate glasses

The P_2O_5 structure undergoes a depolymerisation process when alkali oxides are added to it (increasing x in the formula $xLi_2O \cdot (1-x)P_2O_5$). During this process some of the P-O-P bonds are destroyed and the terminal oxygen bonding (P=O) increases. Structurally, alkali ultraphosphate glasses have combinations of Q^3 and Q^2 tetrahedra [47]. With very low Li_2O content the ultraphosphate structure will look similar to that of vitreous P_2O_5 .

2.1.1.3 Metaphosphate glasses

While these glasses ideally have infinitely long chains of $Q^2 PO_4$ tetrahedra, metaphosphate glasses typically have chains and rings that range from 40 to 100 tetrahedra which are terminated by the presence of hydroxyl groups [47]. The properties of these chains are greatly affected by the linking alkali cations and the terminal (non-bridging) oxygen atoms. Thus, the properties of alkali metaphosphates depend more on the P-O-Metal bonds than on the P-O-P bonds. Both diffraction studies [47] and *ab initio* calculations [49] suggest that in the absence of Li the two terminal oxygen atoms of the Q^2 tetrahedron share the π bond and, hence, there exists a resonance between those bonds making the two oxygen atoms indistinguishable.

2.1.1.4 Polyphosphates

Polyphosphate glasses have a higher concentration of alkali oxide substitution ($R > 1$). The chains are shorter and a special phosphate glass having $R = 2$ with the stoichiometry $\text{Li}_4\text{P}_2\text{O}_7$ is referred as the pyrophosphate glass. The structure is dominated by the presence of phosphate dimers (two Q^1 tetrahedra sharing one bridging oxygen).

2.1.1.5 Orthophosphates

Another special case of a polyphosphate glass is the orthophosphate stoichiometry ($R = 3$), where oxygen atoms do not have bonds between PO_4^{3-} tetrahedra, as shown in Figure 2-3. In reality, the glass formation in a binary system is generally limited to $R < 1.2$ to 1.5 but rapid quenching techniques have yielded lithium phosphate glasses with $R = 2.3$. [47]. The orthophosphate stoichiometry ($R = 3$) was only formed in complex systems such as $\text{Li}_2\text{O}-\text{Al}_2\text{O}_3-\text{TiO}_2-\text{P}_2\text{O}_5$. [50]

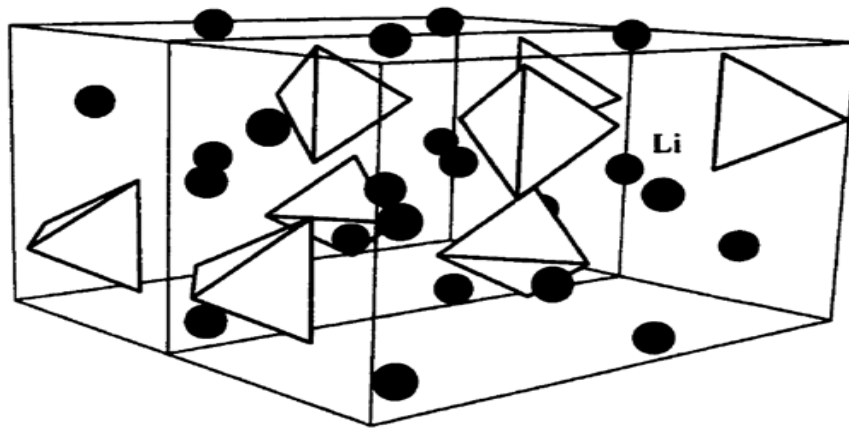


Figure 2-4 shows two unit cells of $\gamma\text{-Li}_3\text{PO}_4$. The Li atoms are shown as isolated atoms (black) and the PO_4 groups are shown as tetrahedra. The PO_4 tetrahedra have no shared oxygen atoms and are therefore isolated from each other

The lithium orthophosphates exist in β , γ , and α crystalline polymorphs with the increase of temperature. The $\alpha\text{-Li}_3\text{PO}_4$ structure has not yet been determined as it cannot be quenched to room temperature. In $\beta\text{-Li}_3\text{PO}_4$ all tetrahedra share only corners and point in the

same direction, whereas in $\gamma\text{-Li}_3\text{PO}_4$ the structure has some edge sharing LiO_4 tetrahedra and some of them point in opposite directions [6]. In the case of $\beta\text{-}$ and $\gamma\text{-Li}_3\text{PO}_4$, Li and P occupy tetrahedral sites and each oxygen is shared by three LiO_4 tetrahedra and one PO_4 tetrahedron.

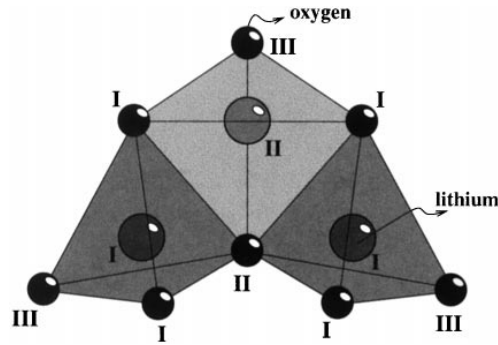


Figure 2-5 is showing $\gamma\text{-Li}_3\text{PO}_4$ structure with 3 LiO_4 tetrahedra (two $\text{Li}_{\text{I}}\text{O}_4$ and one $\text{Li}_{\text{II}}\text{O}_4$) (right). This Figure is reproduced from a reference.[10]

The $\gamma\text{-Li}_3\text{PO}_4$ is a stable phase present between the temperatures range of 520 to 1170°C. Figure 2-4 shows two unit cells of the $\gamma\text{-Li}_3\text{PO}_4$ structure. The unit cell of $\gamma\text{-Li}_3\text{PO}_4$ is orthorhombic. The asymmetric unit cell has 6 atoms along a direction with three tetrahedral cations (Li_{I} , Li_{II} and P) and three oxygen anions (O_{I} , O_{II} and O_{III}). Each $\text{Li}_{\text{II}}\text{O}_4$ tetrahedron edge shares with two corner shared $\text{Li}_{\text{I}}\text{O}_4$ tetrahedra (Figure 2-5). It is important to note that $\gamma\text{-Li}_3\text{PO}_4$ structure has no P-O-P bonding (bridging) but is still stable at the relatively high temperature of 1170°C.

2.1.2 Nitridation of lithium metaphosphates and lithium orthophosphate:

2.1.2.1 Metaphosphates

From Figure 2-2 we can see that pure metaphosphates have only Q^2 type tetrahedra in chain and ring structures. The substitution of the oxygen atoms with nitrogen (nitridation) of lithium metaphosphates significantly increases the crosslinking bonds in the structure. Boukbir *et al.* [51] observed that as the N/P ratio increases, the Li/P ratio decreases, the glass transition

temperature and hardness increase and the thermal expansion coefficient decreases. Larson *et al* also observed these effects and found that nitridation increases the chemical durability [40].

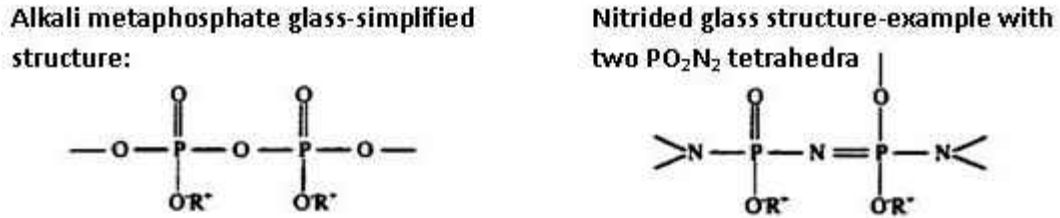


Figure 2-6 Nitridation of a part of metaphosphate chain. The nitrogen atoms that replace oxygen atoms increase the cross-linking between PO₄ tetrahedra [7,51,52].

Reidmeyer *et al*[53] proposed several ways in which nitrogen dissolved in the phosphate melt may increase the crosslinking of the PO₄ network:

- 1) Nitrogen entering the glass is present as N³⁻ ions which then replace the O²⁻ ions according to the reaction $3\text{O}^{2-} (\text{glass}) + 2\text{NH}_3 \Rightarrow 2\text{N}^{3-} (\text{glass}) + 3\text{H}_2\text{O}$. Hence the replacement occurs in the ratio of 3O²⁻ to 2N³⁻ ions.
- 2) Two types of nitrogen bonds, on substituting for the oxygen atoms, are observed in the glass: doubly coordinated (-N=) and triply coordinated (-N<) [7,51–54].
- 3) Nitrogen bonds with the phosphorus in PO₄ tetrahedra by replacing both non-bridging (=O) and bridging (-O-) sites and forms P(O,N)₄ tetrahedra, whereas nitrogen does not replace the oxygen atoms bonded to the metal cations (P-O⁺Me⁺).

The effect of nitridation in the metaphosphate glass structure is illustrated in Figure 2 – 6.

Wang *et al* observed that in the nitrided lithium metaphosphates ionic conductivity is much higher (3.7×10^{-7} S/cm) than that of lithium metaphosphates (2.5×10^{-9} S/cm) [7]. The nitridation of lithium metaphosphates also decreased the activation energy for Li⁺ ion transport from 0.74 eV to 0.57 eV [7]. According to Wang *et al* [7], the reason for high ionic conductivity

could be because of structural distortion arises from additional cross-linking can and a lower electrostatic Li bonding energy when a P-O bond is replaced by a more covalent P-N bond.

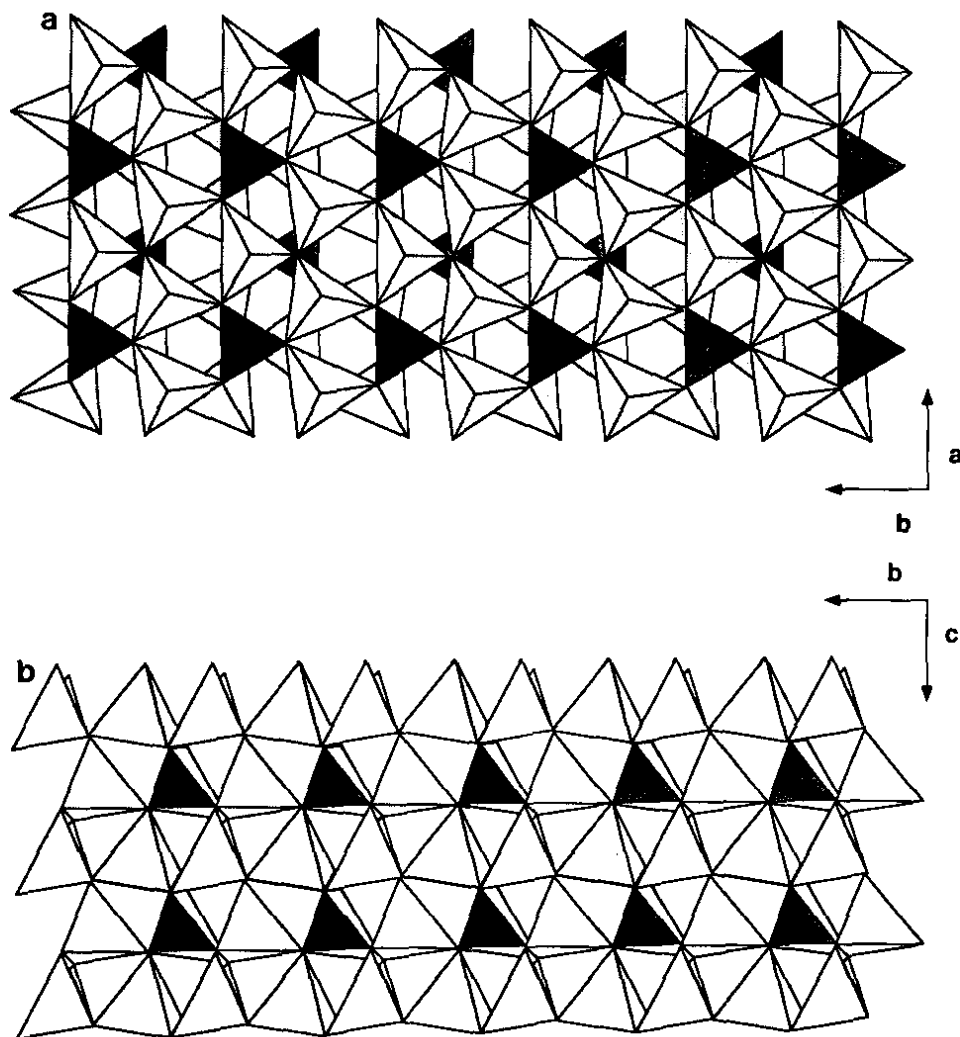


Figure 2-7 Polyhedral crystal structure of β - Li_3PO_4 in (a) (001) shown above and (b) (100) shown below with PO_4 (dark) LiO_4 (light) [6]

2.1.2.2 Orthophosphates

Lithium orthophosphate has the stoichiometry Li_3PO_4 and due to its Q^0 structure there are no oxygen bonds between PO_4^{3-} tetrahedra. Reculeau *et al* [55] reported the phase transformations of crystalline Li_3PO_4 with temperature. The low temperature β phase transforms to γ phase at 500°C and γ transforms to α phase at 1170°C . β - Li_3PO_4 has the Wurtzite crystal

structure with central or tetrahedral sites occupied by Li and P and these tetrahedral share only corners and points in the same direction [6]. Figure 2-7 and Figure 2-8 shows the polyhedral crystal structure of β - Li_3PO_4 and γ - Li_3PO_4 respectively.

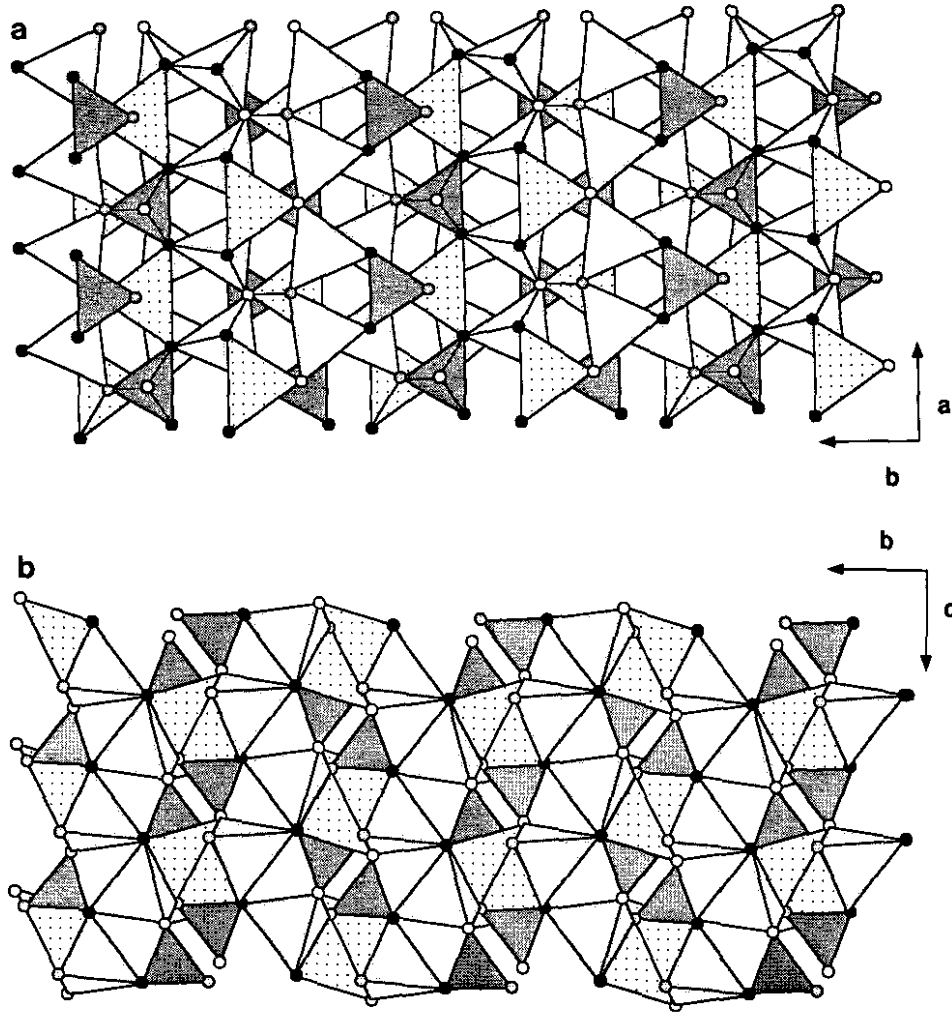
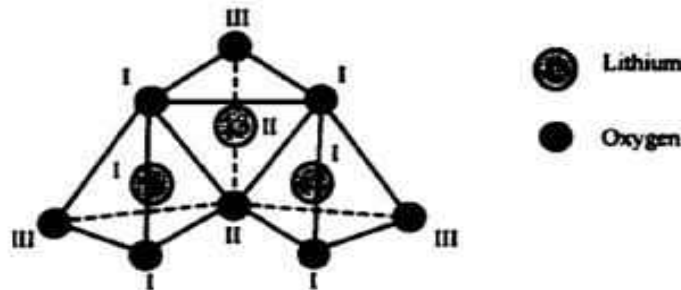


Figure 2-8 Polyhedral crystal structure of γ - Li_3PO_4 in (a) (001) left and (b) (100) right. PO_4 (dark), LiO_4 -(light), $\text{Li}_\text{I}\text{O}_4$ -(gray), $\text{Li}_\text{II}\text{O}_4$ -(dots). O_I , O_II , O_III represents black, gray and white circles respectively[6]

Wang *et al* synthesized polycrystalline LiPON by a solid state reaction between Li_3N and LiPO_3 . [6]. X-ray and neutron diffraction studies on the polycrystalline γ - Li_3PO_4 and nitrated Li_3PO_4 ($\text{Li}_{2.88}\text{PO}_{3.73}\text{N}_{0.14}$) shows that nitrogen incorporation into γ - Li_3PO_4 increases the average Li-O bond distance from 1.99 Å to 2.0 Å causing a structural distortion. This is expected due to

the larger effective ionic radius of N^{3-} (1.32 Å) as compared to that of O^{2-} (1.24 Å). As binding energy is inversely proportional to Li-O bond distance, greater will be mobility of lithium, when there is a weaker bonding between lithium and oxygen. As lithium ions are present in LiO_4 tetrahedron, it must pass through the triangular faces and increase of Li-O bond distance would favor the ionic mobility and conduction.

γ - Li_3PO_4 :



Nitrided form:

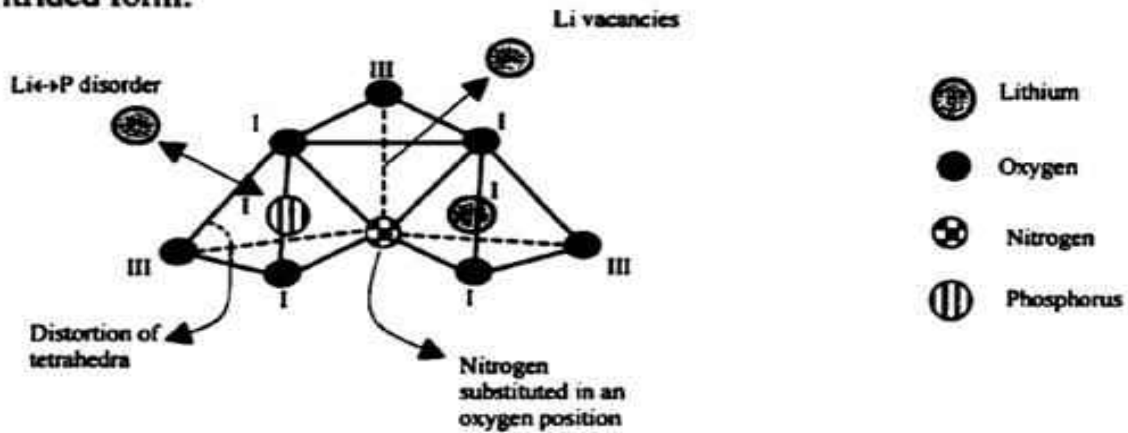


Figure 2-9 Representation of structural difference in γ - Li_3PO_4 and polycrystalline LiPON with γ - Li_3PO_4 structure [6,16]

Although the nitrogen position was not successfully identified in the γ - Li_3PO_4 , he assumed that the addition of nitrogen affects structural distortion and therefore enhancing ionic conduction in nitrided Li_3PO_4 ($Li_{2.88}PO_{3.73}N_{0.14}$). By Rietveld analysis of neutron powder

diffraction data, Wang demonstrated that nitrogen substitution for oxygen led to varying P-O bond distance and angles in the PO_4 and LiO_4 tetrahedra.

High performance liquid chromatography used in this study [6] showed only a PO_4^{3-} peak in case of $\gamma\text{-Li}_3\text{PO}_4$ while the nitrated sample had peaks from $\text{P}_2\text{O}_7^{4-}$, PO_3N , and $[\text{O}_3\text{P-N}=\text{PO}_3]^{5-}$. Since the PO_4 tetrahedra are isolated from each other in $\gamma\text{-Li}_3\text{PO}_4$ there must be some Li-P bonding disorder present to explain the presence of $\text{P}_2\text{O}_7^{4-}$ and $[\text{O}_3\text{P-N}=\text{PO}_3]^{5-}$ anions.. The PO_3N peak, having a nitrogen atom linked to a phosphorus atom and three lithium atoms, is the main difference between the nitridation of $\gamma\text{-Li}_3\text{PO}_4$ and nitridation of lithium metaphosphate glasses.

Surface XPS measurements showed that nitrogen could be incorporated in the form of doubly and triply coordinated nitrogen. The nitrogen atoms were found to occupy oxygen sites in the Li_3PO_4 structure and the measured composition was $\text{Li}_{2.8}\text{PO}_{3.73}\text{N}_{0.14}$, indicating that 3.25% of oxygen vacancies are present and 1.75% of which accommodates nitrogen and the remaining accommodates for 4% lithium. The ionic conductivity measurements on these crystalline samples found that the nitrated Li_3PO_4 had higher ionic conductivity ($\sim 1.4 \times 10^{-13}$ S/cm) than that of polycrystalline $\gamma\text{-Li}_3\text{PO}_4$ ($\sim 1.4 \times 10^{-18}$ S/cm). The nitrogen addition decreased the activation energy, from 1.24 eV to 0.97 eV, increased the Li-O bond length, reduced Li-O binding energy, and enlarged the LiO_4 tetrahedral triangular faces (Figure 2-9). These changes are consistent with higher mobility for lithium ions.

The *ab initio* molecular orbital calculations [10] on the nitrated $\gamma\text{-Li}_3\text{PO}_4$ ($\text{Li}_{2.8}\text{PO}_{3.73}\text{N}_{0.14}$)[6] showed that lithium defects are favored near the nitrogen sites where oxygen was removed.. They studied small molecular clusters $[(\text{HO})_3\text{POP}\{\text{HO}\}_3]^{2+}$ and found that the geometry was affected (increased distortion of LiO_4 and PO_4 tetrahedra) by nitridation

$[(\text{HO})_3\text{PNP}\{\text{HO}\}_3]^{1+}$. LDA calculations indicate a Li/P disorder and P-N-P units formation in the lattice and the lithium mobility was thus enhanced by lithium defects and structural distortion of tetrahedra. In a subsequent study [14] they came to a similar conclusion by calculating the lithium transport activation energy in both nitrated and non-nitrated model clusters for different pathways with a γ - Li_3PO_4 structure. The high ionic conductivity is favored due to lower activation energy of lithium mobility in the defect lattice.

In addition to improving ionic conductivity, nitridation also significantly increased the decomposition voltage of sputter-deposited LiPON thin films (5.5 V) from that of the non-nitrated films (~3.5 V) [9].

The simulation results of Du and Holzwarth study suggested that interstitialcy mechanism could be the favourable means for ionic conduction in crystalline γ - Li_3PO_4 and β - Li_3PO_4 . [56,57]. Effects of oxygen vacancies aids in rebonding of two adjacent PO_4 groups and is further optimized by replacing the bridging -O- with a bridging -N- to form stable bent and straight PNP structures, which in turn stabilized Li ion vacancies. Whereas, on the other hand placing a substit and nitrogen substitution resulted in bent and straight PNP POP defusion N in a tetrahedral phosphate group forms PO_3N that stabilizes interstitial Li ions in these structures. [58,59] In either cases there will be tendencies to trap mobile ions near these defect sites and in general the migration energy for ions to hop near the defects are much lower compared to the migration from near defect site to the bulk material. This could be the large activation energy for the crystalline LiPON ($\text{Li}_{2.88}\text{PO}_{3.73}\text{N}_{0.14}$). In the case of LiPON thin films there is structural disorder in which case both the vacancies and interstitialcy mechanism does not affect the activation energy for the Li ion mobility. They also predicted two new materials with highly symmetric structure, s1- $\text{Li}_2\text{PO}_2\text{N}$ and s2- $\text{Li}_2\text{PO}_2\text{N}$, obtained by replacing nitrogen

in place of oxygen atoms. The s1 and s2 crystalline materials have *Pbcm* and *Aem2* space groups respectively.[60,61]. These materials were never been synthesized and possible synthesis routes were suggested. The study of these materials will deepen the understand of Li ion conduction in LiPON materials.

To better understand the ionic conduction in solid electrolytes, one of the main objectives of this research, a deeper understanding of the ionic mechanism is mentioned here.

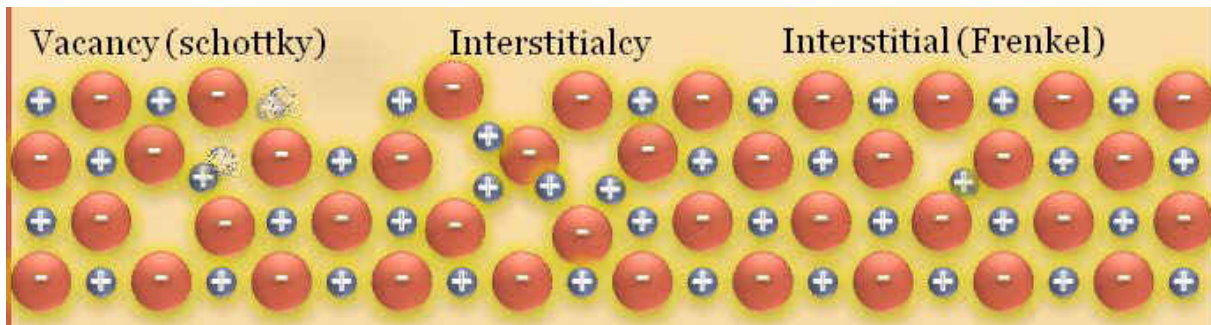


Figure 2-10 Vacancy, interstitial and interstitialcy type diffusion processes in crystalline solids

2.2 Ionic conduction

2.2.1 Motion of Ions in solid electrolytes:

Ions move (conduct) through the solid electrolyte by hopping between the empty sites. Such empty sites, vacancies or interstitial sites, have to be energetically equivalent to each other in order to have the hopping process to be effective. Such diffusion processes are localized and are called as vacancy, interstitial or interstitialcy types when they occur in crystalline solids as shown in Figure 2-10. However, in the case of amorphous solids, the diffusion processes are quite complex and can have more than one type of mechanism. The ions will occasionally encounter non-favorable sites known as ‘bottlenecks’. Hence such motion paths are understood as a succession of energy barriers and wells, shown in Figure 6-4. The net ionic conductivity

from this process is expressed as the product of the mobile ion concentration (c), ionic charge (q), and ionic mobility (μ_i),

$$\sigma = cq\mu_i \quad (2-1)$$

In the hopping process of ionic conduction, two times are considered. First, the actual time, t_j , is the time taken to jump from one site to another is about 10^{-11} to 10^{-12} s and is independent of the material mostly [62]. Second, the average time between successive hops is the ‘site residence time’, t_r , and can vary from nanoseconds in solid electrolytes to geological times in the ionic insulators. The inverse of the site residence time is known as the hopping rate (ω_p), an important parameter. The motions of ions in solids are often modeled by a random walk theory [63], neglecting correlated motions. However, more sophisticated models that include the effect of surrounding mobile ions and glass network relaxation have been developed [49, 50].

From the random walk theory,

$$\sigma = \left(\frac{Ne^2a^2}{k_B T} \right) \gamma * c(1 - c)\omega_p = K\omega_p \quad (2-3)$$

where, N = number of equivalent sites, γ = geometry factor, c = relative concentration of active ions, e = electron charge, a = jump distance between sites, and ω_p = hopping rate. As ω_p is a thermally activated process, the conductivity is temperature dependent:

$$\omega_p = \omega_o \exp\left(-\frac{\Delta G_m}{k_B T}\right) = \omega_e \exp\left(-\frac{\Delta H_m}{k_B T}\right) \quad (2-3)$$

where, $\omega_e = \omega_o \exp\left(-\frac{\Delta S_m}{k_B}\right)$ and ΔH_m is the motion energy (the energy needed to jump to an adjacent site). Not all of the ions present are active and the active fraction may vary with temperature according to:

$$c = c_o \exp\left(-\frac{\Delta G_c}{k_B T}\right) = c_e \exp\left(-\frac{\Delta H_c}{k_B T}\right) \quad (2-4)$$

where ΔH_c is the active ion creation energy. Combining equations (2-2), (2-3), (2-4) and assuming c is much less than 1 we get:

$$\sigma = \left(\frac{Ne^2 a^2}{k_B T} \right) \gamma * c_e \omega_e * \exp \left(- \frac{\Delta H_m + \Delta H_c}{k_B T} \right) = \frac{A}{T} \exp \left(- \frac{E_a}{k_B T} \right) \quad (2-5)$$

This equation introduces the activation energy (E_a) for ionic mobility and can be rewritten as:

$$\sigma_{\text{ionic}} = \frac{\sigma_0}{T} * e^{-\frac{E_a}{k_B T}} \quad (2-6)$$

While the ion flux due to an electric field is characterized by the ionic conductivity, the ion flux due to a mobile ion concentration gradient is characterized by the diffusion coefficient and Fick's first law. In one dimension:

$$J_d = Dq \frac{\partial C_i(x)}{\partial x} \quad (2-7)$$

The ionic diffusion coefficient and the ionic mobility, μ_i , are related by Nernst-Einstein equation [63]:

$$\mu_i = qD/kT \quad (2-8)$$

In phosphate glasses (and also in silicate and borate glasses), it is widely accepted [66–68] that ionic motion is greatly dependent on the presence of non-bridging oxygen (NBO). At low concentrations, the inclusions of alkali oxides in glasses cluster to form localized, isolated regions (lakes) of alkali ions having ionic bonds with NBO. When the alkali ion concentration is increased, the lakes transform to percolating channels. These channels of high alkali ion concentration become paths for the faster diffusion of Li ions as interstitials. A second migration mechanism is exchange. An alkali ion bonded to NBO can migrate to adjacent π bonded NBO site by the exchange of the ionic bond and π bond with the simultaneous motion of the alkali ion position to the previously π bonded site. This bond exchange mechanism occurs uniformly in the

primarily covalently bonded phosphate glass. However, the activation energy for this exchange mechanism is higher than that for interstitial alkali ion transport in a channel and, hence, it is a less important transport mechanism when channels are present. Alkali ion migration happens most readily through these channels of high alkali ion concentration channels. In an amorphous material it cannot be expected that all of these Li ion migration events have the same energy barrier, and hence a range of energy barriers for Li ion conductivity exists and the net effective energy barrier is what is experimentally measured as the activation energy for ionic conductivity. The larger barriers for each mechanism can be understood to be associated with specific defect sites and hence the reduction of defect density is understood to lower the activation energy for lithium ion mobility. The ionic conductivity is further enhanced through the dispersion of multiple diffusion channels throughout the film thickness.[68]

CHAPTER 3 EXPERIMENTAL TECHNIQUES

3.1 Reactive sputter deposition

Sputtering is the process of transferring momentum from an incident energetic projectile to a solid target such that the surface atoms or molecules are knocked out of the target. It has significant advantages compared to that of the evaporation or chemical vapor deposition (CVD) techniques. It allows easy control of alloy composition compared to evaporation, as the sputter yields are similar for all metals and alloys while vapor pressures of the constituents of an alloy may vary greatly. The microstructure of a sputter deposited film can be controlled during its growth through low-energy ion and fast-neutral particle irradiation. Sputtering allows a low substrate temperature during deposition compared to that of CVD.

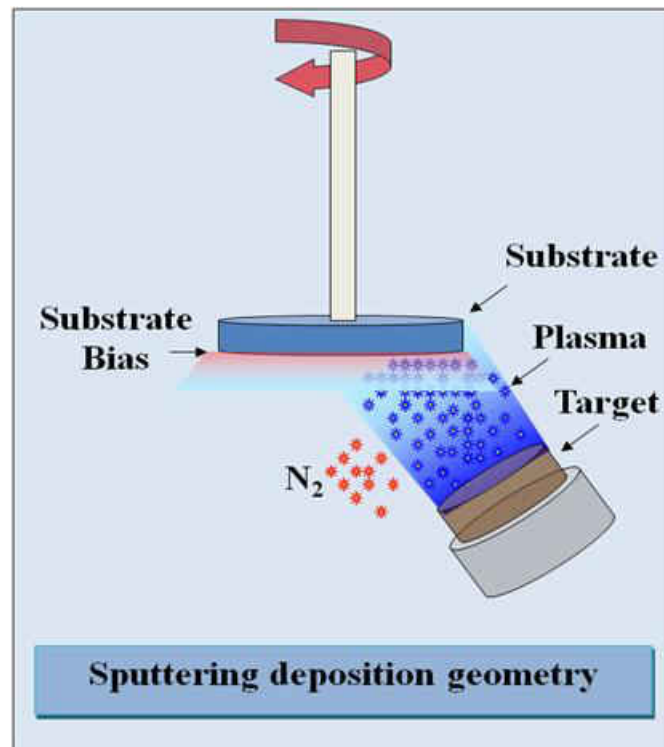


Figure 3-1 The sputtering deposition geometry used axial rotation of the substrate to provide circumferential uniformity of the deposited film thickness from an off-axis magnetron sputter deposition source (one of three is shown). The tilt angle of the deposition source was adjusted to optimize radial thickness uniformity

During sputtering, ions penetrate the target and displace the target atoms along collision cascades. Momentum transfer is principally into the target and the sputter ejection is due to a multiple collision cascade and does not follow from a single binary collision event.

The sputtering yield is the number of sputtered atoms per incident particle [69] and is a time-averaged number as sputtering is a stochastic event involving chance or probability. The sputtered atoms typically are ejected far from the initial collision site [70]. All of these collisions can be considered to be fully elastic hard sphere interactions. There are important trends; $S \propto 1/U$, where U is the surface binding energy, S varies linearly with the incident ion energy, E_i (100 eV to 1000 eV), and S is maximized when the mass of the incident ion (m_i) and the target atom (m_t) are similar, i.e., $S \propto \left(\frac{m_i m_t}{(m_i + m_t)^2} \right) * \left(\frac{E_i}{U} \right)$.

Sputtering atoms from a target is purely a physical process, in which the dynamics are controlled by transfer of momentum from incident ions to the target atoms. Reactive sputtering is a technique in which the film composition is different from that of the target due to the incorporation of gaseous atoms during the sputter deposition process. Reactive RF sputtering is done for LiPON films by sputtering a Li_3PO_4 target in a nitrogen ambient whereas an argon ambient is typically used for non-reactive sputtering.

3.1.1 RF substrate biasing

A RF voltage is applied between the electrically grounded deposition chamber and the substrate (known as substrate biasing) to provide energetic bombardment of the substrate from the surrounding plasma. This voltage induces the formation of a plasma at the substrate surface and the interaction of the substrate with this plasma results in a net DC voltage between the substrate and ground that is known as the bias voltage. This bias voltage represents an average voltage with which the positive ions in the plasma may bombard the substrate. Typically, for a

target voltage of -1000V to -3000V, a bias voltage of -50V to -300V is used. A charge-exchange process occurs in the anode dark space and only a very few discharge ions strike the substrate with full bias voltage energy. Rather, a wide, low-energy distribution of ions and neutrals bombard the growing film. Substrate bias can provide advantages [69] by modifying the properties of the deposited films including: film adhesion, step coverage, density, resistivity, hardness, residual stress, optical reflectivity, and dielectric properties

The effect of bias on film gas content is complex. The fraction of chemically inert gas atoms incorporated is typically proportional to V_b^2 , where V_b is the bias voltage. Some gases that adsorb on the growing film may be removed by low-energy ion bombardment. For example, both weakly bound physisorbed gases (e.g., Ar) and strongly attached chemisorbed species (e.g., O and N on Ta) most likely have large sputtering yield and low sputter threshold voltages and are both readily removed by substrate bias. Gas species with unusually low sputtering yield may be incorporated in to the growing film.

Energetic-particle bombardment prior to and during the film formation and growth makes several changes microscopically. Those changes include removal of contaminants, surface chemistry alteration, nucleation and re-nucleation enhancement, higher surface mobility of adatoms, and increased film temperature with resulting accelerated atomic reaction and interdiffusion rates. As substrate biasing induces such particle bombardment, it results in modification of the film growth properties dependent on the above processes. This includes surface roughening, eliminating interfacial voids and subsurface porosity, creating much finer and more isotropic grain morphology, and the elimination of columnar grains. The LiPON films of our preliminary research were reactively sputter deposited at bias powers of 0W, 5W, 10W, 15W, and 20W.

3.1.2 Process gas pressure

Also, at 10W substrate bias power, process gas pressure was also varied to study the influence of gas pressure on the LiPON film properties.

3.1.3 Deposition temperature

Under a subset of the substrate biasing conditions, the deposition temperatures were varied from room temperature to 500°C.

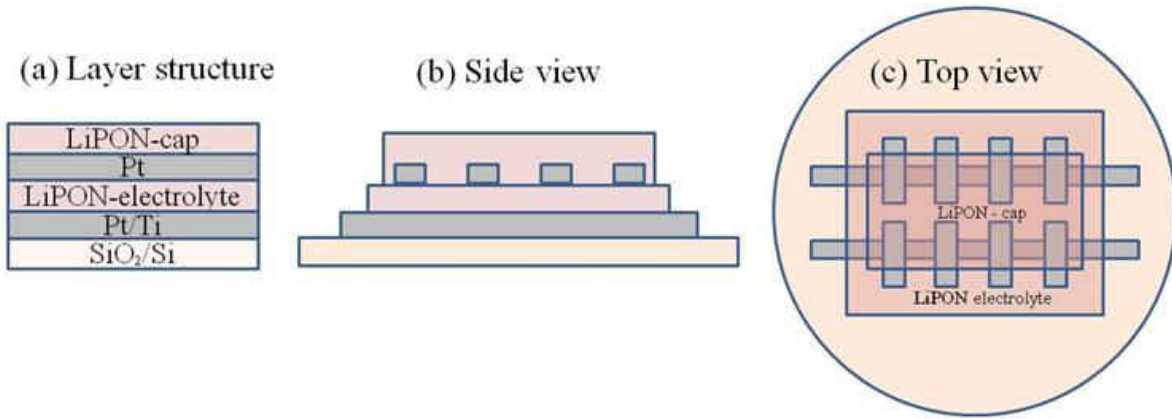


Figure 3-2 A metal/electrolyte/metal layered structure was used for ionic conductivity measurements. (a) is the layer structure, (b) a side view, and (c) is a top view showing the cross electrode geometry.

3.1.4 Sample preparation

The sample top and bottom electrode areas and the leads consisted of patterned Pt with an intervening LiPON solid state electrolyte blanket film layer and were stacked as the metal/electrolyte/metal (MEM) pattern shown in Figure 3–2. Stainless steel contact masks were used to pattern the Pt depositions with the time of laboratory air exposure during the introduction or removal of the masks minimized (typically 60 seconds) to prevent degradation of the LiPON layer. The primary sample preparation sequence started with the deposition of a 10 nm Ti seed layer and 150 nm of Pt for the bottom electrode, both through a contact mask. After removal of the mask the LiPON electrolyte layer was deposited. Subsequently, the top

electrode mask was placed over the sample and 100 nm Pt top electrode was deposited. A second LiPON “cap” layer of 200 nm was deposited on top of the wafer as a last step to serve as an encapsulant to further mitigate atmospheric degradation of the LiPON layer during storage and testing. To provide sufficient LiPON material for the measurement of film density and for the extraction of material for chemical analysis a second deposition run was made for each set of conditions studied wherein a large area single layer blanket film of LiPON was deposited.

3.1.5 Sample processing:

The LiPON films were processed by reactive radio frequency (RF) magnetron sputtering of a lithium ortho-phosphate target of 99.9% purity (from SCI Engineered Materials, Inc.) using 99.999% purity nitrogen as a process gas. The films were deposited onto a silicon wafer substrate having thermally grown oxide surface layer providing electrical isolation from the substrate. A sputter deposition system with three sputtering sources in a confocal geometry was used for the depositions, as shown in Figure 3-1. The tilt angle of the sputter source was optimized to provide radially uniform LiPON film thickness on the substrate ($\pm 3\%$ on whole substrate and less than $\pm 1\%$ on the device area), which was rotated about its axis during the depositions. Preliminary work by the authors identified a target RF power of 150 Watts with a 20 sccm flow of nitrogen gas at 5 mTorr and a target to substrate (substrate center) distance of ~ 12 cm as suitable fixed process parameters for use in the present investigation of substrate biasing, substrate heating, and process gas pressure. [71]

With confocal geometry, the amount of deposit can be radially balanced for uniform thickness by adjustment of the sputtering source angle of tilt, but radially non-uniform plasma bombardment on the substrate surface may still occur. As the target to substrate distance is longer from the center of the substrate holder compared to that of the periphery, a less energetic

bombardment at the center of the substrate and a more energetic bombardment at the film outer diameter is expected for the films deposited without RF bias. Accordingly, a greater film adhesion at the outer diameter is expected compared to the center, and this was observed wherein the LiPON film at the center of the substrate holder was loosely adhered and tended to delaminate. Such occurrence provided the initial motivation for the investigation of RF bias during LiPON deposition.

To improve the film adhesion by providing a more uniform bombardment across the substrate surface, a RF substrate bias was applied to the substrate holder, increasing the density and acceleration voltage of the energetic ions in the plasma beneath the substrate holder. The strength of the bias was controlled by a constant power setting and the bias power levels investigated (with the corresponding bias acceleration voltage ranges tested) were: 0W (15 to 18V of plasma potential), 5W (110 to 125V), 10W (135 to 155V), 15W (165 to 185V), and 20W (195V to 215V).

Indirect heating of the substrate surface (200°C to 500°C) by halogen lamps irradiating the backside of the Inconel substrate holder was also used during deposition to observe its influence on the film properties.

3.2 Characterization

Amorphous LiPON thin films, lacking crystalline order, were expected on this study based on the work of others[5,22,24,27,30,31] and it was confirmed in this work by X-ray diffraction and transmission electron microscopy of selected samples. In addition, characterization of the other aspects of the sputtered LiPON thin films using various techniques to determine the thickness, stress, ionic conductivity and its activation energy, lithium to phosphorus (Li/P) atomic ratio, bonding information, film density, and density of defects was

performed. The film thickness and optical properties were measured using a spectroscopic ellipsometer in the visible to ultraviolet (UV) range. The stress in the LiPON thin films was determined by measuring the change in radius of curvature of the substrate before and after the film deposition. The ionic conductivity of the LiPON films was determined by measuring the impedance of metal/LiPON/metal capacitive thin film structures as a function of frequency, a technique known as electrochemical impedance spectroscopy. In this technique, a signal voltage over a wide range of frequency is applied to the metal-electrolyte-metal structure, and the phase shift and amplitude (i.e., real and imaginary parts) of the signal current at each frequency are measured to give the impedance at that frequency, from which the ionic conductivity is determined. The activation energy for the lithium ion conduction was calculated by fitting the ionic conductivity at four different temperatures (i.e., 21°C, 30°C, 40°C, and 50°C) to an Arrhenius temperature dependence. The Li/P atomic ratio was determined using inductively coupled plasma-optical emission spectroscopy (ICP/OES). Prior to this analysis, samples were digested using a method developed specifically for LiPON samples. The film density was determined from the film mass and volume. The film mass was calculated as the difference between the wafer mass measurements with and without the film present, and the film volume was calculated from the film area and thickness.

3.2.1 Spectroscopic ellipsometry

A spectroscopic ellipsometer was used to study the thickness and optical properties of LiPON films and an ellipsometer set-up is shown in Figure 3-3. It measures the change in polarization of the irradiated light, at a fixed angle, that reflects from or transmits through a thin film material. This polarization change is represented by an amplitude ratio, Ψ , and a phase difference, Δ . However, the response of these measurements is dependent on the film's

thickness and its optical properties (i.e., refractive index, n , and extinction coefficient, k). Additionally, other properties including composition, crystallinity, roughness, and doping concentration can be inferred.

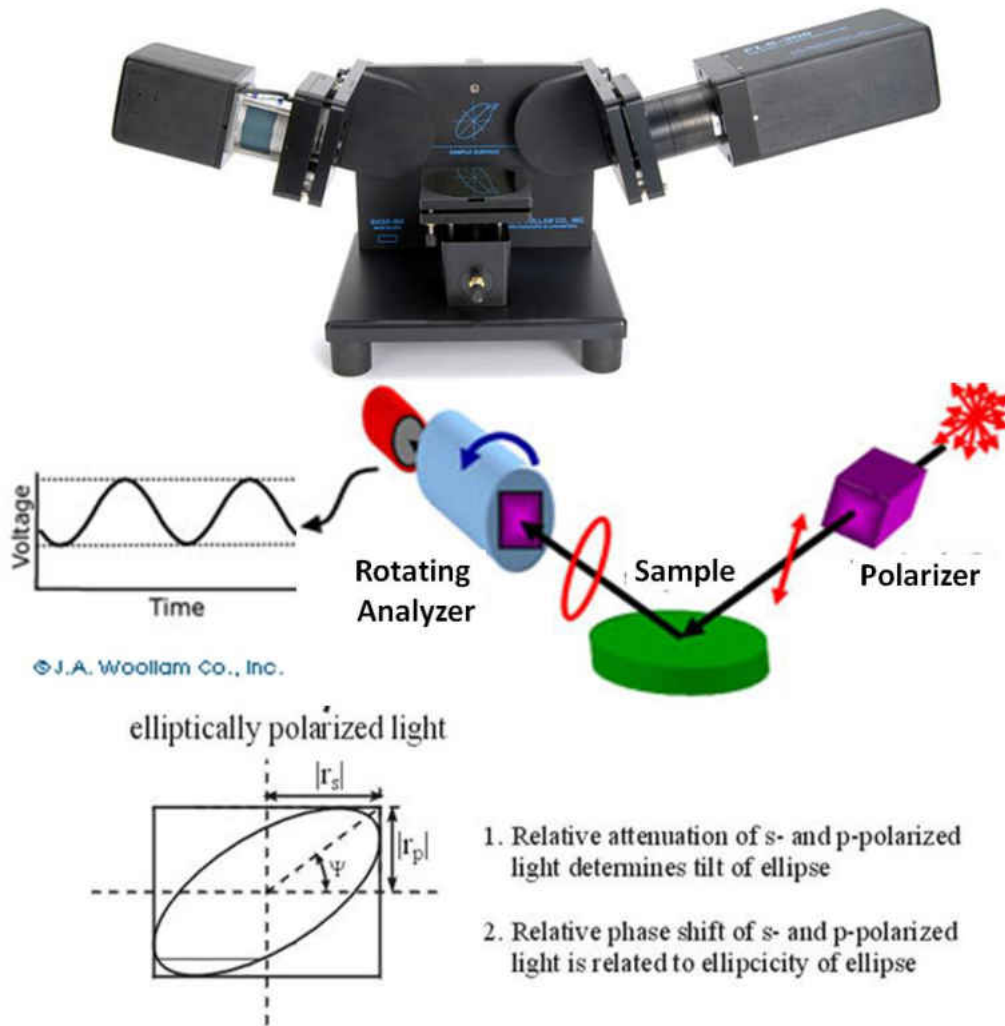


Figure 3-3 Ellipsometry set-up.

Film thickness is obtained by the interference of light reflected from the surface and that reflected from the sub-surface and requires that the film be sufficiently transparent (or sufficiently thin) for the sub-surface reflection to reach the detector. Such interference can be constructive or destructive, which accounts for the amplitude and the phase relationships

between the reflected light from the surface and subsurface. Phase information, given in terms of Δ , is very sensitive to films of even sub-monolayer thickness. Ellipsometry can measure film thicknesses from sub-nanometers to a few microns, with limitations. When the film thickness is several tens of microns, the interference of the oscillations will be increasingly difficult to resolve, unless long infrared wavelengths are used. For an optically absorbing film the maximum thickness that can be measured is limited by the lack of intensity of the sub-surface reflection. In this case, measurements can be done within a spectral region with lower absorption. For example, an organic film is transparent at mid-visible wavelengths, while it may be strongly absorbed at non-visible wavelengths. Metals absorb strongly at all wavelengths and typically have a maximum layer thickness that can be determined below 100 nm.

For our study a fixed angle stage JA Woollam M2000 ellipsometer was used. The ellipsometer was operated by using the WVASE software for data acquisition and analysis.[72] The multiple layers of the sample were modeled using the Cauchy and Urbach equations for the optical constants of the LiPON layer and using published values for the optical constants of the SiO₂ layer and the silicon substrate.[73]

The Cauchy equation was used to model the index of refraction in the ultraviolet and visible wavelength regions, as given by

$$n(\lambda) = A_n + \frac{B_n}{\lambda^2} + \frac{C_n}{\lambda^4} \quad (3-1)$$

where A_n is a constant term and the B_n and C_n terms provide for wavelength (λ) dependence.

In order to model the absorption in the ultraviolet wavelength region the Urbach equation was used:

$$k(\lambda) = A_k e^{B(E-E_b)} \quad (3-2)$$

where A_k is the extinction amplitude, B is the exponent, E is the photon energy, and E_b is

the band edge energy expressed in electron volts (eV). The LiPON layer's optical properties are then modeled as a number of oscillators to fit the optical constants of the film, maintaining consistency between the fit parameters and the Kramers-Kronig relations[74,75].

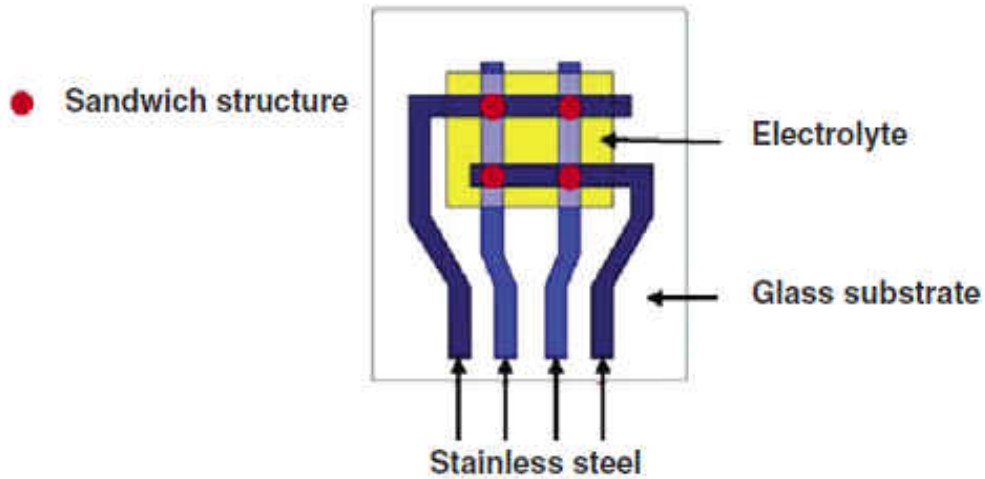


Figure 3-4 Overlapping top electrodes of adjacent devices in ionic conductivity measurement.[33,76]

The optical properties of an amorphous film can be used to understand the defects or irregularities in its bonding as has been done extensively for amorphous silicon, where defects are observed as electron states between the conduction and valance bands.[77] These bonding defects give rise to an “optical tail” or “Urbach tail[78]” in plots of the absorption coefficient, $\alpha = 4\pi k/\lambda$, as a function of photon energy. Equivalently, tails in plots of the extinction coefficient, k as a function of wavelength are observed as indications of optically active defects in the amorphous structure. These defect states between the conduction and valance bands of an amorphous material also serve to narrow the effective band gap and Tauc’s relation is commonly used to determine the effective optical band gap in a disordered or amorphous material: [79]

$$(\alpha * hv) = A * (hv - E_g)^2 \quad (3-Error!)$$

**Bookmark not
defined.3)**

where $h\nu$ is the photon energy, A is a constant and E_g is the optical band gap. The band gap is calculated, from the extrapolation of a straight line to $\alpha = 0$, at $h\nu = E_g$, by plotting $(\alpha * h\nu)^{0.5}$ against $h\nu$. The number of optically active defects per unit volume is expected to be proportional to the penetration depth, δ , which is given by $\delta = 1/\alpha = \lambda/4\pi k$.

3.2.2 Electrochemical impedance spectroscopy

Ionic conductivity is measured by a technique called electrochemical impedance spectroscopy (EIS) using a Solartron 1260 impedance analyzer.

Here, an input sinusoidal voltage is applied to a metal-electrolyte-metal (MEM) device, while the output current is measured at the same frequency of the input voltage but not in the same phase. These measurements are done over a range of frequencies. The measured current (I) is related by the sample impedance (Z) to the applied voltage (V), all of which are functions of excitation frequency, hence

$$Z(\omega) = V(\omega)/I(\omega) \quad (3-4)$$

where Z , V and I are all complex quantities. It is one of the most important techniques for studying interfaces in electrochemistry.

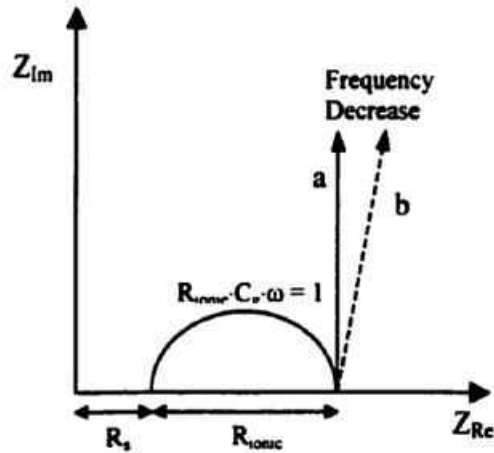


Figure 3-5 Impedance-Frequency response, Nyquist plot, of a typical MEM device. Dotted line show imperfect blocking electrodes

In this research, EIS is mainly used to calculate ionic conductivity and activation energy for LiPON films in the MEM device configuration. Figure 3–2 shows a simple sample structure that consists of LiPON sandwiched between two ion-blocking platinum contacts. Note that each element to be measured is electrically isolated as shown in Figure 3-2c). Other sample geometries, an example shown in Figure 3–4 reproduced from the work of Fleutot et al.[33,76], allow multiple elements to form electrical series-parallel circuits that can result in measurement error for the intended element. The modeling software ZView was used for fitting the data to obtain electrolyte resistance from which ionic conductivity was calculated.[80]. The results of the impedance measurements are generally shown with a Nyquist plot of real and imaginary impedances or a Bode plot with impedance against frequency. A Nyquist plot is shown in Figure 3–5. In this Figure the imaginary part of the impedance is plotted against the real part while the frequency is scanned from 10^{-2} to 10^6 Hz. At very high frequencies, only the series resistance is significant (Z_{im} is zero) and this allows measurement of R_s . The semicircular region is from the intermediate frequencies where the capacitance and ionic conductance have significant contributions to the total impedance. R_{ionic} is the diameter of this semi-circle, with its first

intercept on the abscissa axis at R_s and with a Z_{im} maxima at $R_{ionic} \cdot C_g \cdot \omega = 1$. At lower frequencies a straight vertical line (shown as a solid line, a, in the Figure 3-5), corresponding to a pure capacitive response occurs. A deviation from the ideal behavior when the metal contacts are not purely blocking, is shown by the dashed vertical line, b, in Figure 3-5. Such deviations can be present when a rough interface is present leading to a non-homogeneous current flow across the interface.[81]

A circuit model, shown in Figure 3-6 is used for fitting the data in the Nyquist plot and obtaining ionic resistance of the electrolyte. The circuit model is chosen to include elements which relate to the conduction mechanism in the device being studied. Here, R_s is the series resistance of the leads and the thin film metal contacts, C_{in} is the capacitance due to opposite charge build up in either sides of blocking interface when the voltage is applied across the device, C_g is the geometric capacitance of the MEM device and R_{ionic} is the electrical resistance of the LiPON film which is presumed to be the Li ion contribution due to the small electronic conductivity reported for LiPON.

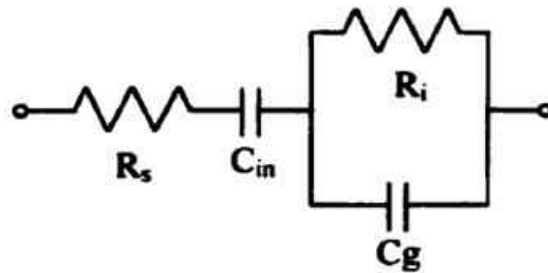


Figure 3-6 Circuit model of an MEM device

In order to calculate the ionic conductivity from imperfect electrode interfaces that gives double layer capacitance, a modified circuit model was used as shown in Figure 3–7. This model is based on the work of Jamnik and Maier[82], Lai and Haile[83], and Donnelly and Randell[84].

In this circuit model, a constant phase element (CPE-bulk) was used instead of bulk capacitance. An additional resistance (R-intr) with a CPE circuit (CPE-intr) was added to accommodate the interfacial or reactive layer. Warburg impedance (diffusional behavior) and a double layer capacitance (C-DL) were added in parallel to account for the contributions from the electrode interface. The contact lead resistance (R-contact) was also included in this model.

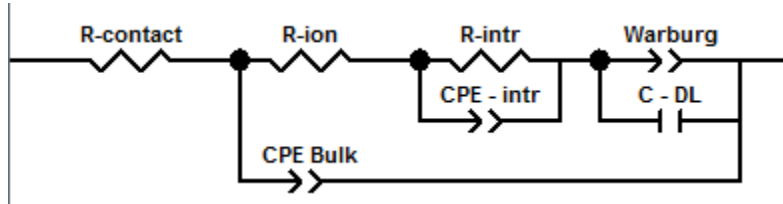


Figure 3-7 The equivalent circuit model used to extract ion transport resistance, R-ion, to determine the ionic conductivity of LiPON films. The other circuit elements are identified in the text.

The concept of double layer capacitance involves the presence of electrical potential difference at the interface between metal and electrolyte. If metal has negative potential or full of electrons, the adjoining layer (positive) is typically the width of ionic radius formed due to contact adsorptions of cations. This adjoining layer is called an inner Helmholtz layer and an outer Helmholtz layer that exists after is due to electrostatic adsorption. The farther end of diffused layer is a uniform mixture of anions and cations. The capacitance of the double layer is calculated from both Helmholtz layer and the diffused layer. Grahame[85] extended the work of Stern's model which combined the models of Helmholtz, Gouy and Chapman.

When the electrolyte resistance is calculated from the Nyquist plot of EIS spectra, the ionic conductivity is calculated from the equation below:

$$\sigma = \frac{1}{R_i * A} \text{ S/cm} \quad (3-5)$$

The activation energy was calculated from Arrhenius plots of lithium ion conductivity at four different temperatures (21°C, 30°C, 40°C, and 50°C) using the Arrhenius equation,

$$\sigma = \sigma_0 e^{\frac{-E_A}{k_B T}} \quad (3-6)$$

where σ is the ionic conductivity in S/cm, σ_0 is the constant prefactor, E_A is the activation energy in eV, k_B is the Boltzmann constant (8.617×10^{-5} eV K⁻¹), and, T is the temperature in Kelvin.

The EIS spectra were obtained for the LiPON films at temperatures of 21°C, 30°C, 40°C, and 50°C. Plotting the log of the ionic conductivities against inverse temperature gives a slope from which activation energy can be calculated using the following equation:

$$\ln(\sigma_T) = (-E_A)/kT + \ln(\sigma_0) \quad (3-7)$$

3.2.3 X-ray photoelectron spectroscopy

The principle of X-ray photoelectron spectroscopy (XPS) is the photoelectric effect which is shown in Figure 3–8. The photoelectric effect was first documented by Hertz in 1887 and was explained mathematically by Albert Einstein in 1905 (Nobel Prize in 1921) by proposing the concept of light as quantum packets or photons. The photoelectron emission was first used as an analytical tool, electron spectroscopy for chemical analysis (ESCA) by Kai Siegbahn[86], for which he received a Nobel prize in 1981. XPS is used to perform both qualitative and quantitative surface analysis of materials.[87] The sample is irradiated with X-rays at specific photon energy, $h\nu$, typically larger than the binding energy, E_B , of the electron from its occupied state. The kinetic energy, (E_k) of the ejected electron, is thus related by

$$E_B = h\nu - E_k - \varphi \quad (3-8)$$

where φ is the work function, which is the potential difference between the Fermi level of the sample and the vacuum level. The vacuum level depends on both the sample and the spectrometer. Photoelectrons are emitted at different energy levels that vary according to the atomic species and local bonding. The chemical states of the elements that are present can be quantified by an analysis of the electron energy spectra.

The bond structure and associated elemental composition of the LiPON films were studied by ESCALAB-220Xi, an x-ray photoelectron spectrometer. The system was operated using the Avantage software and the samples were irradiated from an Al-K α monochromatic X-ray source to a spot of 150 μm by 800 μm with a residual vacuum of 8×10^{-9} Torr or better. The survey spectra were obtained (between 0 eV and 1210 eV) with a pass energy of 50eV and the high resolution scans were obtained with 20eV pass energy. A basic configuration of ESCALAB 220 XI and its schematics are shown in Figure 3–9.

A depth profile was obtained (with an EX05 argon ion source) by collecting high resolution scans after argon ion etching at fixed three minute time steps from the top electrode through the electrolyte and to the bottom electrode (the electro-chemical impedance spectroscopy sample structure). The EX05 argon ion source was maintained with a fixed beam energy of 3 kV and a beam current of $\sim 1\mu\text{A}$ and was differentially pumped to maintain the base pressure at $\sim 5 \times 10^{-7}$ Torr or better during ion milling. The condenser and focus lens was fixed for all the scans. The ion milling was rastered a sufficiently large area such that the X-ray irradiated area of the sample could be easily positioned within the rastered area to insure that all photoelectrons captured were from a uniform depth of the etched region.

The high resolution scans include Li 1s, P 2p, O 1s, N 1s, Ar 2p, Pt 2p, Si 2p, and C 1s. C1s (284.6 eV) was used as the reference voltage for surface scans and the Ar 2p (241.9 eV for Ar 2p $_{3/2}$) was used as the reference voltage in depth profile scans, however a charge neutralizer was not used and additional shifts in energy scale were observed due to surface charging. The shifts in electron energy scale for the spectra obtained during depth profiling were corrected by use of the Ar2p peak as the reference energy. It should be noted that all of the peaks present in any spectra taken were found to shift uniformly. Hence, the deconvolution of the spectra into

distinct bonding types was not affected by the charging induced energy shifts. Small changes in the energy scale shift were observed over time (between acquisitions of different spectra) and these resulted in some uncertainty in peak positions, as given in the data presented. We identify the weak peak of the P2p spectra that has higher intensity with increased sample deposition temperature to be reduced phosphorus (bonded to neighboring phosphorus atoms with possibly no valence) due its position relative to the primary phosphate peak.[87] The weak peak in the N1s spectra that we observed has been reported previously in the literature but not identified.[7] The weak peak in the Li1s spectra is identified as lithium bonded to oxygen, as in Li_2O , due to its position relative to the primary peak of Li bonding in LiPON.[87,88]

For each condition, data was also obtained on the blanket film adjacent to the device in order to compare to prior published works. The data were exported as text file and converted to vamas files in Casaxps software[89], for data analysis. As described below, an average spectrum (of consistent profiles within the film) was then created using the Expression calculator in the software, to provide information representative of the bulk of the LiPON layer.

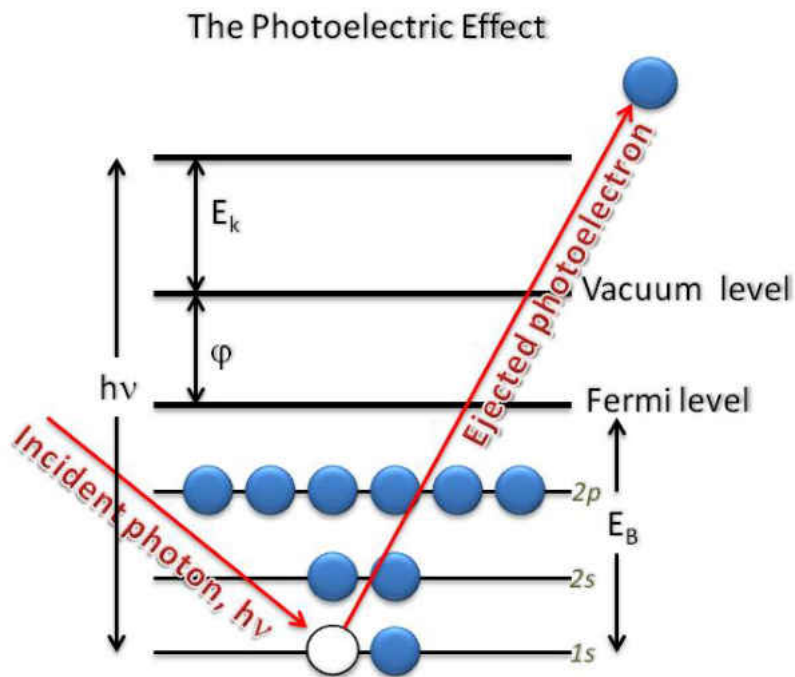


Figure 3-8 The photoelectric effect in X-ray photoelectron spectroscopy

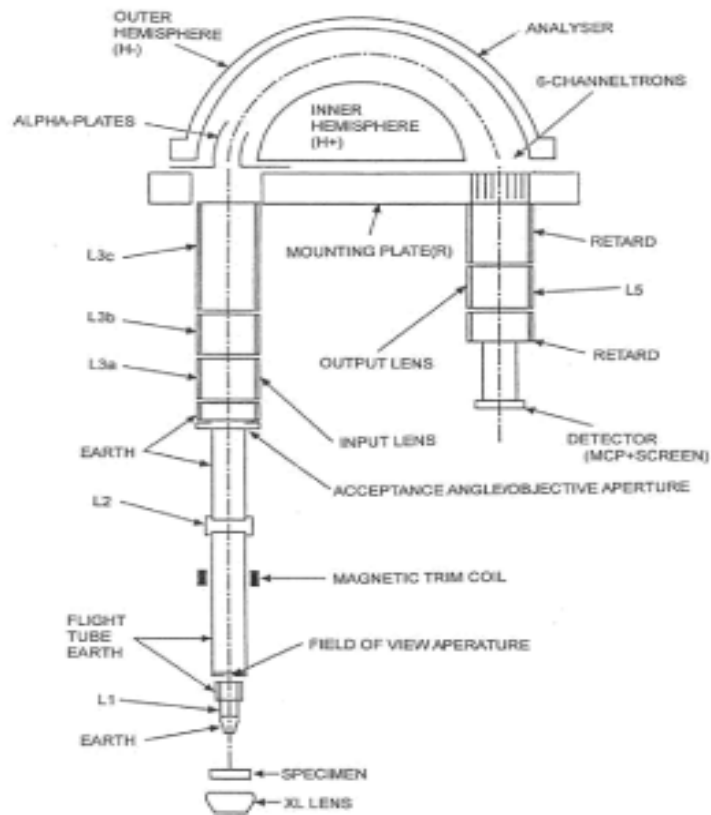
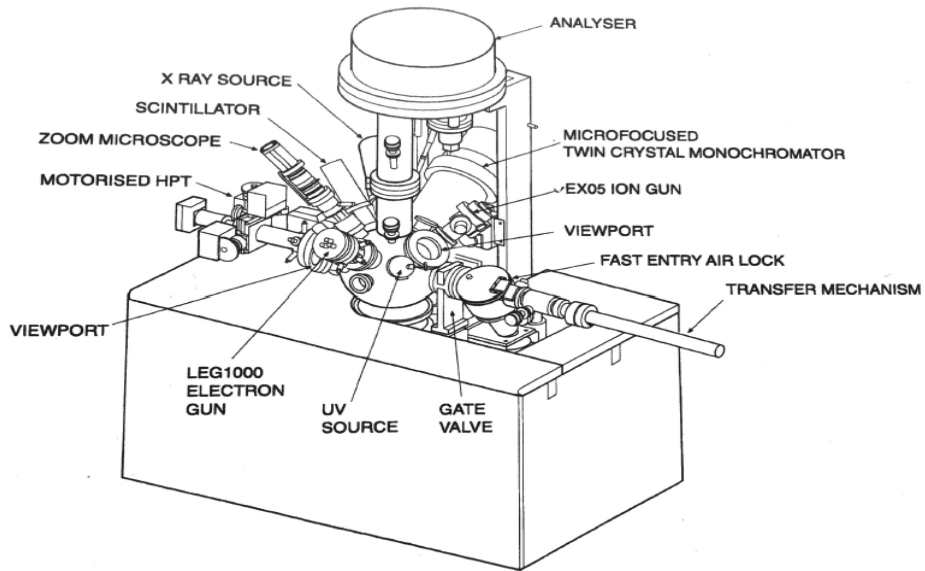


Figure 3-9 A basic ESCALAB 220XI configuration and schematics

3.2.4 Secondary ion mass spectroscopy

The elemental composition as a function of depth below the surface is measured by secondary-ion mass spectroscopy (SIMS). In this technique, a high energy primary ion beam is

used to sputter an area of the sample and the interaction of these primary ions with the sample surface has three major effects: (1) mixing of upper layers of the sample thereby amorphizing the surface, (2) implantation of atoms from the primary ions into the sample, and (3) ejection of secondary particles, such as atoms and small molecules. The ejected secondary particles contain electrically neutral as well as charged species. The secondary ions that are ejected from the surface are extracted to a spectrometer that determines the charge to mass ratio of the ions. The extraction employs an electric field between the sample and an extraction lens. The accelerated secondary ion beam is then led into a mass spectrometer to sort the ions according to their mass (and energy) and is then counted by an ion detector. Ion detector could be an electron multiplier, a Faraday cup or a channel plate. The count rates of various secondary ions give composition information in the sputtered area. The size of the primary ion beam diameter, which is typically in the micro-meter scale, determines the lateral resolution of this technique.

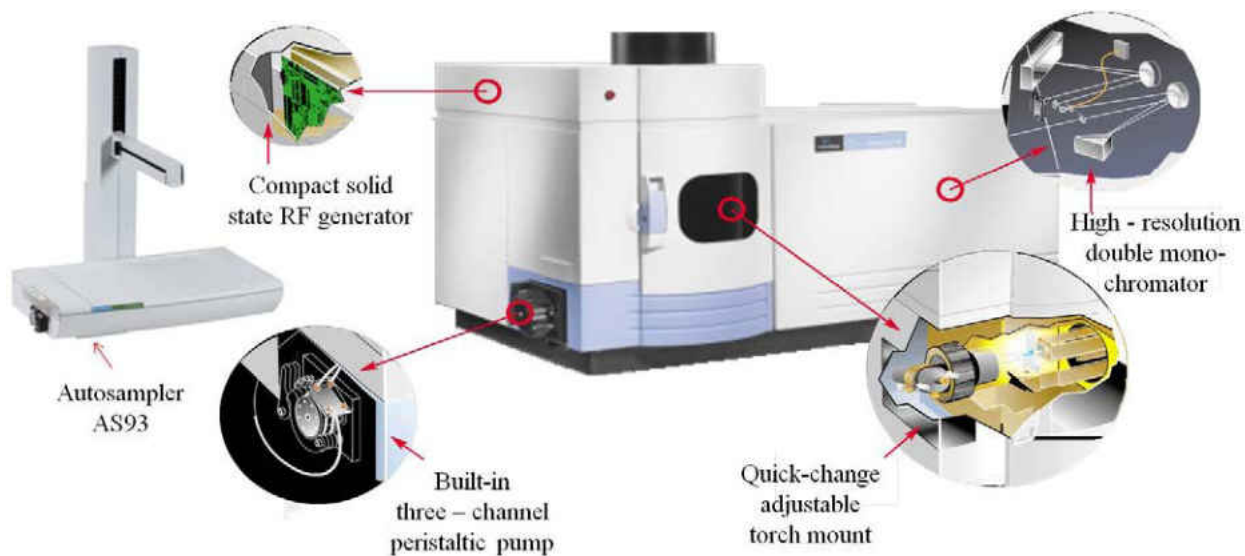


Figure 3-10 Perkin Elmer – Optima 2100 DV ICP/OES spectrometer

3.2.5 Inductively coupled plasma – optical emission spectroscopy

ICP/OES is a widely used technique for lithium and phosphorus detection in LiPON films. In ICP/OES, the intensity of light emitted from the ions in a plasma at characteristic wavelengths is measured. Elemental concentrations of ions from the film that were introduced into the plasma are then obtained from the light intensity measurement by comparison to the reference samples[29].

The average lithium (Li) to phosphorus (P) atomic ratio was determined using a Perkin-Elmer Optima 2100 DV ICP/OES system with AS-93 Plus Autosampler and Winlab32 software for performing elemental analysis. Figure 3-10 shows the configuration of the Optima 2100 dv spectrometer. Wavelength selection is achieved with simultaneous rotation of both prism and grating through scanning sequentially and for each element the maximum rotation is not more than $\pm 2^\circ$, the average wavelength selection is less than 2 seconds. The dual monochromator uses two high slits with no loss of image quality for high optical throughput and part of the slit height is used for the simultaneous neon reference spectrum towards wavelength correction. Two slit widths are available and each width setting is selected automatically by the system for UV and visible wavelengths. The CCD array detector analyzes the complete analyte spectrum and the automatic dual viewing mechanism ensures the lowest detection limits and widest working ranges. The plasma source of Optima 2100V is a 40 MHz solid state RF generator that can be operated between 750 to 1500 Watts in 1 Watt increment at 81% efficiency. The temperature of the plasma is 8000K to 10000K. The RF power from the solid state oscillator ionizes the argon in the torch and thereby producing the plasma and excites the atoms of the sprayed liquid to emit energy as photons at their atomic wavelengths. This photons are detected optically and measured electronically in dual views either radially adjacent to the plasma (to minimize the

matrix effects) or axially above from the plasma (for lowest detection limits), as shown in Figure 3-11. A simultaneous dual viewing ICP instrument can measure 60 different elements at the same time without compromising the detection limits. The peristaltic pump, integrated with 3 channels, can be set at 0.2 to 5 mL/min with 0.1 mL/min increments and uses a 0.76 mm (0.030 inch) inner diameter tube.

A digested sample (LiPON films in nitric acid) was introduced at 1.5 mL/min into a cyclonic spray chamber through a Meinhard Type C concentric glass nebulizer for aerosol generation. The nebulizer flow rate was set at 0.7 mL/min. Then sample aerosol was carried and injected into the plasma within a tulip quartz torch through an alumina injector. The plasma parameters were set at 1400 Watts of RF power with 15 L/min of plasma flow and 0.2 L/min of auxiliary flow. In the plasma, sample molecules were ionized and subsequently produced ionic optical emission spectra which were detected using a scanning charge-coupled device array detector. Lithium was measured at 670.8 nm using the radial window, while phosphorus was detected at 213.6 nm using the axial window.

A digestion method prior to the ICP/OES analysis was developed to reliably extract the target metals from the LiPON sample. The method developed consisted of digesting the sample in 5% HNO₃ at 95°C of 50 mL for one hour and this was compared to a previously published digestion method in 20% HNO₃ at 75°C by Kim.[29] These two methods were quantitatively compared by digesting known amounts (0.30 mg or 0.31 mg) of Li₃PO₄ powder (99.9% purity, Sigma Aldrich) and analyzing for Li and P by ICP/OES. The results were assessed based on accuracy (%Recovery of the actual lithium and phosphorus measured as compared to the standard Li₃PO₄) and precision (%RSD of duplicate samples). The acceptable values for %Recovery range from 80 to 120% with ≤ 10% for %RSD. The developed digestion method

showed average recoveries of 92% (n=3) with 3 %RSD for Li and 78% (n=3) with 4 %RSD for P. These results, especially %Recovery, are better than the published method which showed 87 %Recovery (n=3) with 1 %RSD for lithium and 73 %Recovery (n=3) with 3 %RSD for phosphorus. Therefore, the 5% HNO₃ at 95°C for one hour digestion procedure was adopted for the analysis of the LiPON thin film samples.

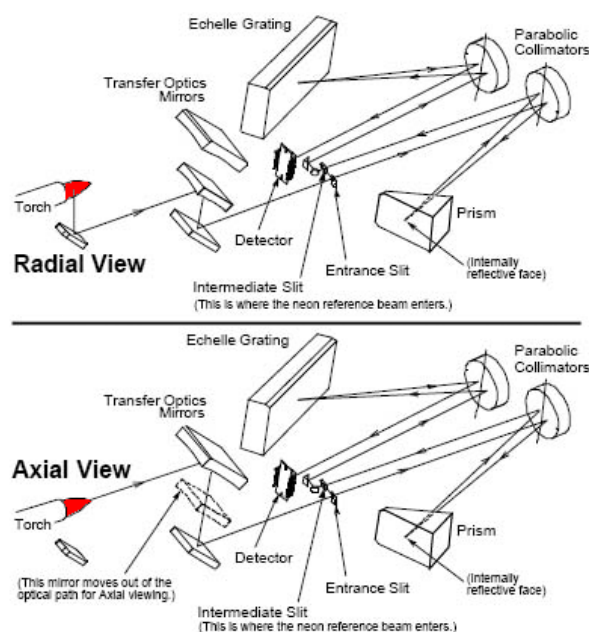


Figure 3-11 Radial view and axial view schematics in Optima 2100 DV ICP/OES spectrometer

Applying the developed digestion procedure in the analysis of Li and P of LiPON thin film samples showed an average of 92 %Recovery (n=3) with 2 %RSD for lithium and 92 %Recovery (n=3) with 1 %RSD for phosphorus. There was no Li or P detected on the blank while the spiked blank showed 91 %Recovery for Li and 89 %Recovery for P. These values are within the acceptable limits for accuracy and precision. Li and P were also analyzed by an external certified lab and compared to in-house analyses. Assessments of the results were also based on %Recovery and %RSD. The results for the external certified laboratory (n=2) showed 80 %Recovery with <1 %RSD for lithium and 86 %Recovery with 8 %RSD for phosphorus.

The in-house results (n=3) were 94 %Recovery with <1 %RSD for lithium and 103% Recovery with 1% RSD for phosphorus. Based on these results, the digestion procedure developed prior of ICP/OES analysis of lithium and phosphorus is applicable for LiPON samples.

3.2.6 Stress measurements

The stress developed in the LiPON films during deposition is measured by the change in curvature of the film's substrate before and after film deposition using a Tencor Flexus FLX 2320 instrument. The curvature change is concave for tensile stress and convex for compressive stress.

The wafer with blanket LiPON films were used for the stress measurements and four radial scans through the center of the wafer at 45 degree separations were used to determine the average change in the substrate radius of curvature. Figure 3–12 shows the position of 3 inch diameter silicon substrate with thermally grown oxide on to the substrate holder upon deposition. Here the substrate is positioned between center and the edge of the holder and hence the average stress values area calculated for the four position scanning explained above. When there is delamination in case of no substrate bias or 0 Watt substrate bias sample, position 1 is neglected and the average stress is calculated from 0, 2 and 3 positions. The Stoney[90] formula was then used to calculate the biaxial stress state of the sputter deposited film:

$$\sigma_f = \frac{1}{6R} * \frac{E_s d_s^2}{(1-\nu_s) d_f} \quad (3-7)$$

where σ is the film stress, $\frac{E_s}{(1-\nu_s)}$ is the biaxial elastic modulus of the substrate [1.805×10^{11} Pa for Si (100)[91]], d_s is the substrate thickness, R is the change in the radius of curvature, and d_f is the film thickness.

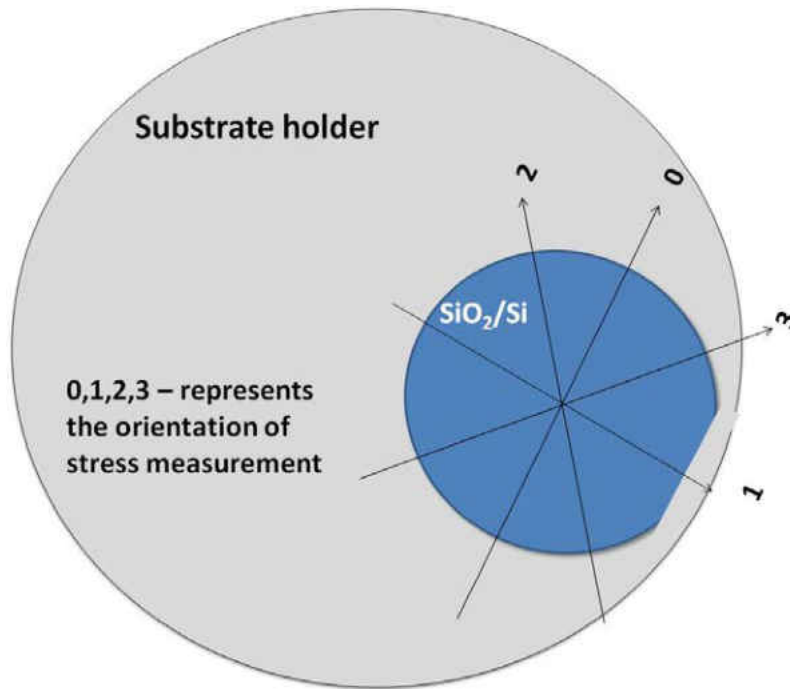


Figure 3-12 shows the sample placement on the substrate holder during LiPON film deposition for stress measurements.

CHAPTER 4 PRELIMINARY RESULTS AND DISCUSSION

4.1 Thickness measurements

Spectroscopic ellipsometry was used to characterize the thickness of the LiPON films deposited on a 6" diameter wafer. The gun tilt angle in the sputtering system was optimized to give uniform thickness of the deposited film across the wafer. Figure 4-1 shows the film thickness plotted against the distance from the wafer center for three gun tilt positions. Depositions made with the medium tilt position show uniform thickness from the center to the periphery.

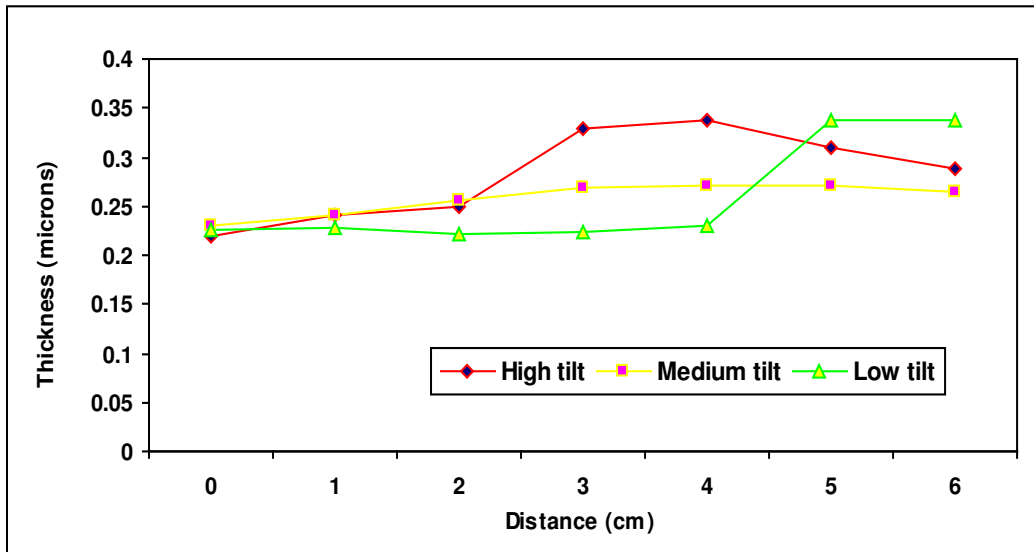


Figure 4-1 Thickness profile Vs Gun tilt

Initially, films deposited on full wafers had poor mechanical stability and underwent delamination at the center of the substrate. This delamination was successfully eliminated by applying RF bias to the substrate during deposition. Substrate bias powers of 0, 5, 10, 15, and 20 Watts were used to study its effect on improving film stability and ionic conductivity. RF substrate bias can remove film material from the substrate and hence reduce the net deposition rate of the film. Figure 4-2 shows the net deposition rate at these substrate bias powers. Figure

4-3 and 4-4 shows a cartoon displaying delaminated and non-delaminated film on silicon substrate respectively.

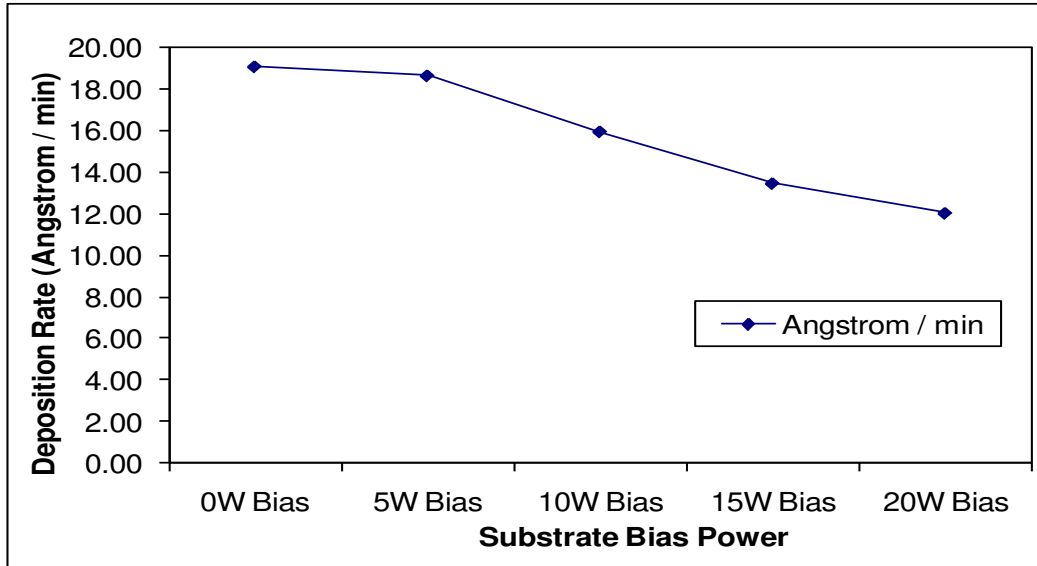


Figure 4-2 Deposition rate Vs Substrate bias

4.2 Stress measurements

Thin film stress measurements were made using Flexus instrument. Stress is calculated from the Stoney's formula, using the radius of curvature of the substrate measured before and after film deposition. Stress measurements were made from samples deposited at various processing conditions using 3" diameter wafer substrates. While it is presumed that the film's stress state is biaxial, measurements were made at two orthogonal directions, identified as "0" and "1", to understand the stress variation. These correspond to circumferential and radial directions, respectively, on the substrate holder for samples positioned as shown in Figure 3-12. Significant variations in the stress measurements were observed, as shown in Figure 4-5. The higher compressive stresses were observed for the samples deposited with 0W, 15W, and 20W bias and these were also the samples that exhibited delamination.



Figure 4-3 Cartoon of the delaminated film on Silicon

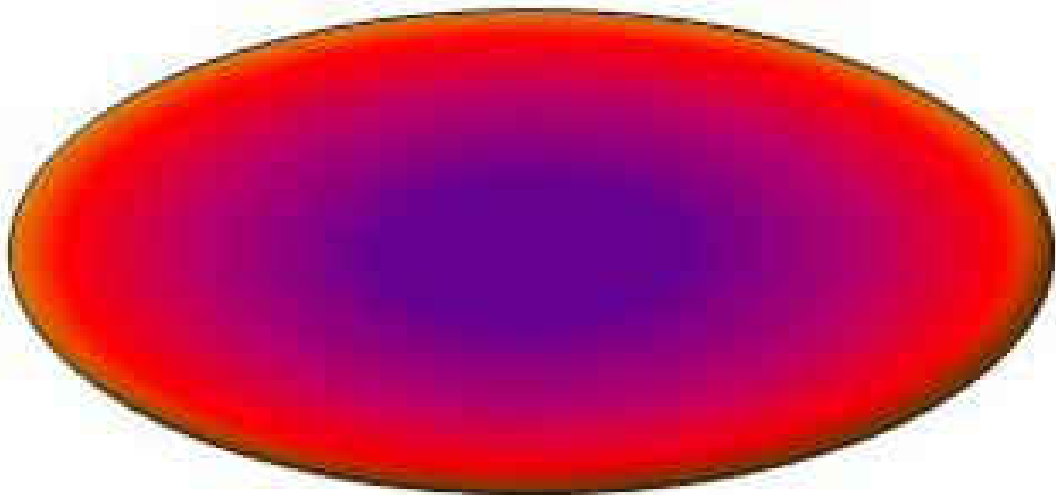


Figure 4-4 Cartoon of the non-delaminated film on Silicon

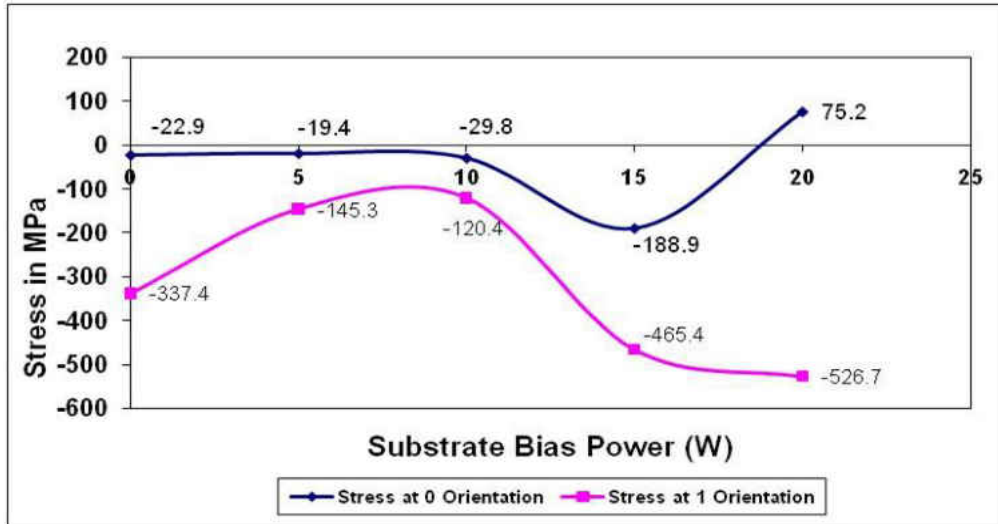


Figure 4-5 Stress measurements

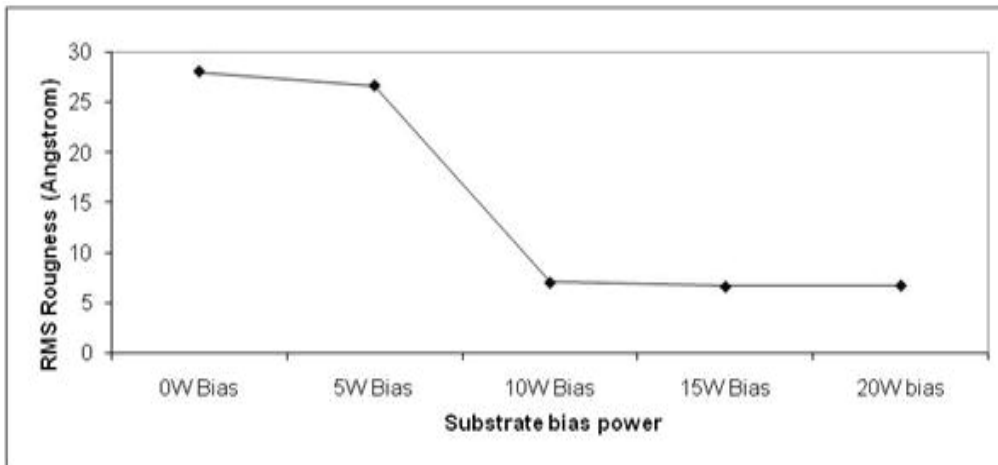


Figure 4-6 Surface Roughness Measurements

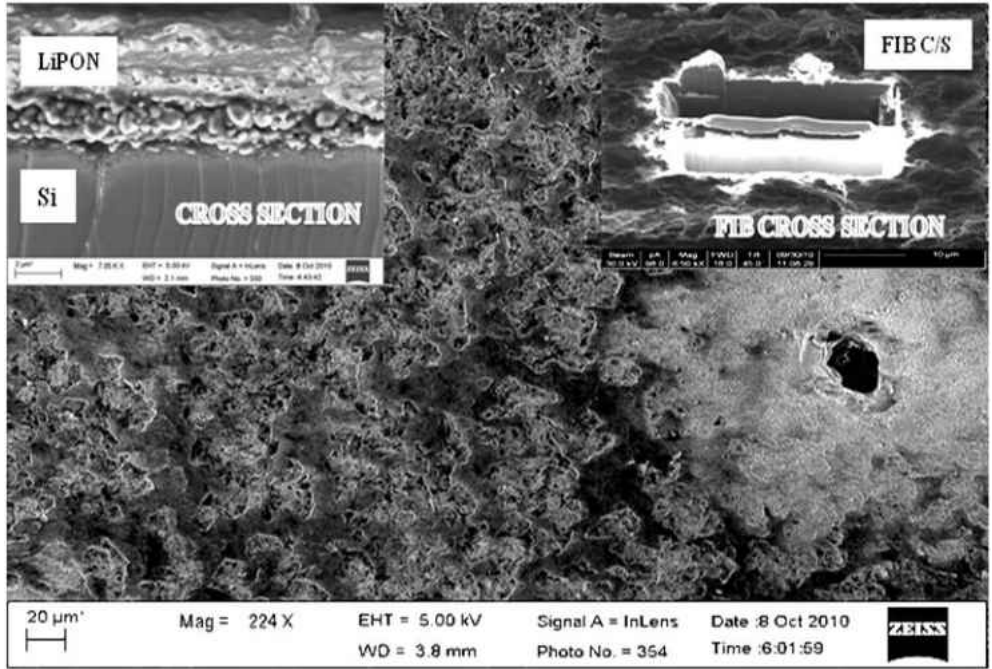


Figure 4-7 Delaminated film-SEM surface, cross section and FIB cross section

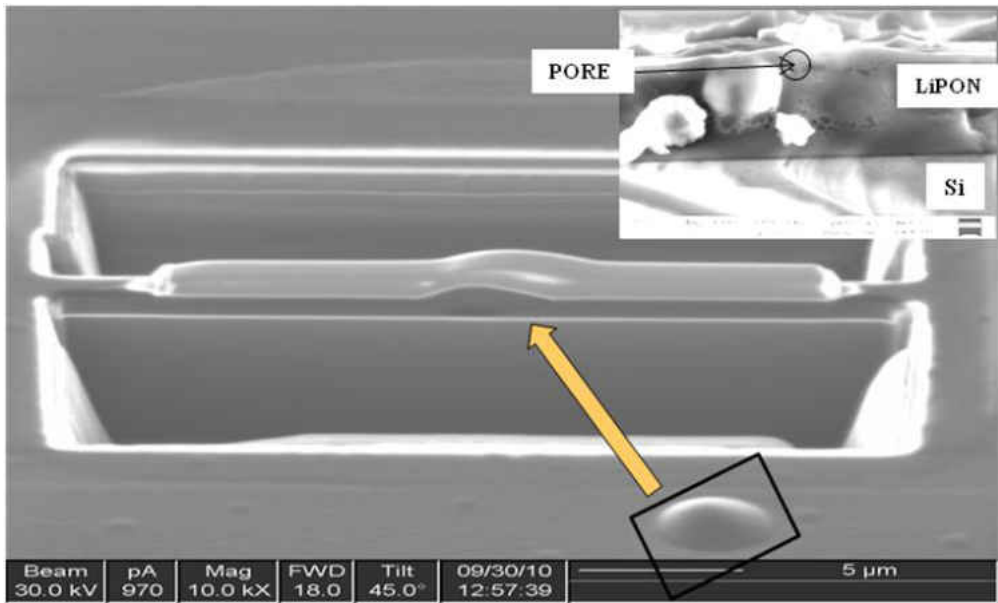


Figure 4-8 Non-delaminated film with crack initiating site-SEM surface, cross section and FIB cross section

4.3 Surface characterization

4.3.1 Surface roughness

Atomic force microscopy was used to analyze surface topography and surface roughness. This analysis showed that RMS roughness decreased with increasing substrate bias power.

4.3.2 Scanning electron microscopy

Surface and cross section film morphology was analyzed using scanning electron microscopy (SEM). Both the delaminated (Figure 4-7) and non-delaminated (Figure 4-8) regions of the sample deposited at 0W bias were examined. Figure 4-7 shows a plan view and cross-sectional image of film from the delaminated region. A high porosity is evident in the film. Figure 4-8 shows a blister formed and a focused ion beam (FIB) cross-sectional sample preparation of a second blister imaged by secondary electron emission in the FIB. The blisters are understood to be small regions of delamination from compressive stress. The inset of Figure 4-8 shows a non-blistered region and a reduced porosity compared to Figure 4-7 is evident.

4.4 Secondary ion mass spectroscopy

The secondary ion mass spectroscopy (SIMS) depth profiles of the porous, delaminated central region and the denser edge region of the 0W bias sample are shown in the Figures 4-9 and 4-10, respectively. Consistent with the SEM image shown in Figure 4-7 adventitious carbon contamination is present throughout the depth profile in the central region. The denser edge region shows a uniform film composition from the surface to a depth of 640 nm, after which a chemical interaction with the silicon wafer substrate is clearly evident from 640 nm to 860 nm. The samples deposited at all of the other bias powers had similar SIMS profiles to that shown in Figure 4-10. The thick substrate interaction layer requires that this aspect be examined further in future work.

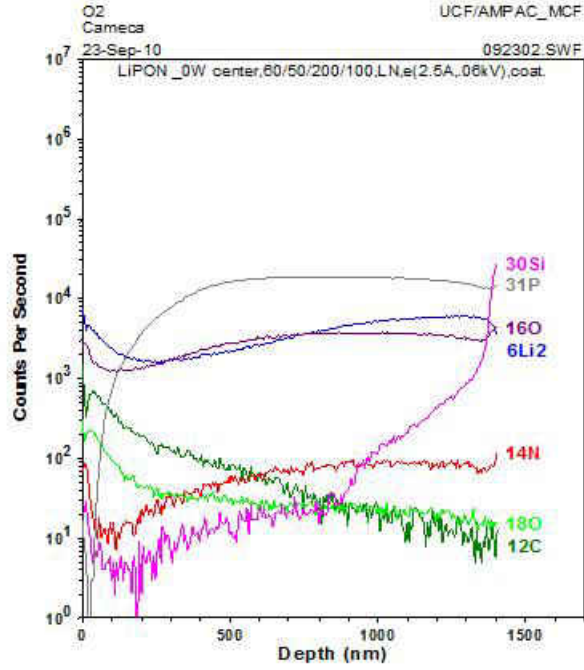


Figure 4-9 Delaminated region SIMS profile

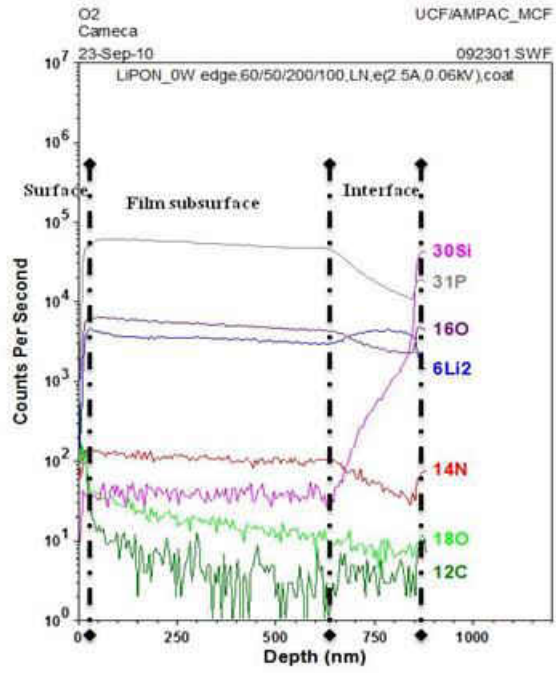


Figure 4-10 Non-delaminated region SIMS data

4.5 Summary

Stable LiPON thin films can be produced by intermediate levels of substrate biasing during RF deposition. The intermediate bias levels had minimal film compressive stress and did not suffer delamination. All the biased samples showed a stable elemental composition through the depth of the sample. . Bias effected the mechanical properties of the films (stress, adhesion). However, these LiPON films were deposited on to the silicon wafer and this generally gives rise to an additive error in the calculation of ionic conductivity measurement. SIMS experimental analysis shows lithium diffusion through the silicon substrate. thus Li/P atomic ratio measurement by ICP/OES does not represent the actual amount of lithium present in case of :LiPON deposition on the oxidized silicon wafer. The trends and variations in the ionic conductivity and the ICP/OES analysis needs to be revisited and understood deeply. Hence all the subsequent samples in the further research were deposited onto thermally grown silicon dioxide (>800 nm) on prime grade (100) silicon wafer.

CHAPTER 5 RESULTS

Table 5-1 Samples identified as A to O are processed at the conditions of substrate bias power, deposition temperature, process gas type, process gas pressure and flow as given. Additionally, the deposition rate for each sample, calculated from the LiPON electrolyte layer deposition time and thickness is also included.

| Series | Samples | Substrate bias (Watts) | Deposition temperature (°C) | Process gas | | | Deposition rate (Å/min) |
|---------------------------------|---------|------------------------|-----------------------------|-------------------|------------------|-------------|-------------------------|
| | | | | Ar/N ₂ | Pressure (mTorr) | Flow (sccm) | |
| Bias series | A | 0 | 24 | N ₂ | 5 | 20 | 18.00 |
| | B | 5 | 24 | N ₂ | 5 | 20 | 13.68 |
| | C | 10 | 24 | N ₂ | 5 | 20 | 11.86 |
| | D | 15 | 24 | N ₂ | 5 | 20 | 11.51 |
| | E | 20 | 24 | N ₂ | 5 | 20 | 9.46 |
| Temperature series-I | F | 10 | 200 | N ₂ | 5 | 20 | 10.97 |
| | G | 10 | 300 | N ₂ | 5 | 20 | 11.00 |
| | H | 10 | 400 | N ₂ | 5 | 20 | 10.57 |
| | I | 10 | 500 | N ₂ | 5 | 20 | 8.13 |
| Gas pressure series | J | 10 | 24 | N ₂ | 10 | 20 | 18.00 |
| | K | 10 | 24 | N ₂ | 15 | 20 | 13.68 |
| Temperature series-II | L | 0 | 300 | N ₂ | 5 | 20 | 17.38 |
| | M | 20 | 200 | N ₂ | 5 | 20 | 8.50 |
| | N | 20 | 300 | N ₂ | 5 | 20 | 7.36 |
| Li ₃ PO ₄ | O | 0 | 24 | Ar | 5 | 20 | 16.68 |

The deposition process conditions for the LiPON films of this study are given in Table 5-1. Samples A through E were deposited at a RF bias power levels ranging from none (0 W) to 20 W. Samples F through I were deposited at deposition temperatures ranging from 200°C to 500°C. Also included in Table 5-1 are samples deposited to explore combinations of bias and increased deposition temperature (samples J, K, and L), increased N₂ gas pressure during deposition (samples M and N), and a sample deposited with Ar instead of N₂ to provide a LiPO₄ film for comparison. The deposition rate measured for each set of deposition conditions is also given in Table 5-1, wherein can be seen that the deposition rate reduces as bias power or

deposition temperature are increased.

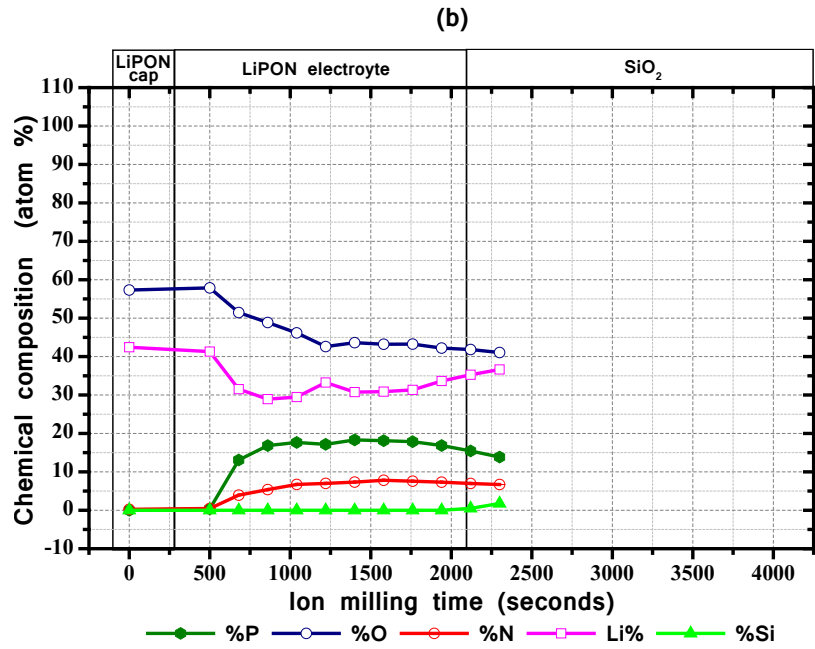
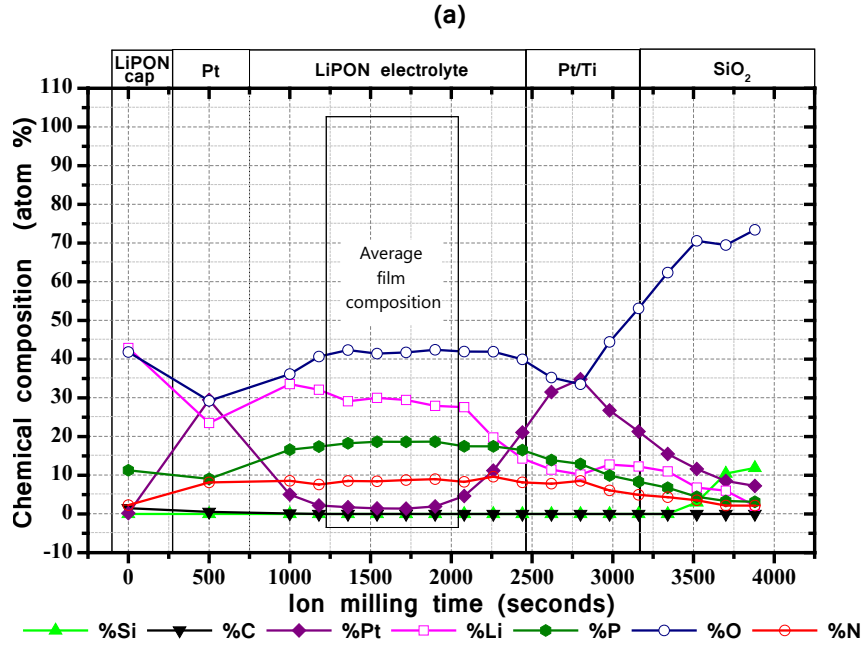
Table 5-2 Results of characterization of LiPON samples A through O. The film properties given are the ionic conductivity, the activation energy for the ionic conduction, the thin film intrinsic stress, (developed during deposition and cooling), the film density, the refractive index (n) at 999 nm, the extinction coefficient (k) at 246 nm, the penetration depth at 246 nm and the optical band gap energy.

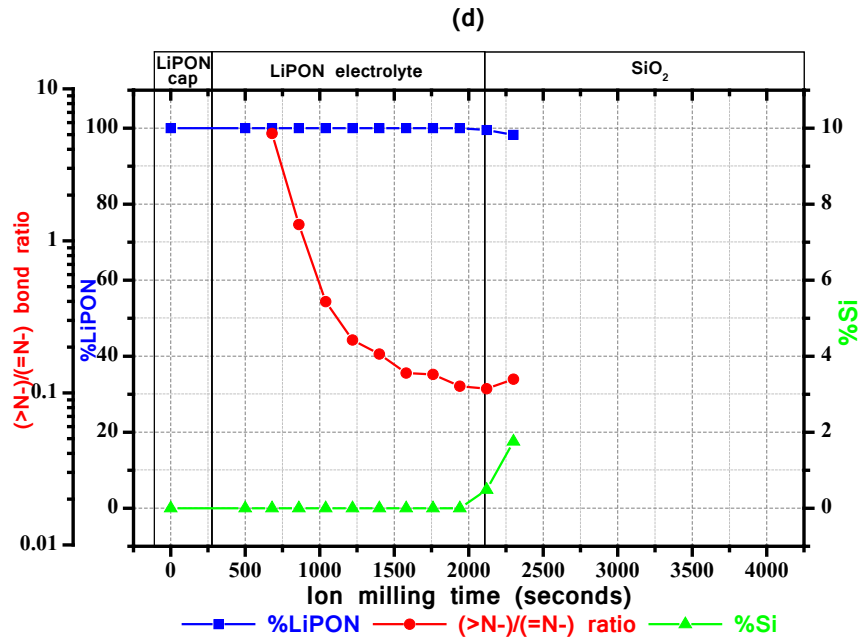
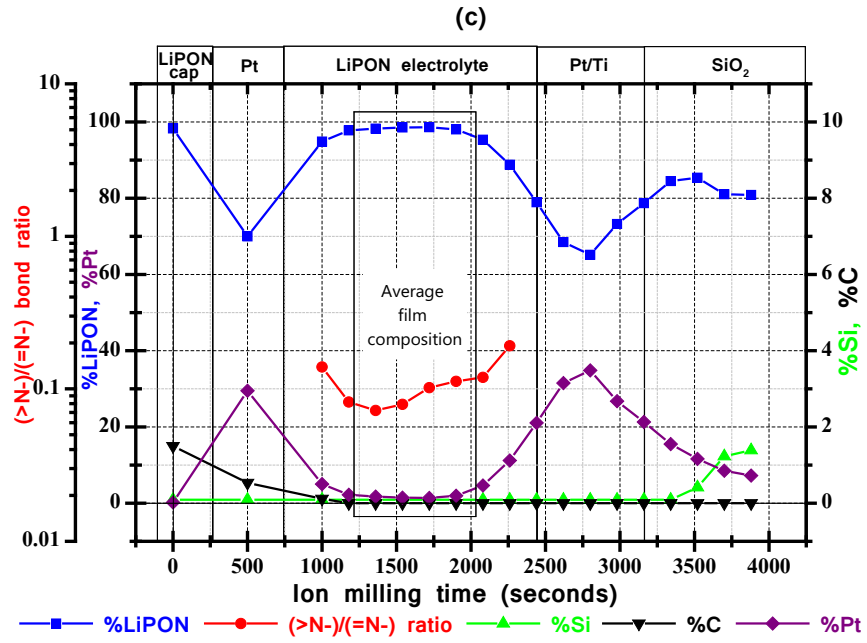
| Sample s | Ionic conductivity (S/cm) | Activation energy (eV) | Film stress (MPa) | Film density (g/cc) | n at 999 nm | κ at 246 nm | penetration depth, δ (nm) | E _g (eV) |
|----------|---------------------------|------------------------|-------------------|---------------------|-------------|-------------|---------------------------|---------------------|
| A | 7.81E-07 | 0.68 | -8.0 | 2.24 | 1.606 | 0.019 | 1041.81 | 3.95 |
| B | 9.55E-07 | 0.62 | -53.7 | 2.15 | 1.638 | 0.081 | 242.10 | 3.77 |
| C | 1.76E-06 | 0.54 | -159.4 | 2.13 | 1.658 | 0.166 | 118.06 | 3.52 |
| D | 1.48E-06 | N/A | -199.5 | 2.18 | 1.664 | 0.178 | 110.34 | 3.60 |
| E | 1.81E-06 | 0.53 | -204.9 | 2.21 | 1.697 | 0.071 | 277.03 | 2.70 |
| F | 3.05E-06 | 0.62 | 12.4 | 2.28 | 1.682 | 0.148 | 132.07 | 3.57 |
| G | 3.08E-06 | 0.57 | 144.8 | 2.43 | 1.669 | 0.118 | 166.55 | 3.62 |
| H | 3.37E-06 | 0.51 | 226.8 | 2.42 | 1.668 | 0.065 | 300.86 | 3.68 |
| I | 9.78E-06 | 0.49 | 265.8 | 2.52 | 1.697 | 0.041 | 483.60 | 3.75 |
| J | 3.52E-07 | 0.56 | -69.3 | 2.25 | N/A | N/A | N/A | N/A |
| K | 2.91E-07 | 0.62 | -124.9 | 2.11 | N/A | N/A | N/A | N/A |
| L | 9.01E-07 | 0.57 | 130.3 | N/A | 1.636 | 0.029 | 673.06 | 3.74 |
| M | 3.21E-06 | 0.55 | -58.1 | N/A | 1.685 | 0.166 | 117.70 | 3.50 |
| N | 3.70E-06 | 0.50 | 99.8 | N/A | 1.686 | 0.127 | 153.74 | 3.68 |
| O | 7.06E-07 | 0.59 | 28.1 | 2.44 | 1.585 | 0.033 | 627.76 | 3.82 |

Some of the properties of the films deposited for samples A through O are shown in Table 5-2. These include the ionic conductivity, the activation energy for ionic conduction, the film stress, the film density, and selected optical properties. Notably, Sample I, deposited at the highest temperature of 500°C has the highest ionic conductivity.

The XPS measurements of film composition includes compositional measurement after an initial Ar ion beam cleaning (and hence some erosion) of the sample surface and after several

additional Ar ion milling steps to provide composition measurements throughout the depth of the film (depth profiling).





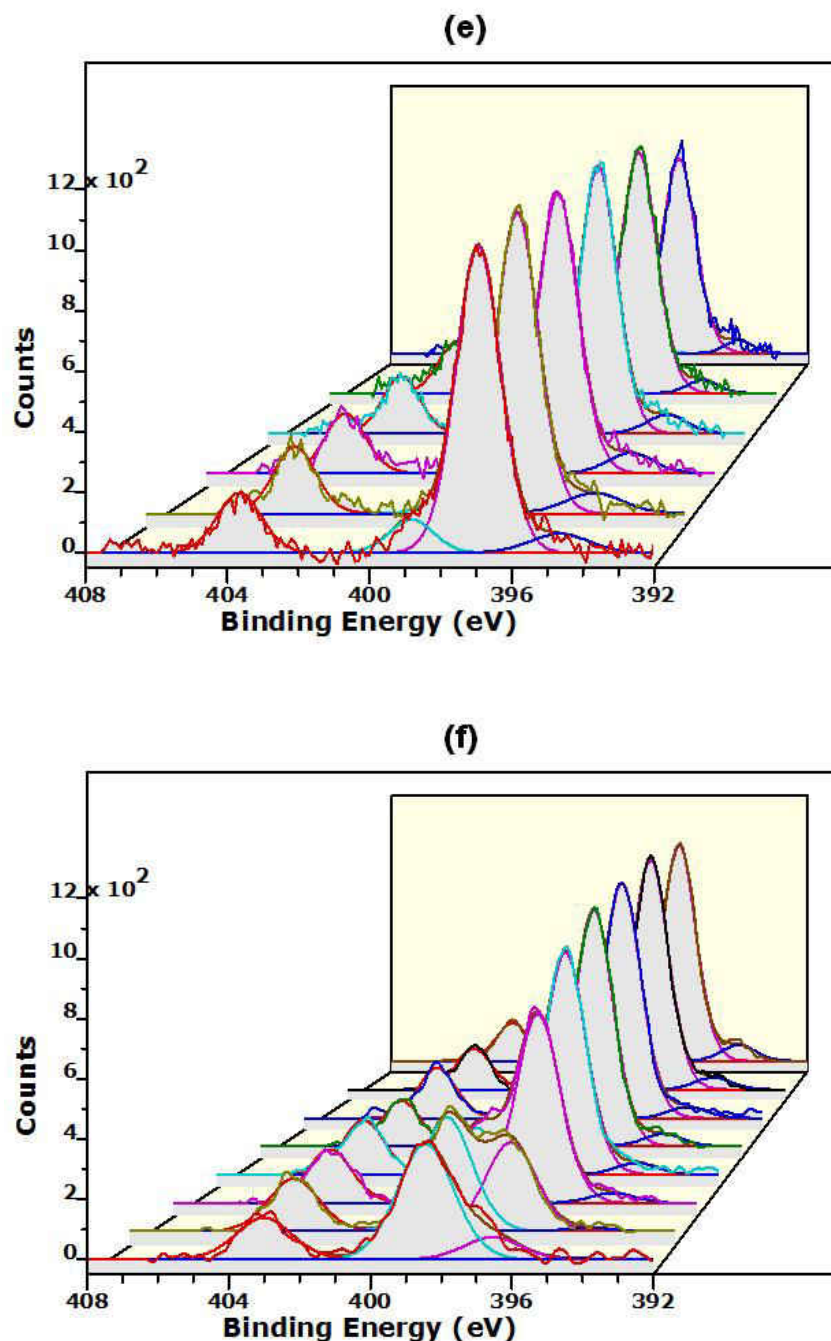
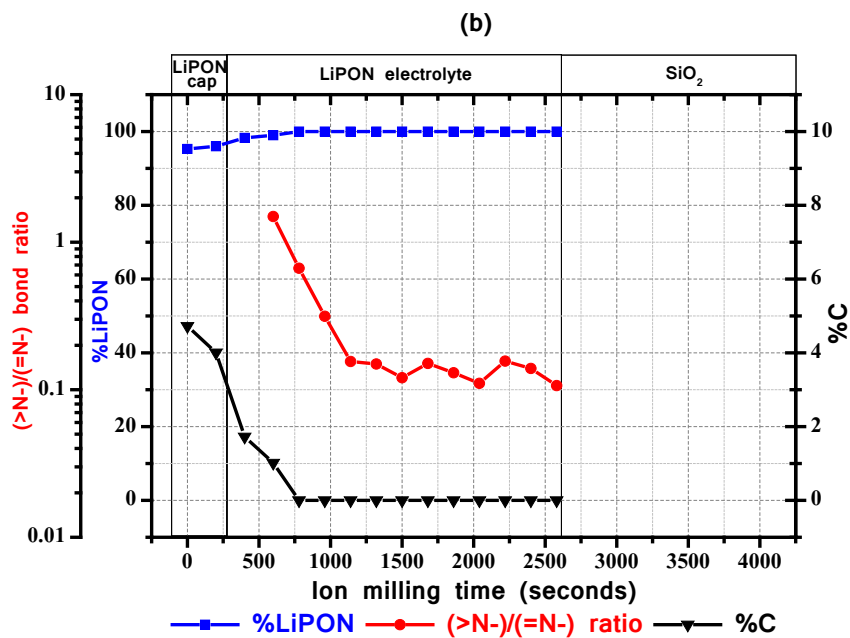
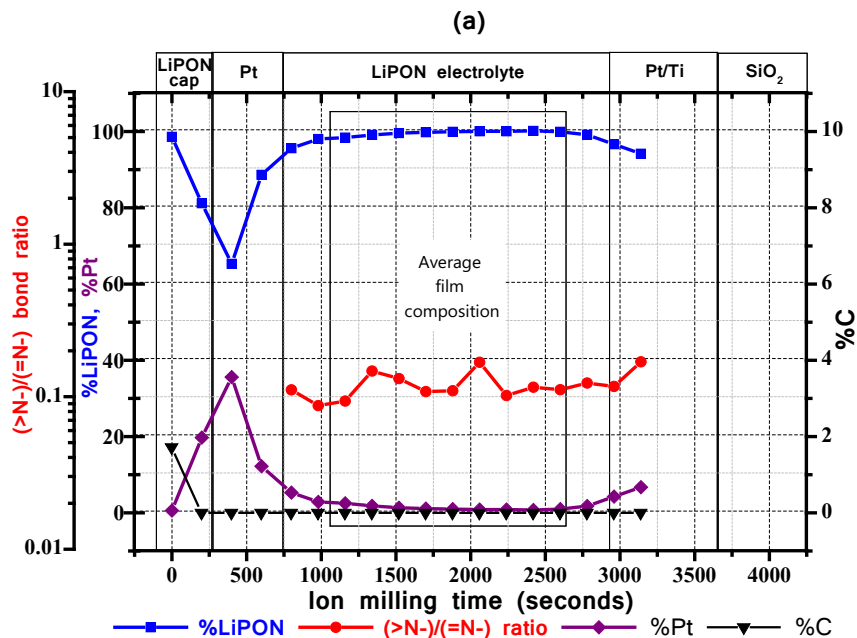


Figure 5-1. Results of the XPS depth profiling of sample G. Inset (a) shows the variation of composition as atomic percent as a function of ion milling time in an area with Pt electrodes. Inset (b) shows the equivalent depth profile of an adjacent area without Pt electrodes. Inset (c) shows %LiPON, %Pt, %C, %Si and the (>N-)/(=N-) bond ratio as a function of ion milling time for an area with Pt electrodes. Inset (d) shows the %LiPON, %Si and the (>N-)/(=N-) bond ratio for an adjacent area without Pt electrodes. Inset (e) shows the high resolution N1s scans from the area with Pt electrodes overlaid at a sequence of ion milling times to illustrate the relative

consistency of the N bonding with depth. Inset (f) shows the high resolution N1s scans from an adjacent area without Pt electrodes to illustrate the variation of N bonding in the upper portion of the LiPON layer.



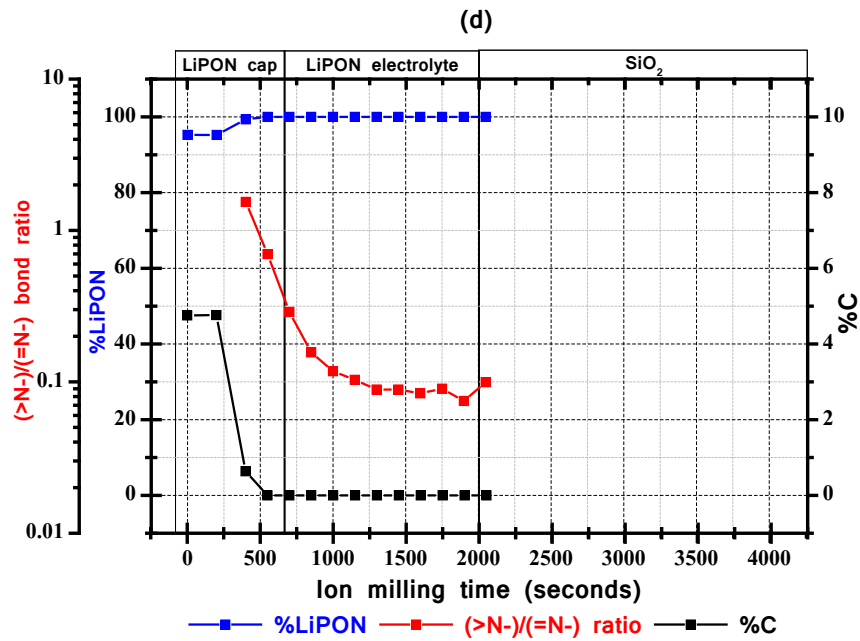
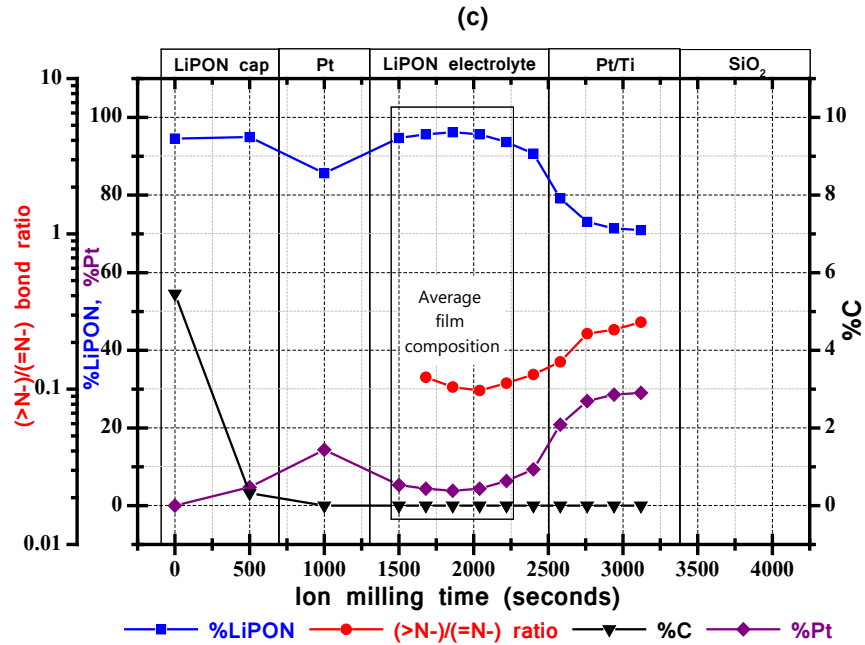
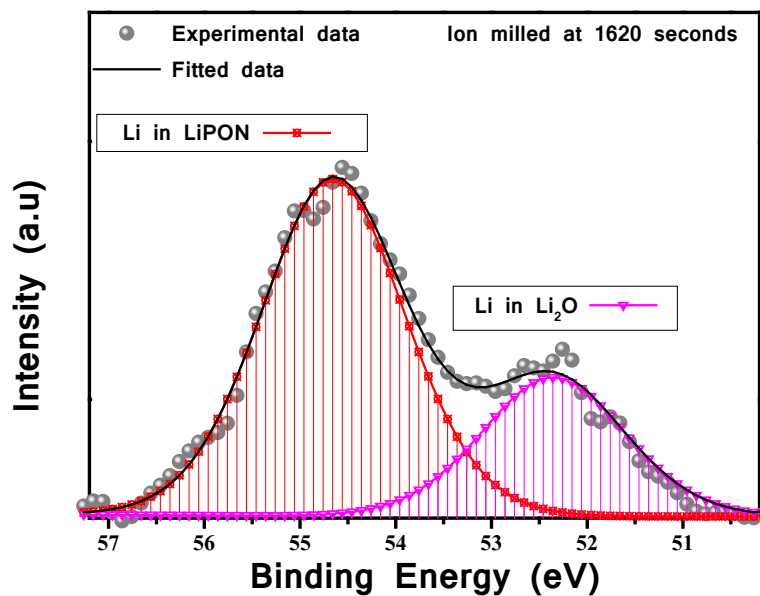
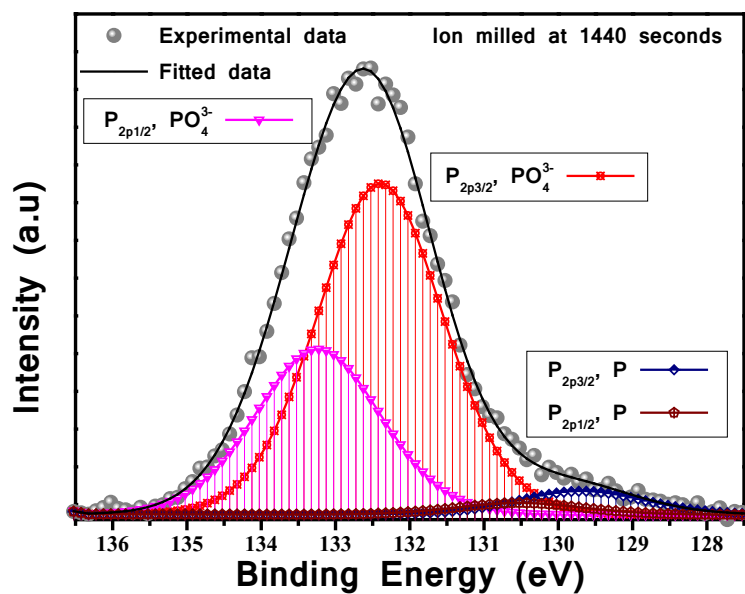


Figure 5-2. Results of XPS depth profiling of samples B and F. Insets (a) and (b) show the variation in composition and bonding for sample B in an area with and without Pt electrodes, respectively. Insets (c) and (d) show the same comparative data for sample F.

(a)



(b)



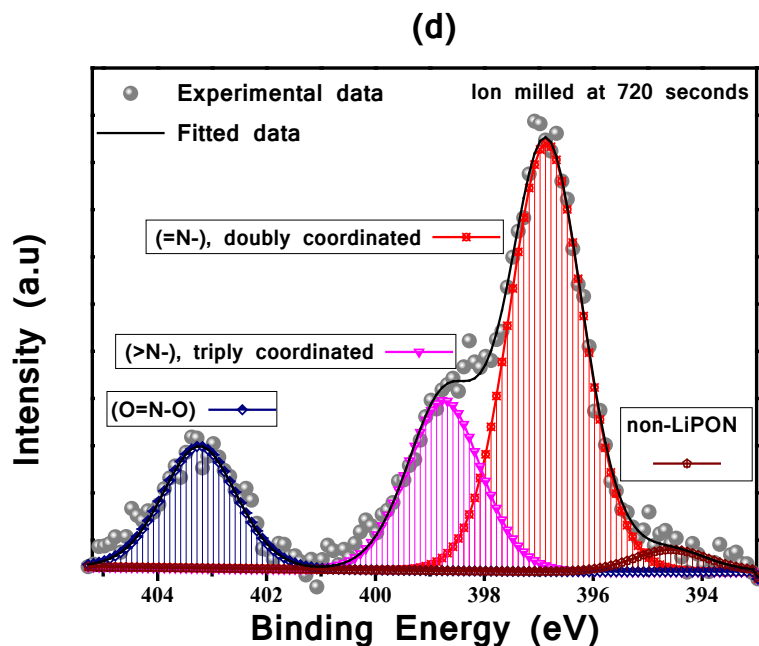
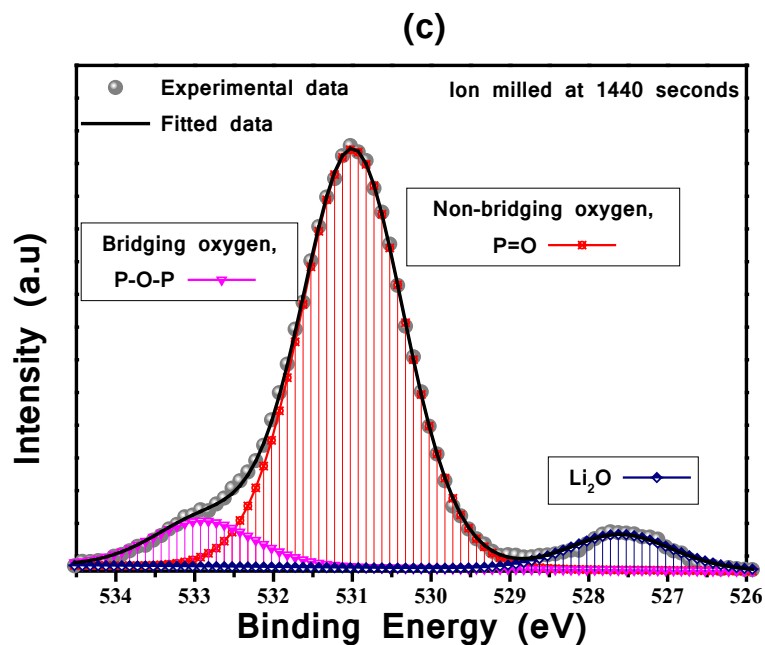


Figure 5-3. Examples of the deconvolution of the high resolution XPS spectra from sample G of Li1s, O1s, N1s and P2p scans are given by insets (a), (b), (c) and (d), respectively. The attribution of the peaks to different bonds is given in the text.

The later step which is a depth profiling was done on both the Pt/LiPON/Pt device area and on the blanket film region without Pt electrodes immediately adjacent to the Pt/LiPON/Pt

device. The compositional profiles of the tested LiPON (i.e., sample G) on the device region and on the adjacent region are shown in Figures 5-1a) and 5-1b), respectively. For clarity, the regions corresponding to each layer present in the profile are indicated in the Figures. Significant differences between the LiPON film composition in the Pt/LiPON/Pt devices and that of the adjacent blanket film were observed for all samples.

In spite of the presence of the LiPON cap layer, the composition on the near-surface region of the film areas without the Pt electrodes appears to be significantly different than that of the majority of the film. The composition of the LiPON cap layer and the upper portions of the LiPON electrolyte layer in the regions of each sample without Pt electrodes have high lithium and oxygen concentration and correspondingly low nitrogen and phosphorus content. This oxidized surface occurred in spite of the sample storage in high purity Ar (nominally 99.999%) with limited ambient air exposure during ionic conductivity measurements (less than 12 hours in all cases). The type of nitrogen bonding present also showed a difference with depth in the regions without Pt electrodes, with a higher ratio of triply coordinated nitrogen to doubly coordinated nitrogen ($>N^-$)/($=N^-$) in the near-surface region than in the rest of the film layer. For sample G, this ratio is shown for the device and adjacent areas on an additional logarithmically scaled axis in Figures 5-1c) and 5-1d), respectively. For the adjacent area without the Pt electrodes the ratio drops from a value greater than 5.0 just below the surface of the LiPON electrolyte layer (after 680 seconds of Ar ion etching) to less than 0.2 in the bulk of the LiPON electrolyte layer (after 1400 seconds of Ar ion etching). For the Pt/LiPON/Pt device region the result of the XPS depth profiling is very different, as shown in Figure 5-1c). In this case, the ratio of triply coordinated nitrogen to doubly coordinated nitrogen stays in the range of 0.19 to 0.07 in the electrolyte layer. This indicates that degradation of the surface of the LiPON

electrolyte layer occurred in areas not protected by Pt electrodes, in spite of the presence of a LiPON encapsulant layer.

Table 5-3 Compositional measurements of Samples A through O. The XPS measured elemental compositions in atomic percentages of Li, P, O, and N together with the derived stoichiometry of LiPON films are given along with the Li/P atomic ratios calculated from XPS and from ICP/OES measurements.

| Sample s | XPS analysis | | | | Li/P atomic ratio | | |
|-------------|--------------|------|------|------|--|------|---------|
| | %Li | %P | %O | %N | Stoichiometry | XPS | ICP/OES |
| A | 32.7 | 16.1 | 47.1 | 4.1 | Li _{2.04} P O _{2.93} N _{0.26} | 2.04 | 2.98 |
| B | 28.1 | 15.6 | 51.4 | 4.9 | Li _{1.81} P O _{3.30} N _{0.31} | 1.81 | 3.14 |
| C | 33.6 | 15.0 | 47.3 | 4.1 | Li _{2.24} P O _{3.15} N _{0.28} | 2.24 | 3.60 |
| D | 35.8 | 14.0 | 46.3 | 3.9 | Li _{2.56} P O _{3.31} N _{0.28} | 2.56 | 4.17 |
| E | 32.6 | 14.3 | 49.4 | 3.7 | Li _{2.27} P O _{3.45} N _{0.26} | 2.27 | 4.54 |
| F | 31.4 | 18.3 | 42.3 | 8.0 | Li _{1.72} P O _{2.32} N _{0.44} | 1.72 | 3.32 |
| G | 29.4 | 19.2 | 42.8 | 8.7 | Li _{1.53} P O _{2.23} N _{0.45} | 1.53 | 2.76 |
| H | N/A | N/A | N/A | N/A | N/A | N/A | 2.41 |
| I | 27.1 | 19.6 | 43.0 | 10.3 | Li _{1.38} P O _{2.20} N _{0.52} | 1.38 | 2.38 |
| J | N/A | N/A | N/A | N/A | N/A | N/A | 4.09 |
| K | N/A | N/A | N/A | N/A | N/A | N/A | 4.44 |
| L | 29.4 | 16.4 | 48.2 | 6.0 | Li _{1.79} P O _{2.95} N _{0.37} | 1.79 | N/A |
| M | 26.4 | 16.3 | 50.5 | 6.8 | Li _{1.61} P O _{3.09} N _{0.41} | 1.61 | N/A |
| N | 24.4 | 18.2 | 48.9 | 8.5 | Li _{1.34} P O _{2.68} N _{0.47} | 1.34 | N/A |
| O | N/A | N/A | N/A | N/A | N/A | N/A | N/A |

There have been prior XPS studies of bonding in LiPON films by various authors.[6,12,24,27,31,33,35,92] However, depth profiling was not used in their studies and hence the surface areas sampled were without the protection of Pt electrodes. These prior studies sampled areas adjacent to the devices or areas on separate wafers. In the depth profiling study presented in this paper, it is clear that the prior studies of the near surface regions without depth profiling are subject to varying extents of surface degradation. The ratio of triply-coordinated to doubly-coordinated nitrogen ($>N^-$)/($=N^-$) reported in these prior studies of sputter deposited

LiPON films is also variable, from a low of 0.15 to a high of 3.33, and are worthy of review for their variability. Chiu et al., found the ratios between 2.2 and 1.02 when varying substrate bias power.[35] Fleutot et al., obtained ratios between 1.2 and 0.5 while varying the argon/nitrogen gas mixture.[33] Hu et al., varied the sputter deposition power and found ratios between 0.63 and 0.16.[27] Roh et al., also varied the deposition power and found relatively consistent ratios between 0.155 and 0.150.[12] Park et al., varied the nitrogen sputtering gas pressure and found ratios of 0.62 and 0.66.[24] Pichonat et al., reported a single value of 2.13 for the ratio.[31] Kim et al., deposited LiPON by plasma assisted directed vapor deposition instead of sputtering and found ratios between 1.65 and 0.72.[30] Wang et al., melt quenched and synthesized bulk LiPON and found the ratio to be 3.33.[6] Many of these prior works considered the triply coordinated nitrogen significant to the ionic conductivity, however, the details of the sample handling (i.e., exposure to air) and the extent to which any ion beam cleaning of the surface was performed prior to acquisition of the XPS spectra are absent.

However, in another work of Wang et al.[6] it was inferred that the presence of triply coordinated nitrogen is attributed only to a surface phenomenon. In the solid state nuclear magnetic resonance analysis of ion beam assisted deposition of LiPON films, the presence of triply coordinated nitrogen was largely absent.[21] This means that the bulk characterization of LiPON films does not show the presence of triply coordinated nitrogen. In the simulation studies of Holzwarth models,[61] in the extreme case of α - P_3N_5 where all the nitrogen bonds are triply coordinated, there are no lithium ions present. The two possible forms of LiP_4O_7 , that were analyzed, had only a small concentration of mobile lithium ions and some triply coordinated nitrogen sites. For the crystalline forms of LiPON films, the triply coordinated nitrogen bonds could be present only at low lithium concentrations. Hence, for typical LiPON films, in order to

sustain lithium concentrations for lithium ion conduction, only a small number of triply coordinated nitrogen sites are possible.

Table 5-4 Lithium and nitrogen bonding characteristics of samples A through N. A comparison of the amount of the two types of lithium bonds observed in the XPS characterization (Li bonding in LiPON and lithium bonded to just oxygen (Li₂O) as in non-LiPON) and the amount of the three types of LiPON nitrogen bonds (O=N-O), (>N-), (=N-), and the (>N-)/(=N-) bonding ratio. Also given is the amount of the unidentified nitrogen bond type, classified as non-LiPON.

| Samples | %Li | | %N | | | | |
|---------|-----------------|-----------------------------------|--------|-------|-------------|------|--|
| | %LiPON | (Li ₂ O) %non-LiPON | %LiPON | | | | (Unidentified nitrogen), %non-LiPON |
| | Li ⁺ | (O-N=O) | (=N-) | (>N-) | (>N-)/(=N-) | | |
| A | 24.7 | 8.1 | 0.9 | 2.5 | 0.4 | 0.15 | 0.4 |
| B | 23.5 | 4.7 | 0.9 | 3.1 | 0.4 | 0.12 | 0.5 |
| C | 22.8 | 10.7 | 0.7 | 2.6 | 0.2 | 0.06 | 0.7 |
| D | 24.2 | 11.5 | 0.7 | 2.2 | 0.2 | 0.11 | 0.7 |
| E | 24.7 | 7.8 | 0.8 | 2.1 | 0.3 | 0.15 | 0.6 |
| F | 28.3 | 3.1 | 1.4 | 5.5 | 0.6 | 0.10 | 0.6 |
| G | 28.0 | 1.4 | 1.2 | 6.4 | 0.6 | 0.09 | 0.4 |
| I | 24.3 | 2.8 | 1.2 | 8.1 | 0.5 | 0.06 | 0.4 |
| L | 25.4 | 4.0 | 0.9 | 4.3 | 0.4 | 0.10 | 0.3 |
| M | 26.2 | 0.2 | 1.0 | 4.9 | 0.3 | 0.07 | 0.5 |
| N | 22.5 | 1.8 | 1.3 | 5.8 | 0.6 | 0.11 | 0.8 |

The range of ratios observed in prior works, having potential (but unknown) extents of surface degradation, are consistent with those that we have found profiling to different depths in areas not protected by Pt electrodes, as shown in example of Figure 5-1d). However, the depth profiling of Pt encapsulated areas, in this study, has shown that these values are not representative of the device regions (as shown in Figure 5-1c). These differences in the triply coordinated and doubly coordinated nitrogen in the device and non-device areas is further evident in the XPS spectra of the relevant energy range shown in Figures 5-1e) and 5-1f) respectively. Additional examples comparing the Pt protected and non-protected areas (as in

Figure 5-1c and 5-1d) are shown in Figure 5-2, from samples B and J. These also show unrepresentatively high (>N-)/(=N-) ratios in the near surface regions of the areas not protected by Pt electrodes. From this, it can be concluded that ex-situ XPS compositional studies without depth profiling of the device regions are not an accurate representation of the composition and bonding present in the LiPON electrolyte layer of the device regions. Accordingly, the XPS results reported in Tables 5-3, 5-4, and 5-5 of this work are derived solely from depth profiling of the sample areas that were protected by Pt electrodes, where ionic conductivity was measured.

Representative deconvolved XPS spectra of the Li1s, P2p, O1s, and N1s peak regions are given in Figure 5-3 a), b), c), and d), respectively. The Li1s spectrum shown in Figure 5-3a) has two peaks at 54.7 eV and at 52.4 eV. The peak at 54.7 eV can be assigned to Li bonding in LiPON and the one at 52.4 eV can be assigned to Li bonding to oxygen (Li-O) as in Li_2O , due to the difference in the binding energy between the two peaks is ~ 2.3 eV.[76,93,88,94] The phosphorus P2p spectrum of Figure 5-3b) has four peaks representing both the $2p_{1/2}$ and $2p_{3/2}$ contributions to the phosphorus bonding in PO_4^{3-} and to the reduced phosphorus (zero valence) bonding. For the PO_4^{3-} environment, the $\text{P}2p_{3/2}$ peak was observed at 132.4 eV[30,33] and the $\text{P}2p_{1/2}$ contribution was 0.84eV higher, at 133.24eV. For the reduced phosphorus environment, the $\text{P}2p_{3/2}$ peak was observed at 129.7 eV[95,96] and the $\text{P}2p_{1/2}$ contribution was observed at 130.54eV. The O1s spectrum of Figure 5-3c) clearly shows three peaks upon deconvolution; bridging oxygen P-O-P (BO) at 532.9 eV, non-bridging oxygen P=O (NBO) at 531 eV, and a weaker peak of Li_2O bonding at 527.7 eV. The BO and NBO peak identifications are consistent with prior reports of alkali bulk phosphate glasses[47] and LiPON films[94]. The Li_2O bonding peak at 527.7 eV in the O1s spectrum is also described in the literature[76,93,88]. The N1s spectrum of Figure 6d) was deconvolved into four peaks; a (O-N=O) bonding peak at 403.2

eV[6], a (>N-), triply coordinated nitrogen bonding peak at 398.7 eV[51], a (=N-), doubly coordinated nitrogen peak at 396.9 eV[51], and a weaker unidentified peak (N1) at 394.6 eV that has also been observed by others[6].

Table 5-5 Phosphorous and oxygen bonding characteristics of samples A through N. The amounts of the two types of phosphorus bonds (phosphate PO_4^{3-} and the reduced phosphorus) and the amount of the oxygen bonded in phosphate PO_4^{3-} (bridging oxygen (-O-) and non-bridging oxygen (P=O)) are given. Also given is the amount of oxygen bonded with lithium (Li_2O , non-LiPON).

| Samples | %P | | %O | | |
|---------|--|------------|------------------------|-----------------------------|------------|
| | %LiPON | %non-LiPON | %LiPON | | %non-LiPON |
| | PO_4^{3-} , Phosphate network | | BO, bridging oxygen | NBO, non-bridging oxygen | |
| A | 15.5 | 0.5 | 4.5 | 38.7 | 3.9 |
| B | 14.9 | 0.6 | 3.8 | 44.7 | 2.9 |
| C | 14.4 | 0.6 | 2.6 | 39.0 | 5.8 |
| D | 13.5 | 0.5 | 3.0 | 38.3 | 4.9 |
| E | 13.8 | 0.5 | 3.2 | 41.9 | 4.3 |
| F | 16.8 | 1.5 | 2.0 | 38.0 | 2.4 |
| G | 17.7 | 1.5 | 2.4 | 38.9 | 1.5 |
| I | 16.4 | 3.2 | 1.7 | 38.0 | 3.3 |
| L | 48.2 | 6.0 | 3.5 | 41.9 | 2.8 |
| M | 50.50 | 6.76 | 2.3 | 46.8 | 1.4 |
| N | 48.92 | 8.50 | 3.2 | 41.9 | 3.8 |

Table 5-3 includes the composition, in atomic percent, of the LiPON films, of samples A through L, as determined by XPS. Additionally, the Li/P atomic ratio as determined by ICP/OES is included in the table. A Li/P atomic ratio calculated from the XPS data is approximately 40% lower than that determined by ICP/OES, presumably due to the preferential sputtering of Li during profiling[69]. The XPS values given in Table 5-3 are an average of measurements from within the bulk of the LiPON film in the Pt/LiPON/Pt device areas, which is most representative of the material whose ionic conductivity was measured. As an example, the values in the cross-

hatched region in Figure 5-1a) were averaged to provide the compositional information for sample G shown in Table 5-3.

Table 5-6 Molar volume calculations for samples A through I from the atomic weights of Li, P, O, and N in LiPON and the measured film density.

| Samples | Li (g/mole) | P (g/mole) | O (g/mole) | N (g/mole) | Total (g/mole) | Film density (g/cc) | mole/cc | cc/mole |
|---------|----------------|---------------|---------------|---------------|-------------------|------------------------|---------|---------|
| A | 2.29 | 4.98 | 7.53 | 0.58 | 15.38 | 2.24 | 0.15 | 6.87 |
| B | 1.97 | 4.82 | 8.22 | 0.69 | 15.70 | 2.15 | 0.14 | 7.30 |
| C | 2.35 | 4.65 | 7.57 | 0.58 | 15.15 | 2.13 | 0.14 | 7.11 |
| D | 2.50 | 4.34 | 7.41 | 0.55 | 14.80 | 2.18 | 0.15 | 6.79 |
| E | 2.28 | 4.44 | 7.91 | 0.52 | 15.15 | 2.21 | 0.15 | 6.85 |
| F | 2.20 | 5.65 | 6.77 | 1.12 | 15.75 | 2.28 | 0.14 | 6.91 |
| G | 2.06 | 5.95 | 6.84 | 1.21 | 16.06 | 2.43 | 0.15 | 6.61 |
| I | 1.90 | 6.07 | 6.88 | 1.44 | 16.29 | 2.52 | 0.15 | 6.47 |

Tables 5-4 and 5-5 present the results of the deconvolution of the XPS high resolution scans of the Li 1s, P 2p, O 1s, and N 1s peaks. The lithium 1s peak was further analyzed to deconvolute the contribution of Li bonded in LiPON and Li-oxygen bonding (Li_2O) and these fractions shown in Table 5-4 as percentages of the overall film composition (Li+P+O+N). Similarly, the nitrogen 1s peak was deconvoluted into four peaks. Three of these peaks are associated with LiPON; nitrogen bonded to oxygen ($\text{O}=\text{N}-\text{O}$), triply coordinated nitrogen bonded to phosphates, ($>\text{N}-$), and doubly coordinated nitrogen bond to phosphates ($=\text{N}-$). There is also an unidentified fourth peak. The fractions of each form of nitrogen bonding and the ($>\text{N}-$)/($=\text{N}-$) ratio are also given in Table 5-4, in atomic percent of the overall film composition. Table 5-5 provides the similar deconvolution results of the phosphorus into PO_4^{3-} and reduced phosphorus and the similar deconvolution of the oxygen into bridging and non-bridging oxygen bonding.

The density and composition data in Tables 5-2 and 5-3 is used to calculate the molar volume for each sample, and this is presented in Table 5-6.

CHAPTER 6 DISCUSSIONS

6.1 Substrate bias power

LiPON film samples A to E were processed varying substrate bias power while using common conditions of a room temperature deposition and 5mTorr of nitrogen process gas. While initially explored to improve adhesion, the use of substrate bias had a significant effect on the LiPON film properties as well as the deposition process itself. As shown in Figure 6-1a), the ionic conductivity increased with bias power. The increase of ionic conductivity for the samples deposited at room temperature was from less than 1.0×10^{-6} S/cm for 0W and 5W of bias, reaching values of $\sim 1.8 \times 10^{-6}$ S/cm and 1.9×10^{-6} S/cm for 10W and 20W of bias respectively. For the samples deposited at 300°C, the increase was from less than 1.0×10^{-6} S/cm for 0W bias to $\sim 3.7 \times 10^{-6}$ S/cm for 20 W bias. This increase in ionic conductivity correlates with increases in the Li/P ratio measured by ICP OES shown in Table 5-3 and by the Li (LiPON bonding) to P (LiPON bonding) ratio measured by XPS shown in Tables 5-4 and 5-5. As the ionic conductivity of LiPON can be considered the product of the Li ion density times the Li ion mobility[12], a higher Li ion concentration can be expected to correlate to higher ionic conductivity.

The applied bias caused other changes in the films. It did provide homogeneous adhesion of the film to the substrate, equivalent at the inner diameter and outer diameter. However, it also caused significant resputtering of the film material from the substrate surface. At the highest bias power (20W) examined, approximately half of the LiPON deposited was removed during deposition due to this resputtering, reducing the net film deposition rate. While the deposition rate decreased drastically with bias power, the change in the film density of the deposited film was relatively unchanged as shown in Table 5-2. On the other hand, the Li/P atomic ratio as

measured by ICP/OES increased with bias power. The change in the phosphorus content that is possible in stable amorphous phosphate networks (PO_3 to PO_4) is relatively small (less than 25 atomic percent). Hence the increase in the ICP/OES Li/P ratio from 2.98 to 4.54 (a ~50% increase) should be interpreted as an increase in the lithium concentration in the film, and this is weakly supported by the XPS measurements of Li concentration. Note that a Li/P atomic ratio of 3.0 is expected for an ideal PO_4 network (Li_3PO_4) while an atomic ratio of 1.0 is expected for an ideal PO_3 network (LiPO_3).[16] The increase in the lithium concentration with increasing resputtering of the depositing film is expected due to the lower sputtering yield of lithium compared to phosphorus, estimated at 37.8% of the phosphorus yield.[69] These trends indicate the significant role that substrate bias has in modifying the structure and composition of LiPON thin films.

The activation energy for lithium ion conduction generally decreases with substrate bias, as shown in Figure 6-1b). It is possible that the slightly lower density amorphous network obtained at intermediate bias power (10W) allowed greater opportunities for lithium ion mobility and hence higher conductivity and lower activation energy. Note that the conductivity was similarly high at 10W and 20W of bias while the Li/P ratio observed by ICP/OES increased consistently with increasing bias, suggesting that the mobility of lithium ions may also be a factor in these films.

The increased N_2 ion bombardment and resputtering due to the increasing substrate bias also caused a change in the stress state of the film. A mild compressive stress of -8 MPa was observed for the sample deposited without substrate bias (0W), increased to a more compressive value of -205 MPa for the sample deposited at 20W substrate bias, as given in Table 5-2. The LiPON films processed at the intermediate substrate bias condition of 10W exhibited good

adhesion, modest stress, and high ionic conductivity and this was taken as the optimized bias condition for further experiments with deposition temperature and variation in the nitrogen gas pressure.

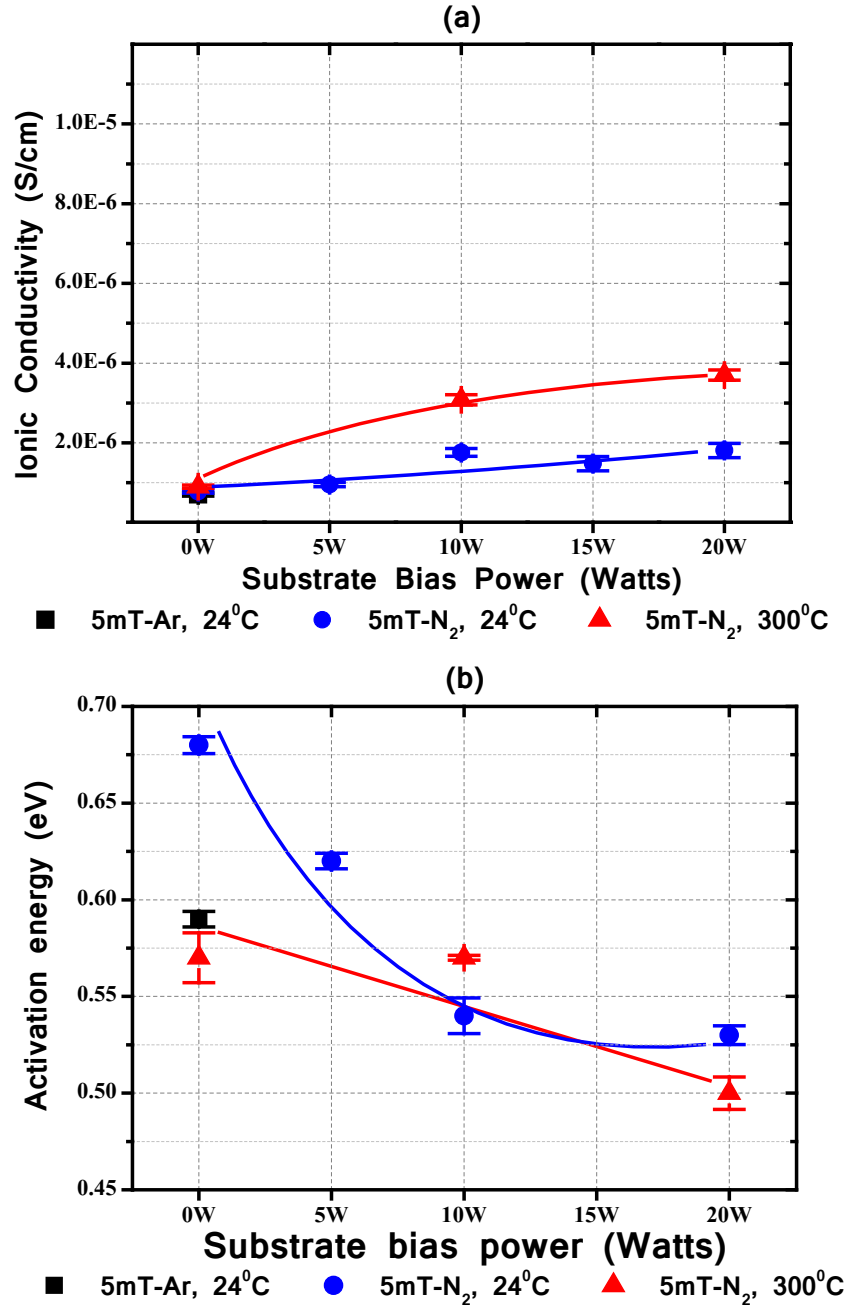


Figure 6-1 Inset (a) shows the ionic conductivity and inset (b) the activation energy of ionic conduction for LiPON films as a function of substrate bias power. Please note that the curved lines are shown to guide the eye.

6.2 Pressure effects at 10W substrate bias condition

Higher N₂ gas pressures of 10 mTorr and 15 mTorr were explored at the 10W substrate bias condition and room temperature deposition to compare to the films deposited at 5 mTorr of N₂. The deposition rate decreased with increasing process gas pressure, as given in Table 5-1. The Li/P atomic ratio, as measured by ICP/OES, increased with gas pressure. The decrease in the ionic conductivity at higher pressures was accompanied by an increase in the activation energy for ionic conduction and a slight increase in compressive stress. No significant advantage to higher deposition pressures was observed.

6.3 Deposition temperature effects at 10W bias condition

The significant effect of the energetic bombardment associated with substrate bias on the structure and properties of LiPON films motivated a study of increasing energy at the atomic scale by increasing temperature during deposition. Specifically, higher deposition temperature is expected to enhance the mobility of adatoms on the surface of the depositing film and result in a structure having a lower defect density that is closer to the metastable equilibrium of an amorphous phase.[97] Hence, using a 10W substrate bias power, the sample deposition temperature was increased from room temperature to the range of 200°C to 500°C. As expected, deposition temperature did have a significant effect on the LiPON film deposition, composition, structure and properties. The residual stress at room temperature in the LiPON films changed from a weakly compressive stress (-159 MPa) to tensile (266 MPa) for the Samples C and I, respectively, as shown in Table 5-2. This increase in tensile residual stress is primarily due to the mismatch in the thermal expansion coefficients of the LiPON film ($\sim 15 \times 10^{-6} \text{ }^\circ\text{C}^{-1}$)[40] with the silicon substrate ($2.6 \times 10^{-6} \text{ }^\circ\text{C}^{-1}$) resulting in tensile strain upon cooling to room temperature from the elevated deposition temperature. More interestingly, the ionic conductivity increased

by an additional factor of five at the highest deposition temperature explored (500°C) to a maximum of 9.8×10^{-6} S/cm. The increased ionic conductivity was accompanied by a decrease in the activation energy of the LiPON films deposited at different temperatures are given in Table 5-2 and shown in Figure 6-2.

The increase in ionic conductivity with deposition temperature was not accompanied by an increase in excess volume of the LiPON amorphous matrix, as might be associated with an increased Li ion mobility. Rather, as shown in Table 5-6, the molar volume decreased with increased temperature. This is supported by increases in both the film density and refractive index. For example, the molar volume of sample I, deposited at 500°C, was $6.47 \text{ cm}^3/\text{mol atoms}$ compared to that of sample C, deposited at room temperature, which was $7.11 \text{ cm}^3/\text{mol atoms}$. This is a decrease of ~10% in molar volume and is consistent with the density increase between the two samples of ~18%. Table 5-2 also provides the refractive index at 999nm wavelength, which increased by 2.35%. The optical properties of LiPON films deposited at different temperatures are shown over a range of wavelengths in Figure 6-3 with the extinction coefficient (k) in Figure 6-3a) and the refractive index (n) in Figure 6-3b). The refractive index at longer wavelengths is understood to result from increased electron (and hence atomic) density[98] and this can be seen to be systematic with increasing deposition temperature. This is highlighted by the subset graph in the Figure 6-3b) that shows that the refractive index measured at 999 nm. The decrease in excess volume observed is expected for amorphous films processed at higher temperatures,[99] but does not explain the increase in ionic conductivity, as a decrease in atomic mobility with decreased excess volume is generally expected for amorphous films.[68] Figure 6-5a) also shows the increasing trend in ionic conductivity with deposition temperature to contradict that of molar volume.

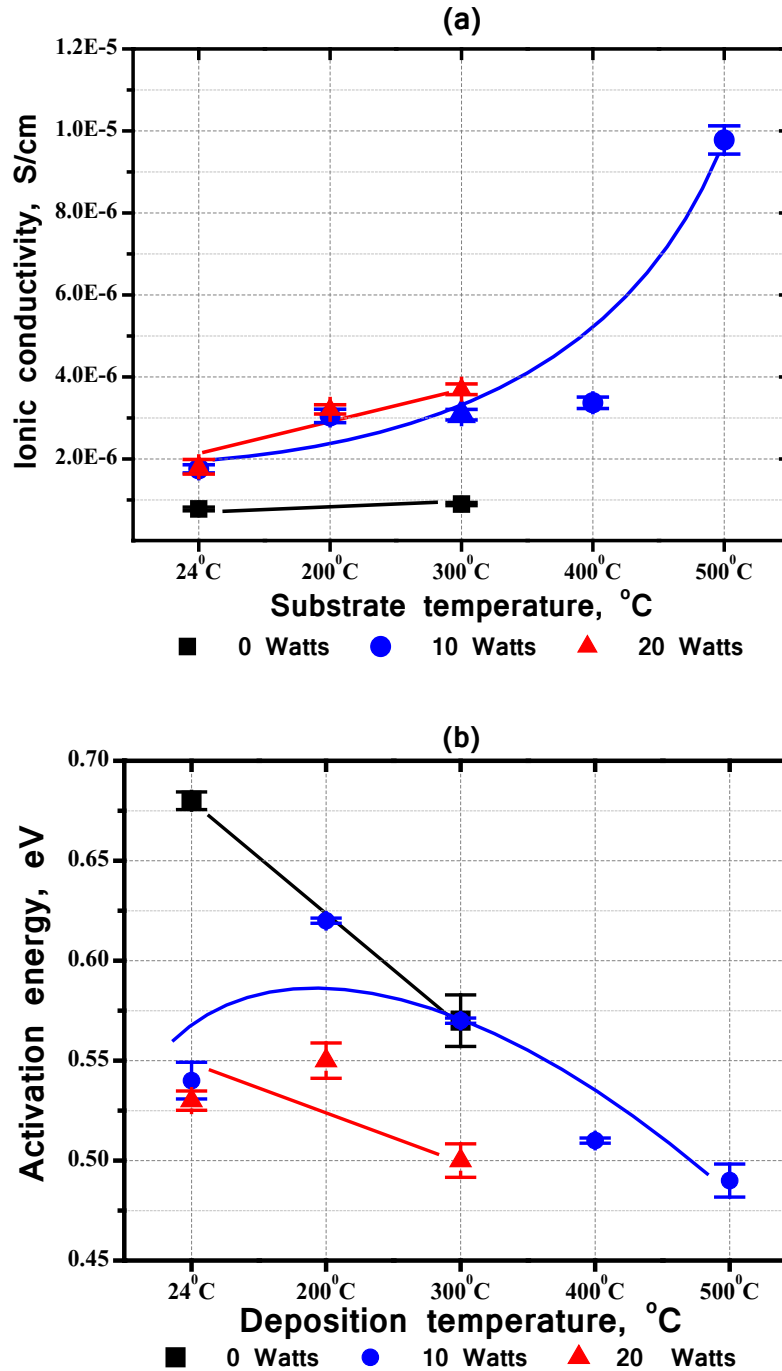


Figure 6-2 Inset (a) shows the ionic conductivity and inset (b) the activation energy of ionic conduction for LiPON films as a function of deposition temperatures. Please note that the lines are shown to guide the eye.

The increase in ionic conductivity with deposition temperature can also not be explained by an increase in the Li concentration of the films. Rather, a decrease in the Li concentration is

observed with increased in the deposition temperature. This is evident in the Li/P atomic ratio measured by ICP/OES and by the XPS given in Table 5-3. While both Li and P adatoms may be expected to have higher desorption rates from the LiPON film surface at higher temperatures, this effect is expected to be more pronounced for Li adatoms due to the weaker bonding of Li to the oxide matrix (the dissociation energy for a Li-O bond at 0K is 331.0 kcal/mol, while the dissociation energy for a P-O bond is 592.0 kcal/mol[100]). The decrease in Li content (and presumably, Li ion density) may also be expected to result in a reduced ionic conductivity, but this is not the case. The trends of Li/P atomic ratio, molar volume and the ionic conductivities with respect to the deposition temperatures are shown in Figure 6-5a).

Previous authors have suggested that the increases in the ratio of triply coordinated nitrogen to doubly coordinated nitrogen, ($>N^-$)/($=N^-$), correlate positively with ionic conductivity[5,6,12,16,27,30,31]. However, the results from the XPS data representative of the LiPON electrolyte layer do not support this. As shown in Table 5-4, ($>N^-$)/($=N^-$) decreases with increasing deposition temperature and increasing ionic conductivity. The relatively low values of ($>N^-$)/($=N^-$) measured are consistent with the nuclear magnetic resonance study of Stallworth et al. wherein the triply coordinated nitrogen was observed to be largely absent.[21]

However, it should be noted that the nitrogen concentration shows a steady increase with deposition temperature, as shown in Table 5-4. The total nitrogen percentage increases from 4.1% at room temperature to 10.3%.at 500°C, more than doubling as the ionic conductivity increases from 1.8×10^{-6} to 9.8×10^{-6} . This is consistent with prior work that has identified nitrogen substitution to improve the ionic conductivity over that of pure Li_3PO_4 films.[4–7,9,10,12,22,24,28,33,34,40,51]

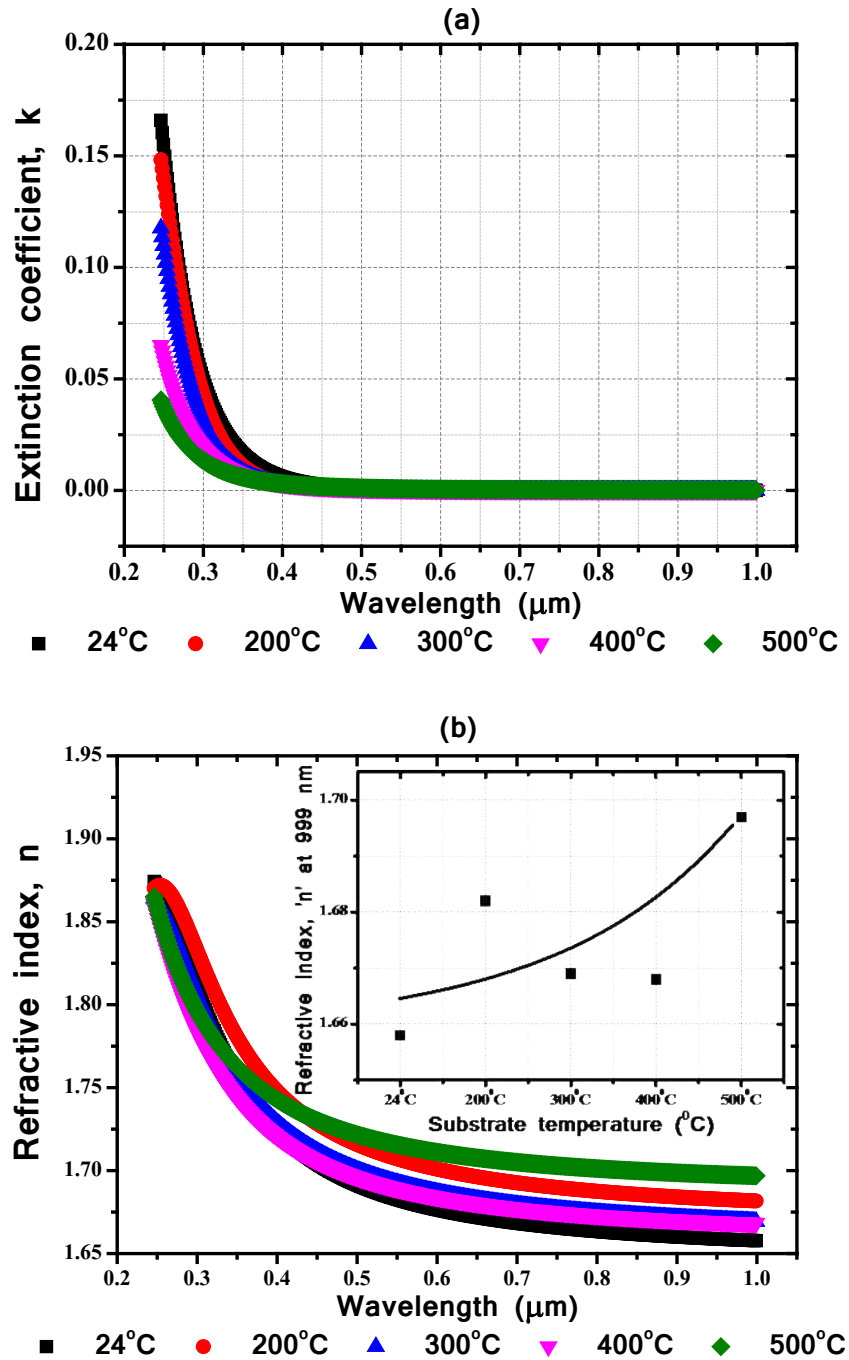


Figure 6-3 Inset (a) shows the optical extinction coefficient, k , and inset (b) the refractive index, n , for LiPON films deposited at various deposition temperatures as a function of wavelength. Inset (b) also shows a subset graph that shows the increase in refractive index at 999nm as a function of deposition temperature. Please note that the curve line is shown to guide the eye.

Another trend in LiPON film chemistry with deposition temperature is the tendency for the higher deposition temperature to result in films with a more strongly reducing, and less oxidizing, chemistry. The non-LiPON atomic percentages for Li, N, O, and P given in Tables 5-4 and 5-5 (derived from the high resolution spectra) can be summed to determine the percentage of non-LiPON bonding in the films. The non-LiPON bonding in films deposited at room temperature ranged from 10% to 22% while that of films deposited at higher temperatures ranged from 3% to 11%. Specifically, the increased deposition temperature resulted in a decrease in the Li-oxygen (Li_2O) bonding and an increasing in the reduced phosphorus bonding. These trends are shown in Figure 6-5b). This indicates that the films deposited at higher temperature were more reducing and less oxidative. This is consistent with higher mobility for Li ions at the higher deposition temperature if it is presumed that the oxidative chemistry has a role in pinning Li and reducing ion mobility.

The reducing chemistry and increased nitrogen content observed at increased deposition temperature may interact with structural factors that influence ionic conductivity. Specifically the density of point defects, such as broken/unsatisfied bonds can be expected to impact ionic conductivity as trapping sites for Li ions. A uniform structure is known to increase internal diffusion in amorphous films as shown conceptually in Figure 6-4.[68] The increased uniformity of energy barriers for interstitial diffusion in an amorphous matrix that is shown in Figure 6-4b) can be expected to similarly aid Li ion conduction in LiPON films of lower defect density. In amorphous semiconducting and insulating materials, an increase in the optical band gap is commonly observed with reducing point defects. The correlation of the optical band gap with ionic conductivity for the substrate temperature series of LiPON films is given in Figure 6-5 (c). Another measure of the defect density in the LiPON films is the optical penetration depth, δ . If

the optical defects and Li ion pinning defects in the film are presumed proportional to one another similarly processed films (i.e., same bias, pressure) then δ should also be proportional to the Li ion mobility in the film. Values for the δ are given in Table 5-2 (calculated at 246 nm) and Figure 6-5c) shows that the ionic conductivity and optical penetration depth also show a strong correlation for the deposition temperature series of samples, consistent with the increased deposition temperature providing a structural improvement in the LiPON amorphous matrix that allows a higher ionic mobility.

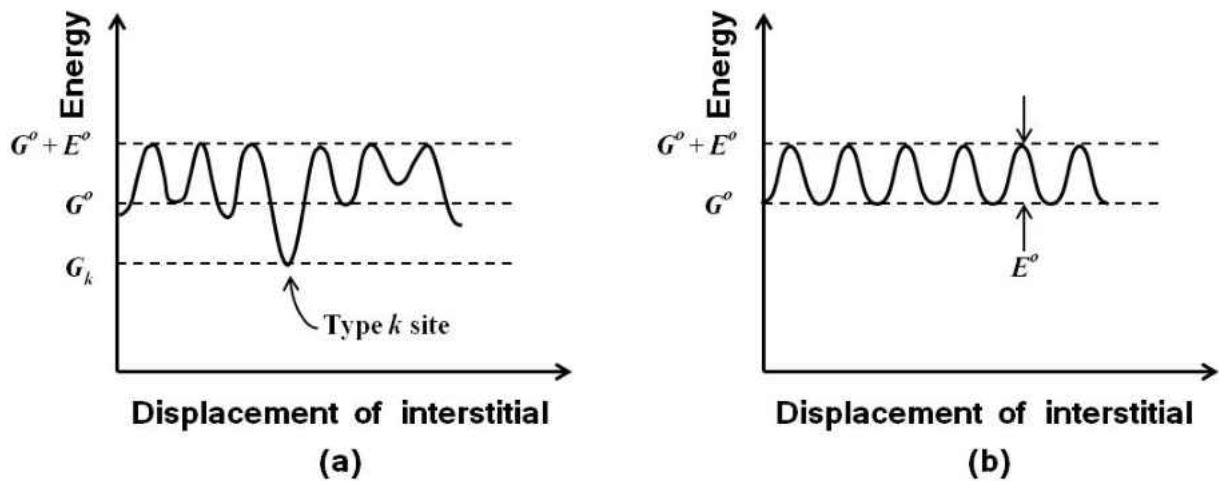
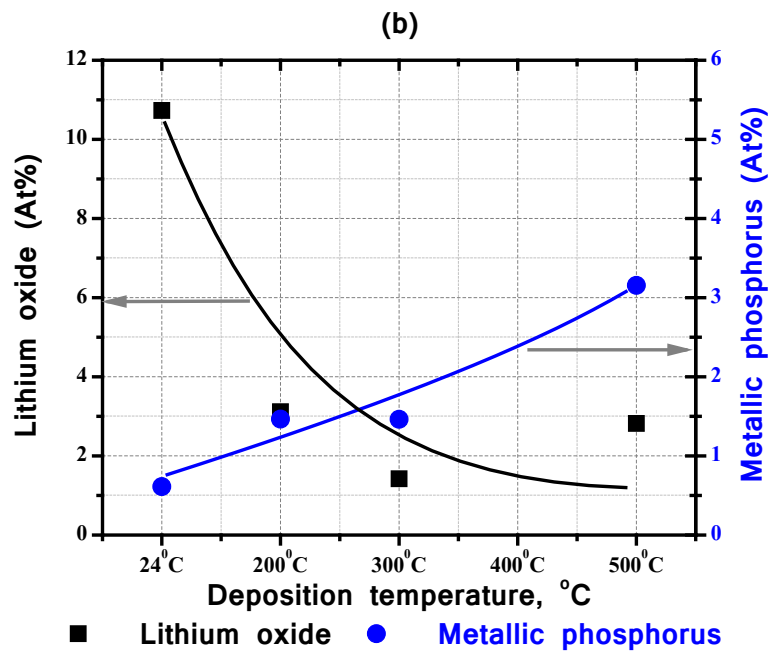
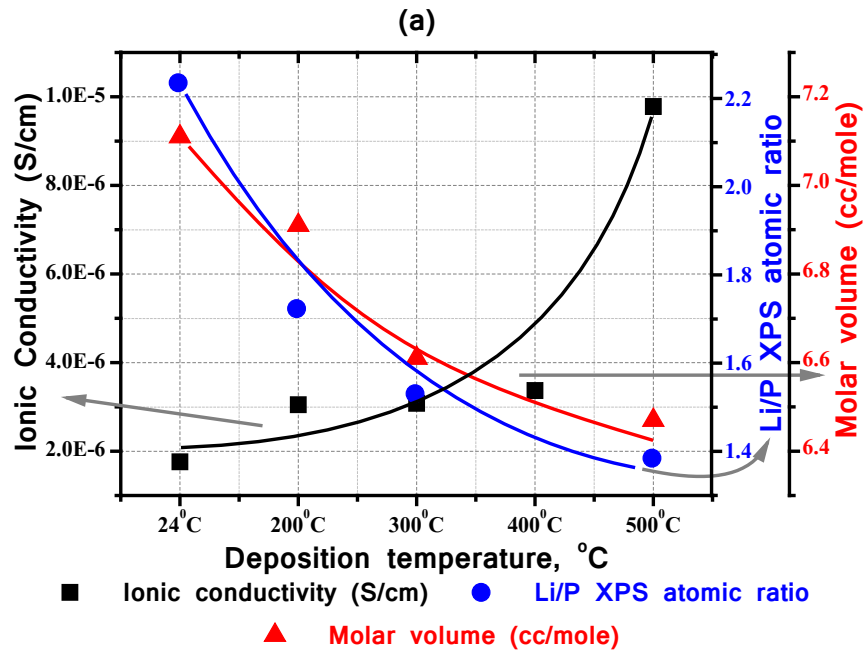


Figure 6-4(a) The energy variation of an amorphous glass with the displacement of a diffusing interstitial atom (Li^+ in LiPON) as it jumps between successive interstitial sites of varying energy levels. The type k site shown in the picture is at a typical lowest energy or a deep trap site. (b) A plot similar to (a) for interstitial jumping in an idealized or ordered material containing only the sites of equal energy states and having activation energies corresponding to E^o . (Reproduced, by permission, from John and Wiley Sons Inc., "Kinetics of Materials", by Robert W. Balluffi, Samuel M. Allen, W. Craig Carter, *Chapter 10 Diffusion in Non-crystalline Materials*, Figure 6-4.4, p235. Copyright © 2005 by John Wiley & Sons, Inc.) [68]



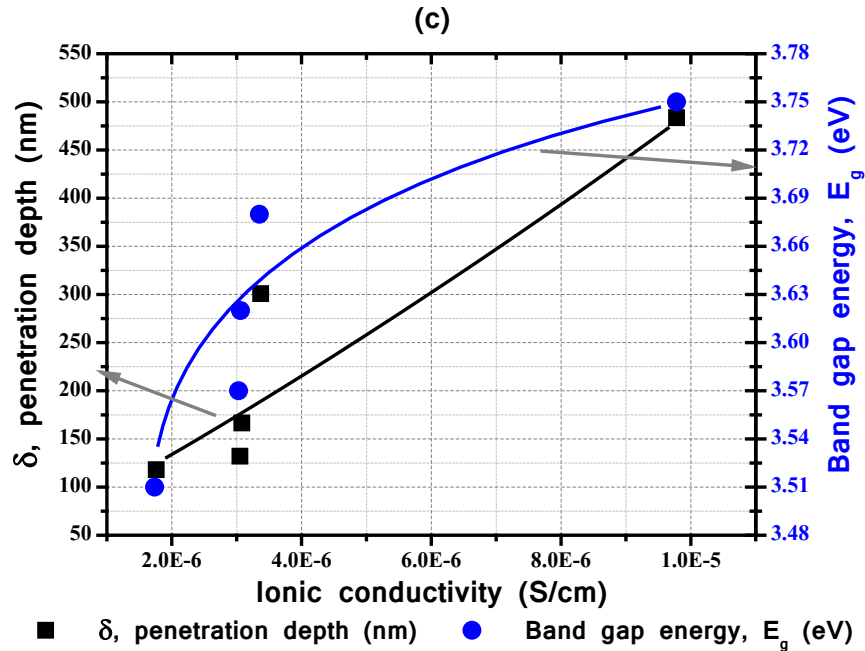


Figure 6-5 shows the characteristics of LiPON films deposited under different temperature conditions. Figure 6-5 (a) shows the increasing trend of the ionic conductivity, the decreasing trends of Li/P atomic ratio measured by XPS and molar volume calculated from film density and atomic concentration. Figure 6-5 (b) shows a decreasing trend of lithium oxide, Li_2O , and an increasing trend of reduced metallic phosphorus with the increase of deposition temperatures. In Figure 6-5 (c) the correlation between penetration depth, δ , (nm) and the ionic conductivity is strong and almost linear. Please note that the curved lines are shown to guide the eye.

CHAPTER 7 CONCLUSIONS

In this work substrate bias, deposition temperature, and sputtering process gas pressure were investigated in the deposition of LiPON thin films and Li ion conductivities in the 10^{-6} S/cm range were obtained with a maximum of 9.8×10^{-6} S/cm. These ionic conductivities substantially replicated that of previous workers, including the relatively high value of 9.1×10^{-6} S/cm reported by Chiu et al.

Ionic conductivity was found to increase modestly with substrate bias power for samples deposited at room temperature. The largest factor influencing ionic conductivity was found to be the temperature of the substrate during deposition, where ionic conductivity was found to increase with increased deposition temperature.

Compositional and structural factors were considered to understand the trends in ionic conductivity observed. XPS depth profiling measurements of the ratio of triply coordinated nitrogen to doubly coordinated nitrogen bonds ($>N^-$)/($=N^-$) were made that did not support prior reports of a positive correlation of this ratio to ionic conductivity. Rather, the large and variable values of this ratio (from 0.3 to 3) previously reported were only observed in oxidized surface regions of the LiPON films and depth profiling revealed that the ratio measured within the LiPON electrolyte layers did not positively correlate to ionic conductivity. This correlation supports and proves the claims of the other works[6,21,61], that the triply coordinated nitrogen sites are just a surface phenomenon and cannot be correlated largely to the ionic conduction. The increased deposition temperature was found to result in decreases in atomic volume and in the Li content of the films that also did not positively correlate to the ionic conductivity. Compositionally, an increase in the reduced phosphorous content and nitrogen content were found to positively correlate with ionic conductivity. Optical characterization of the LiPON film

structure revealed that, an increased effective band gap and penetration depth correlated positively with the increased ionic conductivity observed in the deposition temperature series. From this, it can be speculated that the most important factor in amorphous solid state ionic conductors may be an increased uniformity of the amorphous network, such that it has fewer defect sites that can serve to trap Li ions.

CHAPTER 8. FUTURE WORK

8.1 Solid state nuclear magnetic resonance study on the effects of substrate bias power, substrate heating

The structure-properties relationship of chemical bonding with ionic conductivity that was observed for samples deposited at different levels of substrate bias was consistent with mechanisms proposed in the literature. This was evidenced in the FT-IR, XPS and ICP/OES data. What is not yet fully understood is the processing-structure relationship, i.e., why bias resulted in these bonding changes. Clearly, bias is important to the PVD deposition of LiPON films and will continue to be studied in the proposed research. However, it would be worthwhile to know what phosphate environments are present and quantitatively how does it correlate with LiPON film electrolyte properties. Solid state nuclear magnetic resonance results of Stallworth et al. showed the various phosphate environments present and the large absence of triply coordinated nitrogen.[21]

8.2 Effect of hydrogen doping

PVD films are expected to be deficient in lithium. The incorporation of hydrogen during film deposition may allow an increase in the number of lithium sites in the amorphous structure and hence an increase in the ionic conductivity of lithium. Hydrogen doping of LiPON will be studied to see its effect on the bonding structure of the films and ionic conductivity. This study will not only include the introduction of hydrogen during deposition but also investigations to increase the lithium content of the films after deposition.

8.3 Effect of cation doping

Oxygen and nitrogen compositional variations have been extensively studied in LiPON films, however the role of cation doping has not been studied. Lithium and magnesium are

diagonal neighbors in the periodic table. In their ionic states, Li^+ and Mg^{2+} , they have equivalent ionic radii. Hence divalent doping of LiPON with Mg^{2+} can be done by simultaneously inducing cation vacancies in the system. When one Mg^{2+} ion is substituted for one Li^+ ion, in-order to maintain charge neutrality, a cation vacancy will be created in the structure. Such vacancies may form lithium ion migration sites. Increased vacancy concentration for the lithium sites is expected to increase the ionic mobility. The proposed research will include cation doping experiments, initially focused on magnesium but investigations of sodium, potassium, and calcium are also anticipated to understand the role of cation doping to the ionic conductivity.

8.4 Effect of anion doping

Amorphous sulphides also have network structures and sulphur based solid state electrolytes have shown very high ionic conductivities. Silicon doping of LiPON has been investigated with little benefit to ionic conductivity and this motivates experiments for sulphur doping of LiPON films. Processing difficulties are expected and the availability of suitable deposition targets is a precondition for this research approach.

8.5 3D microfabrication

Increasing the surface area will decrease the internal resistance and thereby increases the ionic conductivity. The electrolyte surface area can be increased by creating high aspect ratio surfaces prior to the electrolyte deposition. Such surfaces can be made at either the substrate or at the bottom of the current collector. MEMS technology can be used to generate high aspect ratios on the substrate using photolithography. Synthesizing nanoparticles of metals overcoated by platinum are expected to provide a significant increase in the surface area.

REFERENCES

- [1] L. David, T.B. Reddy, J. Broadhead, H.C. Kuo, Handbook of Batteries 3rd, 3rd ed., McGraw Hill, 2002.
- [2] P.G. Bruce, Solid State Electrochemistry, Cambridge University Press, Cambridge, 1997.
- [3] K.-K. Wong, A study of the effective electronic resistivity of rf sputtered deposited amorphous lithium niobate thin films, TUFTS University, 1992.
- [4] J.B. Bates, N.J. Dudney, G.R. Gruzalski, R.A. Zuhr, A. Choudhury, C.F. Luck, et al., Electrical properties of amorphous lithium electrolyte thin films, Solid State Ionics. 53-56 (1992) 647–654.
- [5] J.B. Bates, N.J. Dudney, G.R. Gruzalski, R.A. Zuhr, A. Choudhury, C.F. Luck, et al., Fabrication and characterization of amorphous lithium electrolyte thin films and rechargeable thin-film batteries, J. Power Sources. 43-44 (1993) 103–110.
- [6] B. Wang, B.C. Chakoumakos, B.C. Sales, B.S. Kwak, J.B. Bates, Synthesis, Crystal structure, Ionic Conductivity of a Polycrystalline Lithium Phosphorus Oxynitride with the gamma-Li₃PO₄ structure, J. Solid State Chem. 115 (1995) 313–323.
- [7] B. Wang, B.S. Kwak, B.C. Sales, J.B. Bates, Ionic conductivities and structure of lithium phosphorus oxynitride glasses, J. Non. Cryst. Solids. 183 (1995) 297–306.
- [8] B. Wang, J.B. Bates, F.X. Hart, B.C. Sales, R.A. Zuhr, J.D. Robertson, Characterization of thin-film rechargeable lithium batteries with lithium cobalt oxide cathodes, J. Electrochem. Soc. 143 (1996) 3203–3213.
- [9] X. Yu, J.B. Bates, G.E. Jellison-Jr., F.X. Hart, A Stable Thin-Film Lithium Electrolyte: Lithium Phosphorus Oxynitride, J. Electrochem. Soc. 144 (1997) 524–532.
- [10] H. Rabaa, H. Roald, Electronic and Structural Effects of Nitrogen Doping on the Ionic Conductivity of v-Li₃PO₄, J. Solid State Chem. 145 (1999) 619–628.
- [11] B.J. Neudecker, N.J. Dudney, J.B. Bates, “Lithium-Free ” Thin-Film Battery with In Situ Plated Li Anode, J. Electrochem. Soc. 147 (2000) 517–523.
- [12] N. Roh, S. Lee, H. Kwon, Effects of Deposition Condition on the Ionic Conductivity and Structure of Amorphous Lithium Phosphorus Oxynitrate Thin Film, Scr. Mater. 42 (2000) 43–49.
- [13] F. Vereda, N. Clay, A. Gerouki, R.B. Goldner, T. Haas, P. Zerigian, A study of electronic shorting in IBDA-deposited Lipon films, J. Power Sources. (2000) 201–205.

- [14] H. Rabaa, R. Hoffmann, N.C. Hernandez, J.F. Sanz, Theoretical Approach to Ionic Conductivity in Phosphorus Oxynitride Compounds, *J. Solid State Chem.* 79 (2001) 73–79.
- [15] B. Kim, Y. Sang, J. Lee, K. Joo, K. Jung, J. Oh, et al., Ion-implantation modification of lithium – phosphorus oxynitride thin-films, *J. Power Sources.* 109 (2002) 214–219.
- [16] F. Vereda-Moratilla, A study of the thin film battery electrolyte lithium phosphorus oxynitride deposited by an ion beam assisted process, Tufts University, 2003.
- [17] K. Chung, W. Kim, Y. Choi, Lithium phosphorous oxynitride as a passive layer for anodes in lithium secondary batteries, *J. Electroanal. Chem.* 566 (2004) 263–267.
- [18] W. West, Chemical stability enhancement of lithium conducting solid electrolyte plates using sputtered LiPON thin films, *J. Power Sources.* 126 (2004) 134–138.
- [19] Y. Iriyama, T. Kako, C. Yada, T. Abe, Z. Ogumi, Reduction of charge transfer resistance at the lithium phosphorus oxynitride/lithium cobalt oxide interface by thermal treatment, *J. Power Sources.* 146 (2005) 745–748.
- [20] Y. Iriyama, T. Kako, C. Yada, T. Abe, Z. Ogumi, Charge transfer reaction at the lithium phosphorus oxynitride glass electrolyte / lithium cobalt oxide thin film interface, *Solid State Ionics.* 176 (2005) 2371 – 2376.
- [21] P.E. Stallworth, F. Vereda, S.G. Greenbaum, T.E. Haas, P. Zerigian, R.B. Goldner, Solid-State NMR Studies of Lithium Phosphorus Oxynitride Films Prepared by Nitrogen Ion Beam-Assisted Deposition, *J. Electrochem. Soc.* 152 (2005) A516.
- [22] Y. Hamon, a Douard, F. Sabary, C. Marcel, P. Vinatier, B. Pecquenard, et al., Influence of sputtering conditions on ionic conductivity of LiPON thin films, *Solid State Ionics.* 177 (2006) 257–261.
- [23] E. Jeong, C. Hong, Y. Tak, S. Cheol, S. Cho, Investigation of interfacial resistance between LiCoO₂ cathode and LiPON electrolyte in the thin film battery, *J. Power Sources.* 159 (2006) 223–226.
- [24] H.Y.. Park, S.C.. Nam, Y.C.. Lim, K.G.. Choi, K.C.. Lee, G.B.. Park, et al., Effects of sputtering pressure on the characteristics of lithium ion conductive lithium phosphorous oxynitride thin film, *J. Electroceramics.* 17 (2006) 1023–1030.
- [25] N.J. Dudney, Addition of a thin-film inorganic solid electrolyte ž Lipon / as a protective film in lithium batteries with a liquid electrolyte, *J. Power Sources.* (2008) 176–179.
- [26] N.J. Dudney, Thin Film Micro-Batteries, *Electrochem. Soc. Interface.* (2008) 44–48.

- [27] Z. Hu, D. Li, K.A.I. Xie, Influence of radio frequency power on structure and ionic conductivity of LiPON thin films, *Bull. Mater. Sci.* 31 (2008) 681–686.
- [28] Y. Hamon, P. Vinatier, E.I. Kamitsos, M. Dussauze, C.P.E. Varsamis, D. Zielniok, Nitrogen flow rate as a new key parameter for the nitridation of electrolyte thin films, *Solid State Ionics*. 179 (2008) 1223 – 1226.
- [29] Y.G. Kim, Plasma-Assisted Directed Vapor Deposition for Synthesizing Lithium Phosphorus Oxynitride Thin Films, University of Virginia, 2008.
- [30] Y.G. Kim, H.N.G. Wadley, Lithium phosphorus oxynitride films synthesized by a plasma-assisted directed vapor deposition approach, *J. Vac. Sci. Technol. A*. 26 (2008) 174–183.
- [31] T. Pichonat, C. Lethien, N. Tiercelin, S. Godey, E. Pichonat, P. Roussel, et al., Further studies on the lithium phosphorus oxynitride solid electrolyte, *Mater. Chem. Phys.* 123 (2010) 231–235.
- [32] F.. Beniere, Transference numbers in ionic crystals, in: J.. Hladik (Ed.), *Phys. Electrolytes Vol 1 Transp. Process. Solid Electrolytes Electrodes*, 1st ed., Academic Press, London, 1972: pp. 299–318.
- [33] B. Fleutot, B. Pecquenard, H. Martinez, M. Letellier, a. Levasseur, Investigation of the local structure of LiPON thin films to better understand the role of nitrogen on their performance, *Solid State Ionics*. 186 (2011) 29–36.
- [34] W.-Y. Liu, Z.-W. Fu, C.-L. Li, Q.-Z. Qin, Lithium Phosphorus Oxynitride Thin Film Fabricated by a Nitrogen Plasma-Assisted Deposition of E-beam Reaction Evaporation, *Electrochem. Solid-State Lett.* 7 (2004) J36–J40.
- [35] K.-F. Chiu, C.C. Chen, K.M. Lin, C.C. Lo, H.C. Lin, W.-H. Ho, et al., Lithium phosphorus oxynitride solid-state thin-film electrolyte deposited and modified by bias sputtering and low temperature annealing, *J. Vac. Sci. Technol. A Vacuum, Surfaces, Film*. 28 (2010) 568–572.
- [36] I. Seo, Preparation and characterization of lithium thio- germanate thin film electrolytes grown by RF sputtering for solid state Li-ion batteries, Iowa State University, 2009.
- [37] N. Kamaya, K. Homma, Y. Yamakawa, M. Hirayama, R. Kanno, M. Yonemura, et al., A lithium superionic conductor., *Nat. Mater.* 10 (2011) 682–6.
- [38] D.J. Mount, Thin Film Batteries, *Vac. Technol. Coat.* (2007) 73 – 76.
- [39] M.R. Reidmeyer, D.E. Day, Phosphorus oxynitride glasses, *J. Non. Cryst. Solids*. 181 (1995) 201–214.

- [40] R.W. Larson, D.E. Day, Preparation and characterization of lithium phosphorus oxynitride glass, *J. Non. Cryst. Solids*. 88 (1986) 97–113.
- [41] W. Liu, Z. Fu, Q. Qin, A sequential thin-film deposition equipment for in-situ fabricating all-solid-state thin film lithium batteries, *Thin Solid Films*. 515 (2007) 4045–4048.
- [42] C.S. Nimisha, G.M. Rao, N. Munichandraiah, G. Natarajan, D.C. Cameron, Chemical and microstructural modifications in LiPON thin films exposed to atmospheric humidity, *Solid State Ionics*. 185 (2011) 47–51.
- [43] P. Birke, W. Weppner, Change of the oxidation state of phosphorus in sputtered $\text{Li}_{3\pm x}\text{PO}_{4\pm y}$ and $\text{Li}_{3\pm x}\text{PO}_{4\pm y}\text{N}_z$ films, *Ionics (Kiel)*. 2 (1996) 75–79.
- [44] W.C. West, J.F. Whitacre, V. White, B. V Ratnakumar, Fabrication and testing of all solid-state microscale lithium batteries for microspacecraft applications, *J. Micromechanics Microengineering*. 12 (2001) 58–62.
- [45] J.R. Van Wazer, *Phosphorus and its Compounds*, Interscience. 1 (1958).
- [46] Y.-N. Xu, Comparative studies of the electronic structure of LiFePO_4 , FePO_4 , Li_3PO_4 , LiMnPO_4 , LiCoPO_4 , and LiNiPO_4 , *J. Appl. Phys.* 95 (2004) 6583.
- [47] R.K. Brow, Review - the structure of simple phosphate glasses, *J. Non. Cryst. Solids*. 263-264 (2000) 1–28.
- [48] F. Liebau, M. O’Keefe, A. Novrotsky, *Structure and Bondings in Crystals II*, Acad. Press. (1981) 197.
- [49] T. Uchino, T. Yoko, Structure and vibrational properties of alkali phosphate glasses from ab initio molecular orbital calculations, *J. Non. Cryst. Solids*. 263-264 (2000) 180–188.
- [50] M. Tatsumisago, Y. Kowada, T. Minami, Structure of rapidly quenched lithium phosphate glasses, *Phys. Chem. Glas.* 29 (1988) 63–66.
- [51] R. Marchand, D. Agliz, L. Boukbir, A. Quemerais, Characterisation of Nitrogen containing phosphate glasses, *J. Non. Cryst. Solids*. 183 (1988) 297–306.
- [52] D.E. Day, Structural role of nitrogen in phosphate glasses, *J. Non. Cryst. Solids*. 112 (1989) 7–14.
- [53] M.R. Reidmeyer, M. Rajaram, D.E. Day, Preparation of phosphorus oxynitride glasses, *J. Non. Cryst. Solids*. 85 (1986) 186–203.
- [54] B.C. Bunker, D.R. Tallant, C.A. Balfe, R.J. Kirkpatrick, G.L. Turner, M.R. Reidmeyer, Structure of phosphorus oxynitride glasses, *J. Am. Ceram. Soc.* 70 (1987) 675–681.

- [55] E. Reculeau, A. Elkafir, M. Quarton, Characterisation and structural prediction of a new variety of Li_3PO_4 , *J. Solid State Chem.* 79 (1989) 205–211.
- [56] Y. a. Du, N. a. W. Holzwarth, Mechanisms of Li^+ diffusion in crystalline gamma - and beta - Li_3PO_4 electrolytes from first principles, *Phys. Rev. B - Condens. Matter Mater. Phys.* 76 (2007) 1–14.
- [57] Y. a. Du, N. a. W. Holzwarth, Li Ion Diffusion Mechanisms in the Crystalline Electrolyte $\gamma\text{-Li}_3\text{PO}_4$, *J. Electrochem. Soc.* 154 (2007) A999.
- [58] Y.A.. Du, N.A.W. Holzwarth, Li ion migration in Li_3PO_4 electrolytes: Effects of O vacancies and N substitutions, *ECS Trans.* 13 (2008) 1–8.
- [59] Y. a. Du, N. a. W. Holzwarth, Effects of O vacancies and N or Si substitutions on Li+ migration in Li_3PO_4 electrolytes from first principles, *Phys. Rev. B - Condens. Matter Mater. Phys.* 78 (2008) 1–13.
- [60] Y.A.. Du, N.A.W.. Holzwarth, First principles simulations of Li ion migration in materials related to LiPON electrolytes, *ECS Trans.* 25 (2010) 27–36.
- [61] Y. a. Du, N. a. W. Holzwarth, First-principles study of LiPON and related solid electrolytes, *Phys. Rev. B - Condens. Matter Mater. Phys.* 81 (2010) 1–15.
- [62] A.R. West, Crystalline solid electrolytes I: general considerations and the major materials, in: P.G. Bruce (Ed.), *Solid State Electrochem.*, Cambridge University Press, Cambridge, 1995: p. 19.
- [63] J.B. Goodenough, Crystalline solid electrolytes II: Material design, in: P.G. Bruce (Ed.), *Solid State Electrochem.*, Cambridge University Press, Cambridge, 1995: p. 54.
- [64] M.D. Ingram, Superionic glasses: theories and applications, *Curr. Opin. Solid State Mater. Sci.* 2 (1997) 399–404.
- [65] A. Bunde, K. Funkeb, M.D. Ingramc, An unified site relaxation model for ion mobility in glassy materials, *Solid State Ionics.* 86-88 (1996) 1311–1317.
- [66] A. Karthikeyan, P. Vinatier, A. Levasseur, K.J. Rao, The Molecular Dynamics Study of Lithium Ion Conduction in Phosphate Glasses and the Role of Non-Bridging Oxygen, *J. Phys. Chem. B.* 103 (1999) 6185–6192.
- [67] S.W. Martin, C.A. Angell, DC and AC conductivity in wide composition range $\text{Li}_2\text{O-P}_2\text{O}_5$ glasses, *J. Non. Cryst. Solids.* 83 (1986) 185–207.
- [68] R.W. Balluffi, S.M. Allen, W.C. Carter, Diffusion in Noncrystalline Materials, in: *Kinet. Mater.*, John Wiley & Sons, Inc., New Jersey, 2005: pp. 229–247.

- [69] M. Ohring, Discharges, Plasmas, and Ion-Surface Interactions, in: Mater. Sci. Thin Film., Second, Academic Press, San Diego, 2002: p. 177.
- [70] J. Greene, Short Course on “Sputter Deposition,” (2009).
- [71] P.D. Mani, A. Vijayakumar, M.-P. Real-Robert, S.J. Duranceau, K.R. Coffey, Characterisation of reactively sputter deposited lithium phosphorus oxy-nitride thin films, Journal of the electrochemical society, 2010.
- [72] JA Woollam, EASE, WVASE softwares, <http://www.jawoollam.com/software.html>.
- [73] C.M. Herzinger, B. Johs, W.A. McGahan, J.A. Woollam, W. Paulson, Ellipsometric determination of optical constants for silicon and thermally grown silicon dioxide via a multi-sample, multi-wavelength, multi-angle investigation, J. Appl. Phys. 83 (1998) 3323–3336.
- [74] J.A. Woollam, Guide to using WVASE32, J.A. Woollam Co.’ Inc.,.
- [75] H.G. Tompkins, Software Training Manual, 2008, J.A. Woollam Co. Inc..
- [76] B. Fleutot, B. Pecquenard, H. Martinez, a. Levasseur, Thorough study of the local structure of LiPON thin films to better understand the influence of a solder-reflow type thermal treatment on their performances, Solid State Ionics. 206 (2012) 72–77.
- [77] V.L.. Bonch-Bruevich, Problems of the electron theory of disordered semiconductors, Sov. Phys. Uspekhi. 26 (1983) 664 – 695.
- [78] F. Urbach, The long-wavelength edge of photographic sensitivity and of the electronic Absorption of Solids [8], Phys. Rev. 92 (1953) 1324.
- [79] J.. Tauc, Absorption edge and internal electric fields in amorphous semiconductors, Mater. Res. Bull. 5 (1970) 721–729.
- [80] S. Associates, ZView software, (n.d.) <http://www.scribner.com/zplot-and-zview-for-window>.
- [81] R.D. Armstrong, T. Todd, Interfacial electrochemistry, in: P.G. Bruce (Ed.), Solid State Electrochem., Cambridge University Press, Cambridge, 1995: p. p287.
- [82] J. Jamnik, J. Maier, Treatment of the Impedance of Mixed Conductors Equivalent Circuit Model and Explicit Approximate Solutions, J. Electrochem. Soc. 146 (1999) 4183–4188.
- [83] W. Lai, S.M. Haile, Impedance Spectroscopy as a Tool for Chemical and Electrochemical Analysis of Mixed Conductors: A Case Study of Ceria, J. Am. Ceram. Soc. 88 (2005) 2979–2997.

- [84] N.J. Donnelly, C.A. Randall, Mixed conduction and chemical diffusion in a $\text{Pb}(\text{Zr}_{0.53}\text{Ti}_{0.47})\text{O}_3$ buried capacitor structure, *Appl. Phys. Lett.* 96 (2010) 052906–1 – 052906–3.
- [85] D. Grahame, The electrical double layer and the theory of electrocapillarity., *Chem. Rev.* (1947) 441–501.
- [86] K. Siegbahn, Electron spectroscopy for chemical analysis (e . s . c . a .), *Philos. Trans. R. Soc. London.* 268 (1979) 33–57.
- [87] C.D.. Wagner, W.M.. Riggs, L.E.. Davis, J.F.. Moulder, G.E.. Muilenberg, *Handbook of X-ray Photoelectron Spectroscopy*, Perkin Elemer Corporation, Physical Electronics Division, 6509 Flying Cloud Drive, Eden Prairie, Minnesota - 55344, 1979.
- [88] S. Tanaka, M. Taniguchi, H. Tanigawa, XPS and UPS studies on electronic structure of Li_2O , *J. Nucl. Mater.* 283-287 (2000) 1405–1408.
- [89] Casa software Ltd, CasaXPS: Processing software for XPS, AES, SIMS and more, (n.d.). <http://www.casaxps.com>
- [90] G. Stoney, The Tension of Metallic Films deposited by Electrolysis., *Proc. R. Soc. London.* 82 (2013) 172–175.
- [91] M. a. Hopcroft, W.D. Nix, T.W. Kenny, What is the Young’s modulus of silicon?, *J. Microelectromechanical Syst.* 19 (2010) 229–238.
- [92] H. Kim, T. Seong, J. Lim, W. Ii, Y. Soo, Electrochemical and structural properties of radio frequency sputtered cobalt oxide electrodes for thin- lm supercapacitors, 102 (2001) 167–171.
- [93] Y.-C. Lu, E.J. Crumlin, G.M. Veith, J.R. Harding, E. Mutoro, L. Baggetto, et al., In Situ Ambient Pressure X-ray Photoelectron Spectroscopy Studies of Lithium-Oxygen Redox Reactions, *Sci. Rep.* 2 (2012) 1–6.
- [94] A. Thißen, D. Ensling, M. Liberatore, Q.H. Wu, F.J.F. Madrigal, M.S. Bhuvaneshwari, et al., Experimental routes to in situ characterization of the electronic structure and chemical composition of cathode materials for lithium ion batteries during lithium intercalation and deintercalation using photoelectron spectroscopy and related techniques, *Ionics (Kiel).* 15 (2009) 393–403.
- [95] C.E. Myers, H.F. Franzen, J.W. Andereg, X-ray photoelectron spectra and bonding in transition-metal phosphides, *Inorg. Chem.* 24 (1985) 1822–1824.
- [96] T.P.. Moffat, R.M.. Latansion, R.R. and Ruf, An X-ray Photoelectron Spectroscopy Of Chromium-Metalloid Alloys-III, *Electrochim. Acta.* 40 (1995) 1723–1734.

- [97] M. Ohring, Film Structures, in: Mater. Sci. Thin Film., Second, Academic Press, San Diego, 2002: p. 495.
- [98] E.S. Machlin, Optical Properties, in: E.S. Machlin (Ed.), Mater. Sci. Microelectron. II - Eff. Struct. Prop. Thin Film., Second, Elsevier, 2006: pp. 113–115.
- [99] F. Demichelis, G. DellaMea, G. Crovini, C.F. Pirri, T. E., E. Giamello, Hydrogen evolution in amorphous silicon carbide, Phys. B Condens. Matter. 170 (n.d.) 149–152.
- [100] B. deB. Darwent, Bond disassociation energy in simple molecules, 1970.